# FLYING-HOT-WIRE STUDY OF TWO-DIMENSIONAL TURBULENT SEPARATION ON AN NACA 4412 AIRFOIL AT MAXIMUM LIFT

Thesis by

Alan J. Wadcock

In Partial Fulfillment of the Requirements

for the Degree of

Doctor of Philosophy

California Institute of Technology

Pasadena, California

1978

(Submitted May 26, 1978)

ACKNOWLEDGEMENTS

I would like to express my sincere appreciation to the many people who have contributed to this research.

Special thanks go to my advisor, Professor Donald Coles, whose guidance was invaluable and whose constructive criticism is responsible for a great many improvements in the manuscript.

I also wish to thank Dr. Brian Cantwell for his design of the flying-hot-wire apparatus which made these measurements possible.

Finally, I would like to express my appreciation to William Bettes and the members of the GALCIT 10-Foot Wind Tunnel crew, for their co-operation during the hectic period of the airfoil experiment; to Earl Dahl and the Aeronautics Machine Shop for their assistance throughout the research program; and to Kathy Franson and Marcia Clark for typing the manuscript.

This research was supported by the National Aeronautics and Space Administration, Ames Research Center, under Grant NGL 05-002-229 and Grant NSG-2319.

## ABSTRACT

Hot-wire measurements have been made in the boundary layer, the separated region, and the near wake for flow past an NACA 4412 airfoil at maximum lift. The Reynolds number based on chord was about 1,500,000. Special care was taken to achieve a two-dimensional mean flow. The main instrumentation was a flying hot wire; that is, a hot-wire probe mounted on the end of a rotating arm. The probe velocity was sufficiently high to avoid the usual rectification problem by keeping the relative flow direction always within a range of $\pm$ 30 degrees to the probe axis. A digital computer was used to control synchronized sampling and storage of hot-wire data at closely spaced points along the probe arc. Data were obtained at several thousand locations in the flow field. These data include intermittency, two components of mean velocity, and mean values for three double, four triple, and five quadruple products of two velocity fluctuations. No information was obtained about the third (spanwise) velocity component. The data are available on punched cards in raw form and also in processed form, after use of smoothing and interpolation routines to obtain values on a fine rectangular mesh aligned with the airfoil chord. The data are displayed as contour plots of the fifteen variables.

TABLE OF CONTENTS

# I. INTRODUCTION

The rate of development of methods for calculating turbulent flows is limited by a scarcity of accurate measurements. The present research is aimed at a particular need for data in flows which involve separation or rapid relaxation or both. The measurements describe in considerable detail the trailing-edge separation process on an airfoil operating near maximum lift, and also describe the relaxation process in the near wake to a distance of about one chord length downstream of the trailing edge.

Previous Work. -- The experimental material of the Stanford contest (see Coles and Hirst 1968) included several studies of turbulent separation or near-separation in diffusers and on airfoils. The most complete study, carried out by Schubauer and Klebanoff (1950), is unsatisfactory in several respects. The mean flow was definitely three-dimensional in the region of rapidly rising pressure, and the published values for turbulent stresses are almost certainly too large, perhaps by as much as forty percent.

It is noteworthy that none of the experimenters who provided material for the Stanford contest attempted measurements beyond separation. The main reason was probably that the best instrument available at the time (the conventional hot-wire probe) has limited directional response and tends to rectify the velocity signal in regions of intermittently reversed flow. This property continues to restrict the usefulness of hot-wire instrumentation in such flows (e.g., Chu and Young 1975, Caupenne 1976). Experimenters may

also have been influenced by the fact that until recently no methods have been available for continuing a calculation beyond separation. Occasionally, measurements have been made downstream of separation but outside the separated region. Fomina and Buchinskaia (1938), for example, used total-pressure and static-pressure probes to obtain such data for flow over an airfoil with trailing-edge stall. In a modern study of separating flow in a diffuser by Simpson, Strickland and Barr (1977), the rectification problem was avoided by use of laser-Doppler instrumentation with frequency offset. However, the data are too sparse to allow accurate modeling of mixing processes in the separated region.

The nearest equivalent to the experiment reported here is the recent work by Seetharam and Wentz (1977). The two experiments may seem at first to be very similar. Both deal with flow past an airfoil at high angle of attack at about the same Mach number and Reynolds number. Both include data in the wake to about one chord length downstream of the trailing edge. Both airfoils had an aspect ratio of order two and were mounted between plane parallel side walls in a compound test section. However, the two experiments are completely different in attack and execution. Seetharam and Wentz used only pressure instrumentation of various types, except for some recent qualitative work with hot-film probes (Wentz and Seetharam 1977), and it is difficult to estimate the magnitude of any errors which may be present in their data. The same is true of similar data obtained by Goradia, Mehta, and Shrewsbury (1977) during an independent

investigation of flow past the same airfoil section. Moreover, our experience has been that it is not easy to establish a satisfactory flow. Our mean flow was highly three-dimensional in the absence of effective flow control, and was grossly unsteady at angles of incidence beyond the angle for maximum lift (see Sections 3.1 and 3.2 of this report, especially Figures 9, 10, and 17).

Perspective of the Present Research. -- The main experimental technique of the present research uses a flying hot wire mounted on the end of a whirling arm. The rectification problem is thus avoided by biasing the relative velocity. In practice, the tip speed of the whirling arm is made large enough so that the direction of the relative flow at the probe (a standard commercial X-array) is always within the useful range of about $\pm$ 30 degrees with respect to the probe axis.

The flying-hot-wire technique has several special features, all of which were recognized at the outset of the research and most of which are discussed at length in a separate report on instrumentation (Coles, Cantwell, and Wadcock 1977; this report will frequently be referred to below as CCW). One special feature (bad) is that the wake of the whirling arm is a substantial moving disturbance in the flow. Another (good) is that data are obtained along a line rather than at a point. A third (good) is that the hot-wire probes are inherently self-calibrating in pitch. A fourth (bad) is that hot-wire signals must be transmitted through slip rings. A fifth (bad) is that the relative position of probe and

model is very difficult to measure. A sixth (good and bad) is that the technique is necessarily digital. The probe signals are not statistically stationary (the concept of spectrum, for example, plays no role at all in the measurements). Mean values are, by definition, ensemble mean values obtained by repeated sampling at fixed points in the flow. The primary effort in instrumentation thus tends to shift away from the hot-wire equipment and toward the digital computer which manages and monitors the processes of data acquisition and recording.

Several other problems were anticipated in the research. Previous experience in the GALCIT* 10-foot tunnel (which is constructed partly of concrete) suggested that the life expectancy of hot-wire probes might be very short, of the order of minutes. In practice, this problem was serious but not critical. All of the data reported here were obtained with two X-arrays, both of which survived about twenty hours of tunnel operation.

A second problem, common to all research of this kind, was that it might be difficult to achieve a two-dimensional mean flow. A small axially-symmetric model was tested and judged to be unsatisfactory, at least for the geometry chosen, and a two-dimensional model was eventually used. The natural flow at high angles of incidence turned out to be very far from two-dimensional, as expected. After an unproductive effort to improve the flow by using conventional active methods of flow control, success was

---

*Graduate Aeronautical Laboratories, California Institute of Technology.

finally achieved by a simple passive method, as described in Section 3.1.

A third problem, amounting to a calculated risk, was the prospect that the flying-hot-wire instrumentation might interfere with and change the flow under study. Our original expectation, which did not materialize, was that the wake of the moving probe might noticeably affect the momentum distribution along its trajectory. What happened was quite different. Because the separation line is not fixed by the geometry, flow separation from an airfoil is exquisitely sensitive to small changes in the ambient flow at large distances. Such changes did occur. The obstacle presented to the free stream by the rotor, and especially by the rotor hub, caused a measurable dependence of the flow in the boundary layer and wake on the position of the rotor in the test section. Considerable time was required to understand this effect and minimize its importance, as described in Section 5.1.

Critique of the Present Research. -- It is characteristic of research done in large, expensive, rigidly-scheduled facilities that any given operation is done only once. It is characteristic of graduate research that any given operation is done for the first time; i.e., by amateurs. In some cases, we consider that the work reported here was well done. We are satisfied with the simple solution found for the problem of flow control, and with the techniques developed for smoothing and interpolating the hot-wire data to obtain reliable values on a closely-spaced rectangular grid. However, other operations were indifferently well

done. Higher fidelity could have been achieved in molding the airfoil model, and the methods used to cope with hot-wire drift could probably have been improved. Finally, some operations were badly done. The most serious of these was our failure to anticipate the real nature of probe interference at the time that the measurements were being planned.

Our conclusion at the end is that the flying hot wire is a difficult but usable instrument. It is probably best suited to bluff-body flows, where close approach to a surface is not mandatory, and where separation is fixed or nearly fixed by the geometry of the model. When the same flying-hot-wire instrumentation was used by Cantwell (1975) to study vortex shedding from a circular cylinder, no measurable interference effects were found.

At least two other instruments besides the flying hot wire might be considered for use in regions of occasional reversed flow. These are the pulsed-wire probe and the laser-Doppler velocimeter (LDV). The first has been used by Bradbury (1976) and the second by Owen (1976) to study flow in closed recirculating regions marked by very high turbulence levels. Experience with pulsed-wire probes at GALCIT (Tombach 1973) has been that there are formidable difficulties in measurement of turbulent stresses. Experience with LDV techniques has been more favorable, although statistical bias can be a serious problem when operating in the single-particle mode. Unfortunately, the geometry of the only large-scale wind tunnel at GALCIT is not well suited

to optical methods. It is also likely that the need for an optically clear path might interfere with the need for flow control. The measurements might have been done with the LDV in water (with attendant advantages in terms of flow visualization), except that we have no facility which would be free of cavitation under the conditions of the experiment. In any event, it was necessary to commit the experiment to a particular technique in late 1972. At that time we did not consider the LDV to be the instrument of choice, in spite of its advantage of linearity. The development effort for the LDV appeared to be comparable to that required for the flying hot wire, and the latter instrument was certainly sufficiently promising to merit a trial.

One issue in any measurement of turbulence is the time required to obtain a stable mean. The moving probe has the advantage that it is a line rather than a point instrument. In our application, each five-minute run yielded an ensemble of several thousand velocity samples at each of sixty or more points along an arc in the flow. At each of the sixty points, moreover, the flow was observed over the full five minutes. The time required to obtain a stable mean for a point measurement is not known, but it is certainly longer than the five seconds which could be allotted if the same tunnel operating time and the same density of data points were specified, without allowance for the time required to move the probe from one point to another. The benefits of a stable mean are conspicuous in the present results. We know of no other experiment of comparable complexity in

which the experimental data can be differentiated with any confidence.

We expect that for some time to come the present measurements will provide a major test case for development of calculation methods for turbulent flow. The spirit of the measurements is entirely the spirit of Reynolds averaging, with the additional feature that the boundary-layer approximation is avoided. The quantities which are reported as processed data are quantities which appear in the Reynolds equations for the evolution of mean velocity and for the evolution of mean double products of velocity fluctuations. So that users of the data need be in no doubt about the strengths and weaknesses of the results, we have made every effort to describe the experiment completely, warts and all, and to record all the results in accessible form. Instructions for gaining access to the data are included in the text.

## II. APPARATUS AND INSTRUMENTATION

### 2.1 Tunnel Modifications

We originally thought that the problem of achieving a two-dimensional mean flow might be finessed by using an axially-symmetric ring airfoil. A small ring model with a diameter/chord ratio of about unity and with inside stall was therefore constructed and tested. The results were disappointing. The main difficulty was that the pressure rise in the diffuser-like internal flow was accompanied by a large increase in the rate of turbulence propagation toward the axis. The region of potential

flow on the axis of symmetry ended approximately at the trailing edge, and the overall flow about the ring resembled the flow about a bluff body with base bleed. To improve this situation, the diameter/chord ratio would have to be substantially increased. For a ring of fixed diameter in a given flow, there would be a corresponding decrease in Reynolds number based on chord. For this and other reasons, the ring configuration was abandoned in favor of a more conventional plane wing. One immediate benefit was that the angle of incidence of the airfoil no longer had to be frozen at the design stage. At the same time, it became certain that considerable additional effort would be required for flow control, with no guarantee of success.

False Walls. -- The circular cross section of the GALCIT 10-foot wind tunnel became a disadvantage when the decision was made to abandon the ring wing in favor of the plane wing. It was necessary to construct false walls inside the working section, as shown in Figures 1 and 2. Vertical steel H-beams were bolted to T-slots which ran the length of the test section at 45 degrees from the tunnel plane of symmetry. These beams were covered by 1.9-cm thick plywood panels to give an overall wall thickness of about 14 cm. The distance between the inner faces of the false walls was 199.1 cm.

Relative to the entrance plane of the cylindrical test section, whose diameter and length are both 304.8 cm (10 feet), the false walls were placed as shown in the plan view in Figure 3. The leading edges were streamlined by solid wood nose pieces shaped

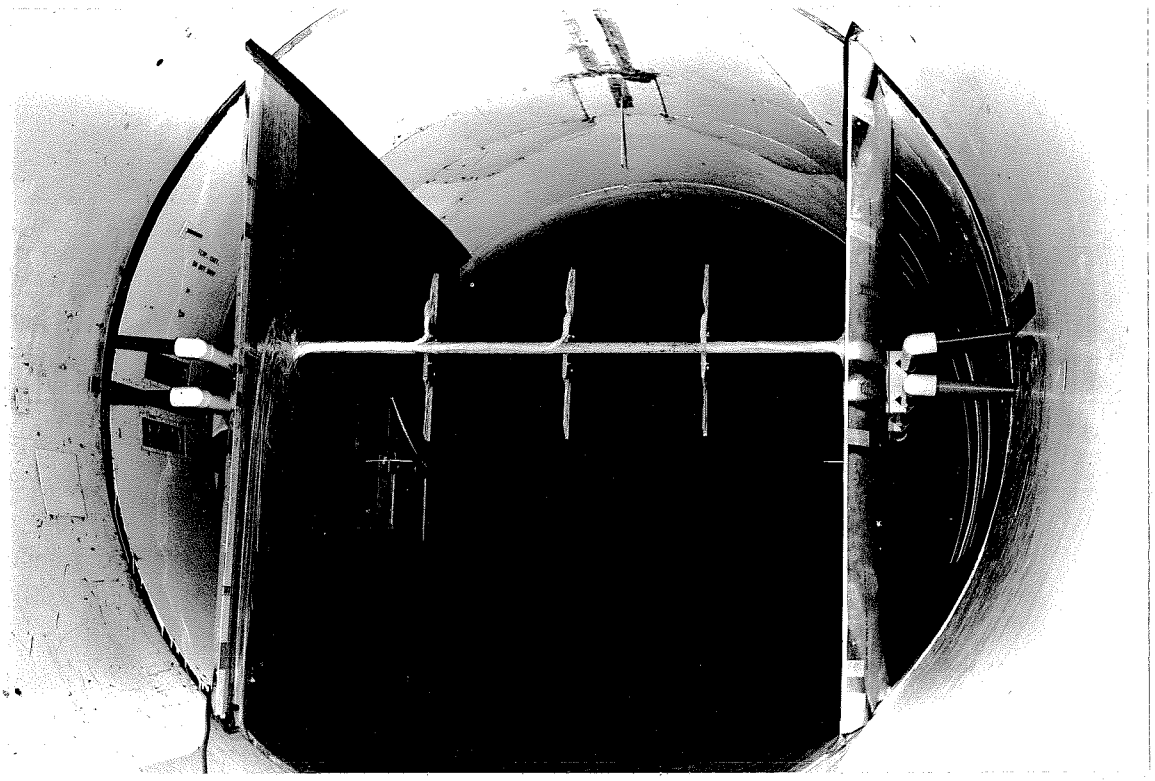

Figure 1. View of cylindrical test section, false walls, and airfoil model, looking upstream from diffuser. Airfoil is at 14 degrees angle of incidence. Wake rake is in foreground. Flow guides are present in final configuration. Note absence of screens in supply section.

to represent the first 30 percent of an NACA 0012 airfoil section. The trailing edges were streamlined by tail pieces made of plywood and sheet metal, flat toward the center of the test section. Small windows were installed in the false walls for observation purposes. All wood surfaces were smoothed and varnished. Tufts were used to verify that unwanted separation did not occur on the false walls.

Flow Control. -- Plenum chambers were also installed in the walls near the trailing edge of the model. These chambers

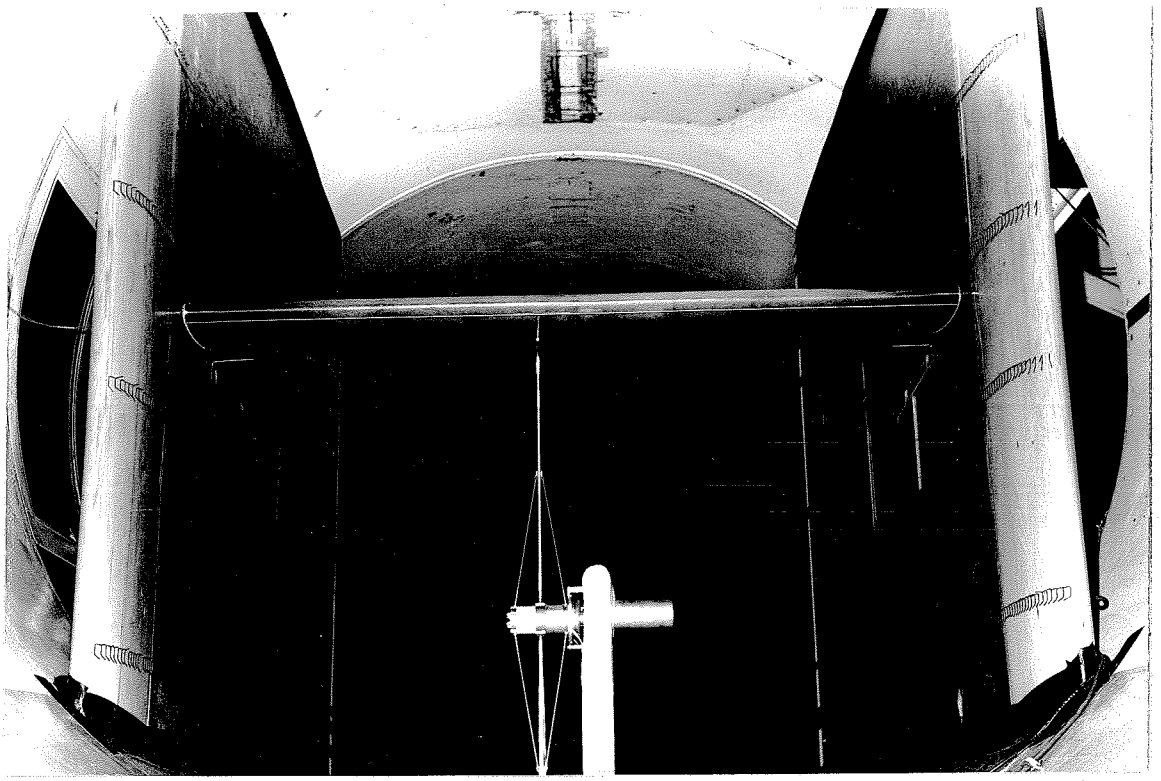

Figure 2. View of cylindrical test section, false walls, and airfoil model, looking downstream from supply section. Airfoil is at 14 degrees angle of incidence. Part of strut and most of rotor are visible below airfoil. Flow guides are present in final configuration.

could be covered by solid or perforated plates or by plates with a single vertical slot to produce a plane wall jet directed downstream. Air was supplied to (or removed from) the plenum chambers through ducts running downstream along the outside surface of the false walls. The ducts left the test section through a 5-cm annular slot which separates the test section from the diffuser. This plumbing and an associated 15-horsepower blower were intended for flow control, but proved to be inadequate to the need. A simpler and more effective method for flow control

was eventually found and was used during the main experiments, as described under "Passive Flow Control" in Section 3.1 below.

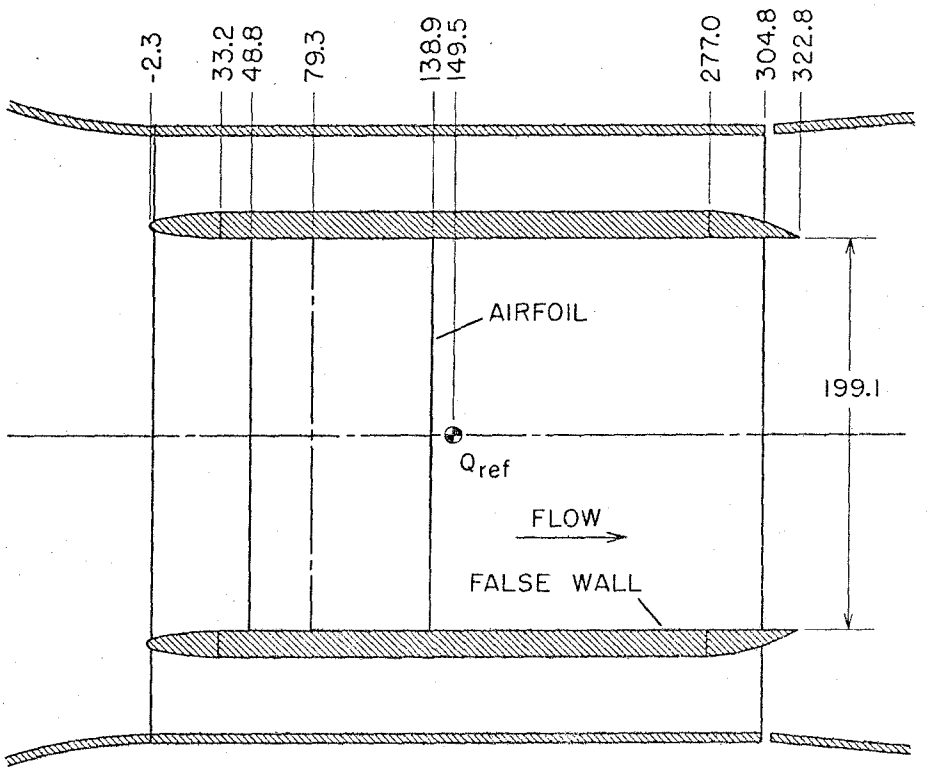


Figure 3. Plan view of test section showing location of false walls, airfoil, and roof-mounted pitot-static tube. Dimensions are in centimeters. Stations are measured from entrance plane of test section.

## 2.2 The Airfoil Model

Choice of Section and Size. -- In principle, one airfoil section would serve as well as another to meet the primary objectives of the present research. What was wanted was a well-documented section known to have good stalling characteristics; i.e., a smooth variation of lift with angle of attack near maximum lift, with gradual trailing-edge separation. The section chosen was the

NACA 4412. The aerodynamic properties of this section have been measured in considerable detail by Pinkerton (1936, 1938) for (effective) Reynolds numbers based on chord from 100,000 to 8,200,000. In particular, there seems to be no problem with leading-edge separation at (effective) Reynolds numbers greater than about 900,000 if stream turbulence or some other efficient tripping method is used to stimulate transition.

There were conflicting size requirements for the model. The chord should be small to make the near wake experimentally accessible, but large to permit exploration of the separated region in detail. Important practical considerations included the range of the available traverse and the anticipated effect of free-stream turbulence level on transition. A small chord implies a high tunnel speed to reach a given Reynolds number. High tunnel speed in turn means less testing time and less drift in the instrumentation; but it also means larger aerodynamic loads and deflections, increased risk of hot-wire breakage, and decreased wire sensitivity. After all of these factors were taken into account, including also cost, the chord of the airfoil was specified as 90.12 cm. The span was constrained to be 198.8 cm by the geometry of the false walls used to convert the circular test section to an approximately rectangular one.

Analytical Definition. -- The NACA 4412 airfoil is defined analytically by formulas published by Jacobs, Ward, and Pinkerton (1933), by Abbott and von Doenhoff (1949), and elsewhere. With $\xi = x/c$ and $\eta = y/c$, where c is the chord length, the 4412

camber line consists of the two parabolic arcs

$$\eta_c(\xi) = \frac{1}{4}\left(\frac{4}{5}\xi - \xi^2\right) \qquad (1)$$

for $0 \le \xi \le 2/5$ and

$$\eta_c(\xi) = \frac{1}{9}\left(\frac{1}{5} + \frac{4}{5}\xi - \xi^2\right) \qquad (2)$$

for $2/5 \le \xi \le 1$. The thickness distribution for unit chord is given by

$$t(\xi) = \frac{3}{5}\left(0.2969\,\xi^{\frac{1}{2}} - 0.1260\,\xi - 0.3516\,\xi^2 + 0.2843\,\xi^3 - 0.1015\,\xi^4\right) \qquad (3)$$

where t is measured symmetrically along the local normal to the camber line. The airfoil surface is therefore defined by

$$\xi_s(\xi) = \xi \mp t \sin\sigma \qquad (4)$$

$$\eta_s(\xi) = \eta_c \pm t \cos\sigma \qquad (5)$$

where $\tan\sigma = d\eta_c/d\xi$. The upper (lower) signs refer to the upper (lower) surface.

Fabrication. -- The airfoil model was fabricated of fiberglass-reinforced polyester resin using the mold shown in Figure 4. The mold surface was thin polished stainless-steel sheet bonded to external ribs. The airfoil was made in two pieces, a main body and a full-span hatch cover. The hatch extended from $x/c = 0.18$ to $x/c = 0.73$ on the pressure surface and gave access to the interior for installation of ribs, spars, and pressure instrumentation. The mold section for the rear part of the pressure

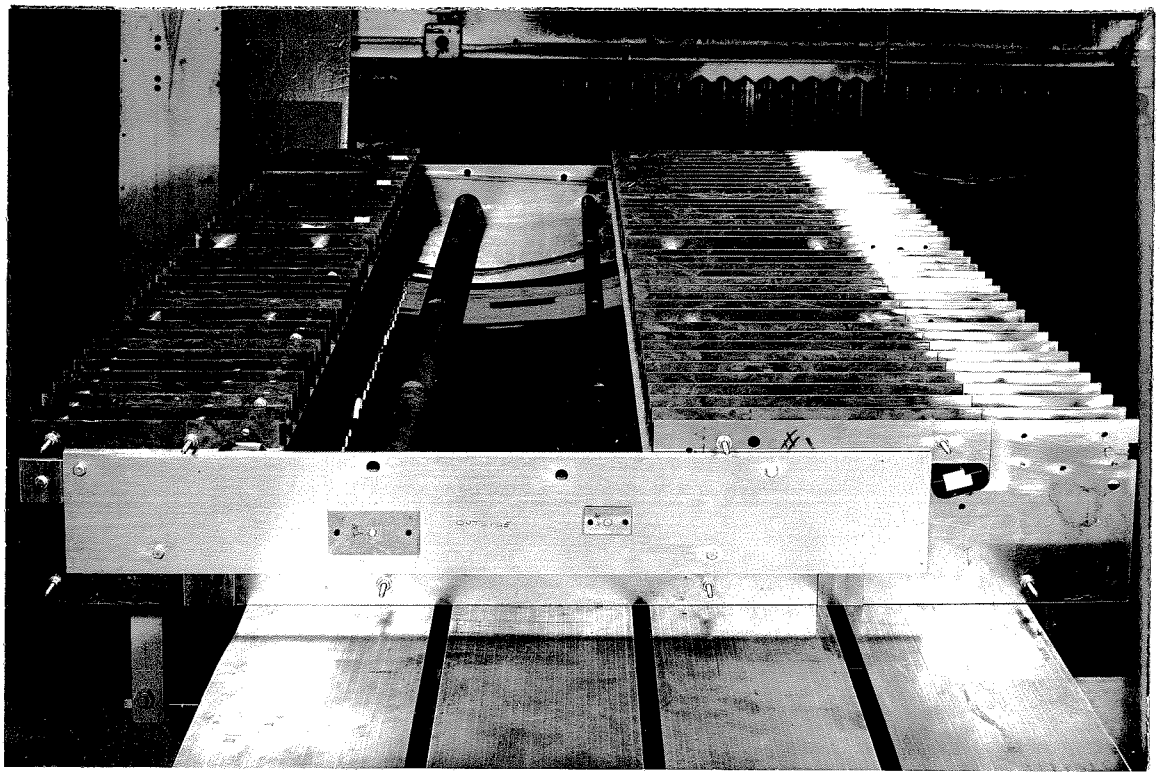

Figure 4. Mold used for fabrication of main airfoil section. Tubular spars are located about 25.5 cm apart.

surface, downstream of the hatch, was hinged at the rear to allow removal of the completed airfoil from the mold. This part of the skin was laid up separately, and details involving ribs and pressure connections were finished. The mold was then closed and the upper and lower skins were bonded at the trailing edge.

Actual fabrication of the wing was done by a commercial vendor who also advised on some details of design. The skin thickness of the main airfoil was approximately 3 mm, with appropriate reinforcement close tc the leading and trailing edges and in the vicinity of the hatch opening. The ends of the airfoil

were approximately 5 mm thick. Eight internal ribs were provided in the main body. Fiberglass-reinforced tubular spars running the length of the span were individually bonded to the internal ribs and to the ends of the model (these spars are visible in Figure 4). The larger spar, located at $x/c = 0.338$, $y/c = 0.056$, was used to transfer the main air load to steel bushings attached to the false walls. The smaller spar, located at $x/c = 0.620$, $y/c = 0.042$, engaged steel pins mounted on plates which could be indexed about the main support to change the angle of incidence.

The hatch cover was heavily reinforced with ribs and stringers, since the pressure surface is loaded in compression if the airfoil is supported from both ends rather than cantilevered. The hatch cover was held in place by means of self-locking flat-head screws distributed around the perimeter. Nuts were epoxied into the main body of the airfoil. The screw heads and joints were covered by thin tape to maintain a smooth surface.

The weight of the finished wing was about 40 kg, low enough for easy handling. The surface was hard and extremely smooth. If we were to use this fabrication technique again, we would probably take care to align the external ribs of the mold a little more precisely. For reasons set out under "Blockage" in Section 3.2 below, and under "Model Coordinates" in Section 4.1, we would also make sure of close contact everywhere between the sheet-metal skin and the external ribs before bonding these components together. The simplest method would be to

use an assembly of matching internal ribs to position the skin during bonding. These are minor details, however; we considered the molded wing to be satisfactory as a test model.

Before it was installed in the tunnel, the assembled wing was mounted in a test fixture and subjected to a distributed proof load of 870 kg. This proof load corresponded to the worst-case condition of maximum attainable lift coefficient and maximum attainable dynamic pressure, and was about six times larger than the actual load during the main experiments of this research.

Pressure Instrumentation. -- Numerous pressure holes of 0.8-mm diameter were drilled in the model. Sixty-five of these were located at mid-span, fifty-five were located at $\frac{1}{4}$-span and again at $\frac{3}{4}$-span, and the remainder were distributed over the span at $x/c = 0.25$. The NACA 4412 section has a finite trailing-edge thickness, and several pressure holes were installed actually in the trailing edge.

One method commonly used to produce pressure holes in wood models, because of the porosity of the material, is to drill an oversize hole and insert a length of metal tubing which extends just beyond the outer surface. The tubing is then fixed in position and the outer surface is hand-worked to a flush surface. This method was unsuitable for the present model, as hand-working destroys the glassy surface obtained with the molded resin. The method adopted was to install hollow brass buttons, 0.8 cm in diameter and 0.3 cm thick, on the inside of the wing at the locations desired for the pressure holes. These buttons

were bonded to the skin by resin. Steel hypodermic tubing extended from the buttons to the open space below the hatch cover. The translucence of the fiberglass-resin material allowed the brass buttons to be located from outside the wing so that pressure holes could be drilled along the local normal to the surface.

Two pressure-scanning valves, driven by 12-step rotary solenoids, were mounted inside the wing. One valve had seven 12-port wafers; the seven output lines were connected to the second valve, which had one 12-port wafer. Altogether, therefore, $7 \times 12 + 5 = 89$ pressures could be connected at one time. The active port on each valve was identified using a voltage source and resistance ladder connected to a switch wafer on the valve shaft. The initial assignment of valve ports (and the only assignment, as it turned out, because of the press of other business), had one port connected to the static-pressure line from the roof-mounted pitot-static tube, 56 ports connected to holes at mid-span (with some duplication as a check on the data), and the remainder connected to holes at the $\frac{1}{4}$- and $\frac{3}{4}$-span locations aft of the 40-percent chord position on the suction side of the airfoil (the location of these holes is detailed in Table 2 below). Pressure holes not connected were sealed internally.

Power was supplied to the rotary solenoids through the main support bushings. Identification voltages were brought out of the model the same way. When the data-acquisition system was in use, the stepping interval for the solenoids was set at

about 20 seconds in an automatic mode. The solenoids could also be controlled manually. The single output line from the pressure-selector system, and the single input line from the roof-mounted pitot-static tube, also passed through the main support bushings.

Tunnel Installation. -- The wing was mounted upside down in the tunnel (lifting downward) because of the peculiar geometry of the flying-hot-wire instrumentation. The airfoil was located with the main support on the tunnel centerline at a distance of 79.3 cm from the beginning of the test section, and the angle of incidence was varied by rotation of the airfoil about this main support. To prevent leakage at the juncture of the wing with the side walls, thin sheets of plastic foam were affixed to the ends of the model. No unusual procedures were used to prepare the wind tunnel for the airfoil experiment, and no screens or other devices were used to improve the quality of the free-stream flow. The free-stream turbulence level under the conditions of the experiment was about 0.7 percent.

## 2.3 The Flying Hot Wire

Traverse, Strut, and Rotor. -- Figure 5 is an outline drawing of the flying-hot-wire apparatus and the airfoil model in the GALCIT 10-foot tunnel. Figure 2 above is a photograph of the actual tunnel installation. The horizontal traverse below the tunnel in Figure 5 is a salvaged lathe bed and carriage. It has a range of about 110 cm and is repeatable to about 0.01 cm. The vertical traverse is a milling-machine slide. It has a range of

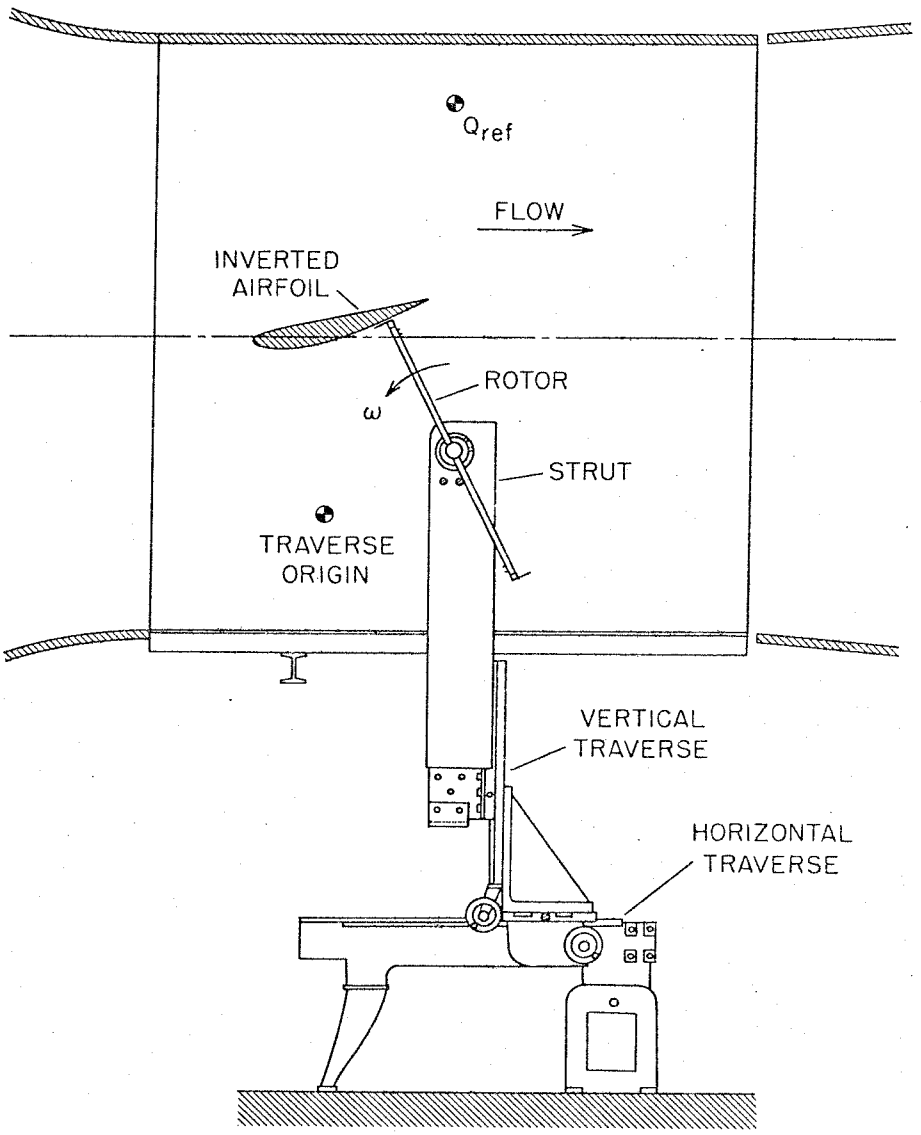


Figure 5. Side view of flying-hot-wire apparatus and traverse in test section of GALCIT 10-foot wind tunnel. Flow is from left to right; rotor rotates counter-clockwise.

36 inches and is repeatable to 0.001 inch. The rotor was supported from the vertical traverse by a strut of heavy rectangular steel tubing. The part of this strut which was exposed to the airflow was streamlined by wooden cladding shaped to an NACA 0024 profile section. The test section of the wind tunnel has a

narrow full-length slot at the bottom which allows traversing in the streamwise direction. The slot was sealed by a cloth strip with two zipper closures running upstream and downstream from the strut.

Mounted in the strut was a flat printed-circuit motor whose axis of rotation was parallel to the airfoil span. The flying-hot-wire rotor was attached directly to the shaft of this motor. Rotor speed was accurately controlled by a phase-locked-loop (PLL) servo system which was designed by B. Cantwell and is described in more detail in CCW. The angular position of the motor shaft was encoded by a 256-tooth precision gear and a magnetic pickup. The pickup provided a clean square-ware TTL signal at 256 pulses per revolution. This ENCODER signal served as feedback input to the PLL phase detector, whose other input originated in a 200-kHz crystal-controlled pulse train. A counter controlled by thumbwheel switches divided this 200-kHz frequency by any desired decimal integer from 1 to 999. The PLL servo system responded smoothly to commands to change speed, and could maintain lock in spite of large variations of torque on the rotor. The presence of lock was monitored by an oscilloscope display of the undemodulated output of the phase-detector circuit.

Hot-wire Probes. -- A commercial hot-wire probe was mounted in a clamp holder at the end of each arm, as shown in Figure 6. A square section machined at the forward end of a sleeve on the probe body mated with a broached recess in the holder to guarantee proper registration of the X-arrays. The

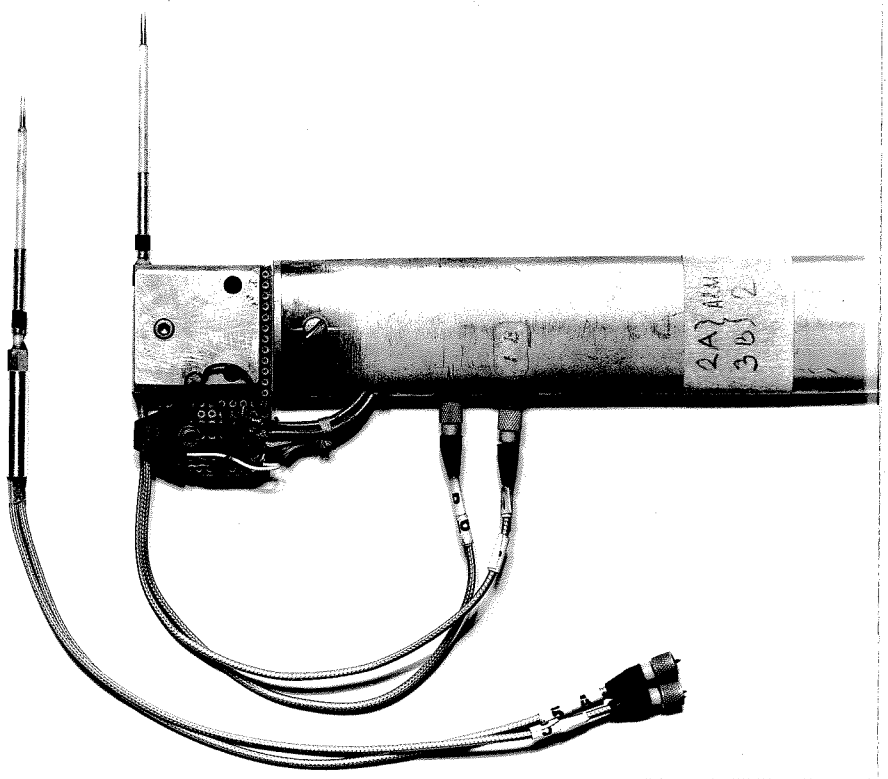

Figure 6. Hot-wire probe installed in end of rotor arm (and spare probe). Scale is about 2/3 actual size; chord of rotor arm is 3.3 cm. Black trapezoidal object in lee of probe clamp is optical proximity sensor.

sensing elements were platinum-plated tungsten wire, five μm in diameter and one mm long. The operating resistance ratio was normally about 1.4 to 1.5. Hot-wire signals were carried through the hollow rotor arms to the hub and thence through the hollow motor shaft to a set of twelve mercury slip rings. Eight rings were required for two X-probes; there were no common leads. The remaining four rings carried power, ground, and signal connections to an optical proximity sensor located on the end of arm 2 (see Section 4.1 below for some uses made of this

sensor). The relatively long hot-wire cables contributed altogether about 35 percent of the total resistance in the active arm of the resistance bridge. Adequate compensation for cable inductance was available in the hot-wire circuitry.

## 2.4 Conventional Instrumentation

Pressure. -- Pressures were measured using two electronic differential manometers. One manometer was permanently connected to the two sides of a pitot-static tube mounted from the tunnel roof to measure a reference dynamic pressure $Q_{ref}$. The point where the static pressure was measured was 29.8 cm below the curved roof and 149.5 cm from the entrance to the test section, as indicated in Figure 3 above. This dynamic pressure $Q_{ref}$ and the associated velocity $q_{ref}$ are used throughout this report whenever pressures or velocities are made dimensionless. The second differential manometer was connected to the pressure-scanning system inside the wing to measure model surface pressure $p_m$. The reference pressure for this manometer was the total pressure from the roof-mounted pitot-static tube (see under "Data Preparation" in Section 4.4 below for a disadvantage of this procedure). Since one pressure input to the pressure-scanning system was from the static side of this same pitot-static tube, the two manometers could be checked against each other by selecting the proper valve port. Agreement in $Q_{ref}$ was usually within one or two parts in a thousand. Both manometers were normally used on a range having 10 volts output for a differential pressure of 30 mm Hg.

Atmospheric pressure was measured using a mercury barometer. Wet- and dry-bulb temperatures were also recorded once or twice a day. To set the tunnel operating condition, the pressure difference between two piezometer rings, one in the supply section and one at the entrance to the test section, was adjusted by the tunnel operator to a value which was known to provide the desired dynamic pressure at a point centered in the empty test section. This particular dynamic pressure is referred to as $Q_{nom}$; it played no part in the data analysis except as a vehicle for repeating a given operating condition.

Temperature. -- An electrical signal representing tunnel temperature was obtained from an electronic thermometer mounted inside the tunnel test section. A mercury thermometer and a vapor-pressure thermometer were used to calibrate the electronic device, whose signal was found to be essentially linear with temperature. Changes in tunnel temperature of more than one degree centigrade during a six-minute data run were unusual.

Intermittency. -- Constant-temperature anemometer circuits were constructed particularly for the present experiments, following a design recommended by Perry and Morrison (1971). Design and fabrication were supervised by A. Perry, who was associated with this research during a study leave at GALCIT, and by B. Cantwell*. The main addition to the design was the incorporation of a hybrid intermittency circuit in each channel.

The conventional definition of intermittency assumes that

*See "Manual for Matilda Meter Constant-Temperature Anemometers", GALCIT, October 1975, by B. Cantwell.

the motion at any point in the flow at any instant can be classified as either turbulent or non-turbulent. In particular, it is common practice to call the motion turbulent if there is appreciable energy at high frequencies. In the present experiments, the classification process was carried out by analog methods in real time. Continuous analog signals from both wires of one X-array were first separately differentiated, to emphasize high frequencies, and then added. The combined signal was band-pass filtered and rectified and fed into a comparator with an adjustable threshold level. The output of the comparator was an irregular pulse train corresponding to portions of the input signal above the threshold level. Each time the flying hot wire passed through turbulent fluid, a burst of such pulses was produced. This burst was fed to a retriggerable one-shot whose output remained high whenever the time interval between input pulses was less than the pulse width of the one-shot. The output of the intermittency circuit was a TTL-compatible digital signal which was continuously available to the data system and was recorded as the least significant bit of each data sample.

Figure 7 is an example of analog input signal and digital output signal for the intermittency circuit. The lower trace shows the (filtered but unrectified) analog signal added electronically to the digital intermittency signal in order to show the quality of the discrimination technique. The relatively weak noise in the early part of the hot-wire trace is associated with the passage of the probe through the turbulent wake of the

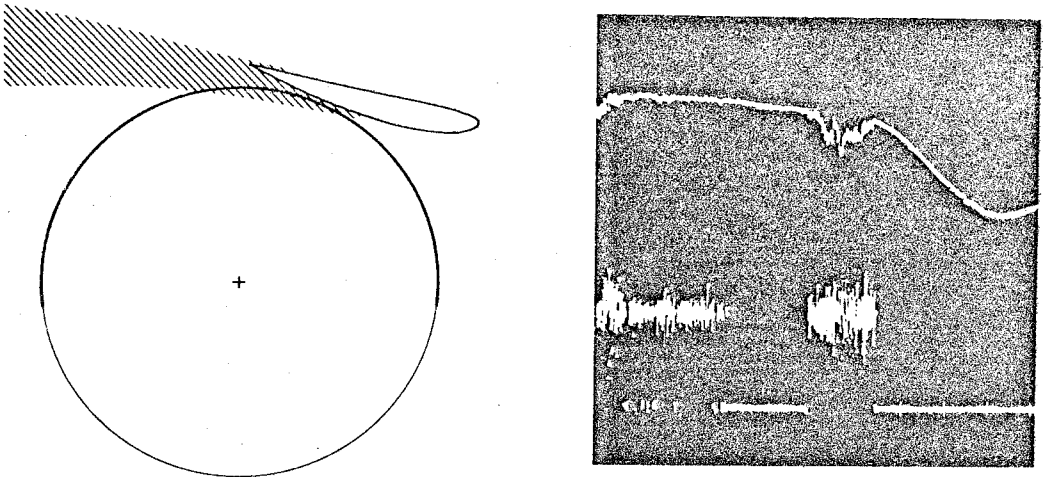

Figure 7. Example of intermittency signal. Upper trace is raw signal from one hot wire during upper half revolution. Time increases from left to right. Lower trace is sum of digital intermittency signal and filtered analog signal. Oscilloscope is triggered by INDEX pulse. Filter passband is 1.0 kHz - 6.3 kHz. One-shot pulse width is 0.4 msec.

preceding rotor arm (see Section 4.2 below, especially Figure 30).

The operation of the intermittency circuit was found to be little affected by changes in filter pass band, at least up to an upper cutoff of 20 kHz, indicating that the hot-wire signals contained useful information up to this frequency. The signals used were always from the wires designated L-0, L-1 (i.e., "last channel minus zero", "last channel minus one"), and were valid for the first half of each revolution only.

The intermittency circuit described here is subject to a difficulty which is common to most such circuits. There is a slight lag in response on leaving a turbulent region, because the retriggerable one-shot remains on for a time equal to its preset pulse width (here about 0.4 msec, or about two-thirds of the

sampling interval). The flying-hot-wire technique has a useful self-correcting property in this situation. Because the probe is moving, so that the mean intermittency data are dynamic rather than static, a plausible a posteriori correction can be made to remove the lag.

The correction treats the mean intermittency surface $\gamma(x, y)$ as a real surface whose slope is a measure of the net rate of interface crossings per unit time. Denote the sampling interval by $\Delta t$ and the preset pulse width of the one-shot by $\tau$. Typical uncorrected mean intermittency data along a probe arc might appear as shown by the open points and the solid line in the sketch at the right in Figure 8. After a displacement backward in time by an amount $\tau$ in regions of decreasing $\gamma$, the same data appear as shown by the dashed line. Now at each data

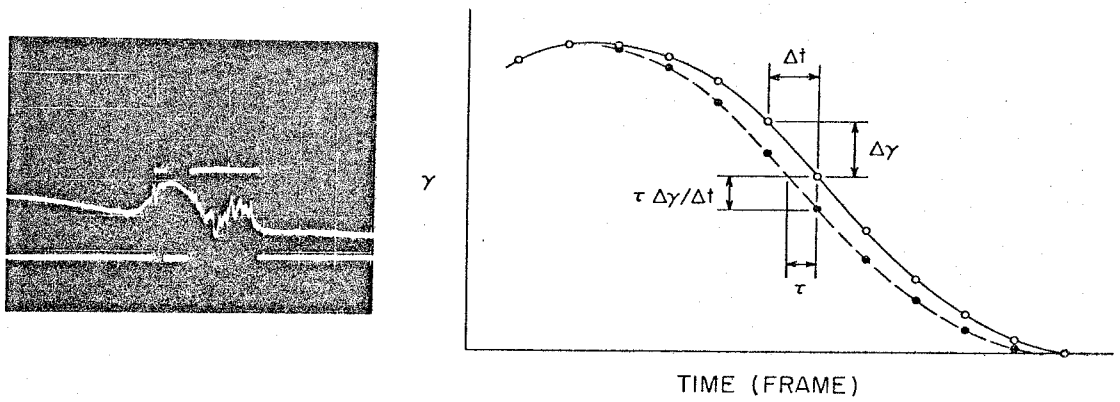


Figure 8. Oscilloscope trace showing raw hot-wire signal and associated intermittency signal, with exit lag. Display is chopped single beam; sweep rate is about 3 msec/cm. Method used to correct mean intermittency data for exit lag is indicated in sketch at right.

station the intermittency circuit indicates turbulent flow for a fraction $\gamma$ of the data samples. Whenever the intermittency is decreasing, the net rate of interface crossings from turbulent to laminar flow per unit time is $-\Delta\gamma/\Delta t$. The number of such crossings in the time interval $\tau$ is $-\tau\Delta\gamma/\Delta t$. This is the number to be subtracted from $\gamma$. It is also the vertical distance between the original (solid) and displaced (dashed) curves in Figure 8. The correction thus amounts simply to displacement of the original time coordinate backward in time by an amount $\tau$ and displacement of the original $\gamma$ downward to the new curve.

2.5 Data Acquisition

Solo System. -- Data from the experiment were recorded by a computer-controlled data-acquisition system. At the time of the main tunnel tests, in March, 1975, the system included computer with 32 K words of core memory, phase-encoded tape transport, removable-cartridge disc, plotter, teletype, paper-tape reader, analog-to-digital converter (16 analog channels, range $\pm$ 10 volts, resolution 14 bits plus sign, maximum rate 400,000 samples/second), and operating-system software.

This data-acquisition system has two unusual but related properties. First, the system is portable. It is in fact moved frequently between a number of experimental sites within the Karman, Guggenheim, and Firestone laboratories. Portability was achieved by mounting the main component (a double-bay rack weighing about 400 kg) on a floating air-cushion platform. Second, the system is normally under the complete and exclusive

control of each experimenter who uses it. This property is explicit in the name "Solo System" which is used to refer to the equipment. There are no computer operators, no data transmission lines, no staff programmers. Everything is (or at least is intended to be) the responsibility of the experimenter.

Programming and Control. -- The Solo System can be programmed in several high-level languages. However, because of the massive data-handling requirements of the flying-hot-wire technique, data acquisition and editing in the present experiment were carried out using stand-alone programs written in assembly language. These programs made no use of the operating system.

There were three main data-acquisition programs. The original program, MSTRY, was designed mainly for hot-wire calibration. This program assumed that an X-array probe was present on each end of the rotating arm. During each half-revolution, two channels of data were recorded from the probe which was currently advancing into the stream. The second program, STALL, was similar except that some editing operations were deleted to accommodate the high rotor speeds used in the airfoil experiment. The third program, PRESS, was also similar to MSTRY, except that rotation was simulated rather than real, and one pair of data channels was recorded continuously rather than two pairs alternately.

Control of data acquisition was shared by data logic circuitry in the flying-arm controller, control logic circuitry in the analog-to-digital converter (ADC), and direct-memory-access

(DMA) circuitry in the computer. Each revolution of the flying arm normally involved 3072 words of data (12 channels, 256 frames). Two 3072-word data buffers in core were used alternately. The computer was instructed to verify, at the end of each revolution, that the buffered data had the correct format and were properly synchronized. During the remaining time the computer was free to edit and dispose of data obtained during earlier revolutions.

Details of the data logic in the flying-arm controller are described in CCW. The main function was to arrange for a burst or frame of N words, spaced at intervals of 5 μsec, to be acquired each time a gear tooth passed the magnetic pickup (N is the number of active analog channels). Thus the ENCODER signal controlled not only the rotor speed, as described under "Traverse, Strut, and Rotor" in Section 2.3 above, but also the timing, and hence the position in the flow, of the hot-wire measurements. The circular trajectory traced out by the hot wires had a nominal diameter of 151.4 cm and a circumference of 475.6 cm. Specification of a 256-tooth gear then implied that digital data would be obtained every 1.86 cm along the arc.

The origin for the angular position of the rotor was an INDEX pulse generated once per revolution, at a time when the rotor arm was approximately horizontal, by a second magnetic pickup and a single-tooth gear on the rotor shaft (for the position of this pulse with respect to the horizontal, see under "Data Placement" in Section 4.1 below). When the computer finished

editing data from the previous revolution, it entered a wait-for-flag loop to await completion of the DMA block transfer for the current revolution. When this transfer was completed, the DMA circuitry inhibited further data transfers. The computer then checked that the INDEX pulse had not yet occurred, verified that the most recent word of data was measured on the last analog channel, set up the DMA circuitry for the next revolution, and entered a second wait-for-flag loop until an INDEX pulse occurred. When this INDEX pulse was detected, the computer activated the DMA channel and the ADC data channel for the new revolution and began editing data acquired during the revolution just completed.

When the computer was first started, status checks were made to verify that the ADC was functioning normally, that the tape transport was on line with a write ring present, and so on. A gap was written on the magnetic tape. The multiplexer was initialized to last channel. The first DMA block transfer from the ADC to core memory was set up but not started. The system then remained in a state of suspended animation until a control line called RUN was set true. The RUN signal was present continuously at the data input of a D-type flip-flop which was clocked by the INDEX pulse. A false output from the flip-flop prevented the ADC from functioning except in response to certain privileged commands from the computer. The data system became armed when RUN was set true manually, and became latched when the next INDEX pulse occurred.

The self-synchronizing properties of the system allowed a data run to be started manually at an arbitrary time after the wind tunnel and the flying arm had reached operating speed. Data from the first revolution were normally free of error. The contents of a revolution counter were displayed continuously on the computer front panel so that progress of the run could be monitored. At the end of the run, an end-of-file mark was automatically written on the tape.

The same control circuitry permitted operation in an alternative mode, in which the flying arm was stationary or absent altogether. A signal generator was used to simulate rotation by supplying a regular pulse train to the ENCODER input at the controller. The program instructions which checked synchronization in terms of the INDEX pulse were deleted. This mode could be used, for example, to record signals from stationary hot wires or other conventional instrumentation (program PRESS).

Error Correction. -- Two errors in data format could occur and, in fact, did occur occasionally. The first error was failure of a DMA block transfer to end on the last ADC channel. The most likely cause was electrical noise in one or another of the counting and sequencing elements in the system. The second error was occurrence of the INDEX pulse before the DMA block transfer was complete. The most likely cause was noise in the ENCODER signal from the magnetic pickup, including dropouts at very low rotor speed. In either case, the data were presum-

ably garbled. However, errors of these two types were considered to be recoverable. The program first executed a restart subroutine to reposition the multiplexer on the last channel (maximum execution time 270 μsec for 12 analog channels), and then waited for an INDEX pulse before activating the DMA channel for a new revolution. The defective data were discarded without editing.

Editing. -- There were several editing operations. In a typical case, the first eight data channels were miscellaneous signals. Voltage samples for these eight signals were accumulated and averaged over the 256 frames of each revolution. The original data were discarded. The particular channel assignments for the main experiments of the present research are listed in Table 1.

Table 1

ADC CHANNEL ASSIGNMENTS

| Channel | Signal |
|---|---|
| 0 | Short circuit |
| 1 | Model static pressure, $p_{t_{ref}} - p_m$ |
| 2 | Tunnel dynamic pressure, $p_{t_{ref}} - p_{s_{ref}}$ |
| 3 | Scanning valve ID voltage 1 |
| 4 | Scanning valve ID voltage 2 |
| 5 | Tunnel temperature |
| 6 | Optical proximity-sensor voltage |
| 7 | Reference voltage |
| 8 | Hot wire L-3 |
| 9 | Hot wire L-2 |
| 10 | Hot wire L-1 |
| 11 | Hot wire L-0 |

ADC channels 0 and 7 were used to record known constant voltages as a check that the data-acquisition system was functioning properly. The pressure and temperature instrumentation connected to channels 1, 2, and 5 have been described in Section 2.4. More information about the optical proximity sensor can be found in Section 4.1 below.

The last four channels were normally reserved for hot-wire data from two X-arrays, one on each arm of the rotor. For a given array, the two wire voltages were measured not quite simultaneously, but 5 μsec apart. This time interval corresponds to a probe motion of about 0.2 mm, or 1/5 of the wire length, and is considered to be negligible, especially as the hot-wire frequency response of 20 kHz limited the resolution of the wires to fluctuations having a period of 50 μsec or more. During each half-revolution, the computer saved <u>verbatim</u> the data from the X-array which was currently advancing into the stream, and discarded the data from the X-array which was currently retreating (programs MSTRY, STALL; see also Figure 30 below). Provided that all wires were present and working, there were therefore two independent observations of the flow over the same 180-degree arc during each revolution. The data after editing consisted of 512 wire voltages together with eight mean values for the miscellaneous signals already described. These eight values were written over the first eight wire voltages, which had little significance because the active probe was passing through the wake of the rotor hub. The word format

was binary integer, 14 bits plus sign, left-justified in the 16-bit computer word. The free least significant bit was used for an intermittency bit obtained from wires L-0, L-1 (see under "Intermittency" in Section 2.4 above).

Two secondary editing operations were transfer of the 512 surviving data words to the appropriate position in one of two tape buffers, and supervision of output to magnetic tape via a second DMA channel. Four revolutions were normally combined into one tape record of 2048 words. No attempt was made to detect or correct writing errors.

Performance. -- Some precise quantitative statements can be made about the load on the data system. The basic clock for the system was a 200-kHz crystal-controlled oscillator. For the airfoil experiment, this clock frequency was divided by 125 to generate a 1600-Hz ENCODER signal. The rotor drive was phase locked to this 1600-Hz signal, as described under "Traverse, Strut, and Rotor" in Section 2.3 above. With a 256-tooth gear, the rotor speed was therefore precisely 6.25 rev/sec or 375 rpm. The 200-kHz clock signal was also used directly to control sampling of 12 data channels at 5-μsec intervals in a burst mode. Such sampling occurred every 625 μsec, at positive-going transitions of the ENCODER signal.

During a run or file, therefore, the ADC rate was 200,000 words per second (wps), intermittent. The mean transfer rate to core was 19,200 wps. The mean transfer rate to magnetic tape was 3200 wps. Each data file lasted for 2048 revolutions

or 327.68 seconds. There are 85 such files in the main data base, representing 89,128,960 words of data on tape and about 7.74 hours of tunnel time (about 13 hours of elapsed time). In this mass of data, one word is known to have been incorrectly recorded, and one tape record out of 43,520 was unreadable (see under "Glitches" in Section 4.3 below).

It may seem foolish to be so precise about some of these numbers. The reason is that we are trying to emphasize the nature of digital techniques when these techniques require keeping accurate books on each word of data, its location and meaning. In the present experiment the analog signals were statistically neither stationary nor homogeneous, and rotor phase was a controlling factor in the sampling process. The experiment was different in kind from experiments which use digital methods primarily for convenience in gaining access to digital filtering algorithms or other numerical data-processing techniques.

## III. CONVENTIONAL MEASUREMENTS

### 3.1 Flow Control

The strategy of the research called for extensive hot-wire measurements at only one angle of incidence and at only one Reynolds number. Suitable values for these two parameters therefore had to be chosen almost at the outset. The measurements by Pinkerton (1938) provided some guidance on the problem of avoiding a laminar separation bubble near the leading edge of the airfoil. Our own observations of surface pressure near the

leading edge at an angle of incidence of 14 degrees, with no boundary-layer trip, showed a definite leading-edge bubble near $x/c = 0.03$ at a Reynolds number of 730,000 (based on chord length c and reference velocity $q_{ref}$), and no bubble at a Reynolds number of 2,100,000. Having in mind the hazards associated with high tunnel speed (e.g., loss of lock in the PLL servo system, shorter life expectancy and lower sensitivity for the hot wires, larger deflections for the model and probe, and reduced effectiveness of the blower intended for flow control), we settled on an intermediate Reynolds number. With a nominal tunnel operating condition of $Q_{nom} = 10$ lbf/ft$^2$, the typical reference velocity $q_{ref}$ and kinematic viscosity $\nu$ for the main experiments were 27.13 m/sec and 0.1605 cm$^2$/sec, respectively. The Reynolds number was 1,523,000.

Boundary-layer Trips. -- To encourage uniform transition over the span, boundary-layer trips were attached to both surfaces of the airfoil. The trips were narrow strips of tape, about 0.15 mm thick and 4 mm wide, with a sawtooth leading edge. On the suction side, the trip was centered at $x/c = 0.025$, slightly downstream from the pressure minimum (this trip is visible in Figures 2 and 13). On the pressure side, the trip was centered at $x/c = 0.103$, well downstream from the stagnation line. Surface pressures measured at 14 degrees immediately after the trips were installed, with no other flow control, are plotted in Figure 9 and are also tabulated in Table 2 (Run 7). Other things being equal, the trips had almost no effect on the

Table 2

SURFACE-PRESSURE DISTRIBUTIONS

| Run No. | | | 38 | 37 | 36 | 35 | 39 | 40 | 79 | 87 | 7 |
|---|---|---|---|---|---|---|---|---|---|---|---|
| $\alpha$ (deg) | | | -4 | 0 | 4 | 8 | 12 | 14 | 16 | 14 | 14 |
| $Q_{ref}$ (mm Hg) | | | 3.62 | 3.44 | 3.28 | 3.17 | 3.08 | 3.08 | 3.19 | 3.13 | 3.09 |
| $C_L$ | | | -0.015 | 0.398 | 0.842 | 1.242 | 1.585 | 1.681 | 1.595 | 1.669 | 1.652 |
| $C_D$ | | | 0.008 | 0.010 | 0.017 | 0.033 | 0.052 | 0.071 | 0.133 | 0.072 | 0.081 |
| Hole No. | $100\frac{x}{c}$ | $100\frac{y}{c}$ | $C_p$ | | | | | | | | |
| 1 | 100.00 | -0.02 | 0.206 | 0.142 | 0.042 | -0.060 | -0.236 | -0.375 | -0.500 | -0.352 | -0.348 |
| 117 | 99.14 | -0.13 | 0.194 | 0.131 | 0.049 | -0.032 | -0.175 | -0.270 | -0.365 | -0.259 | -0.252 |
| 120 | 91.18 | -0.20 | 0.139 | 0.106 | 0.080 | 0.056 | 0.010 | -0.030 | -0.068 | -0.022 | -0.024 |
| 122 | 81.87 | -0.35 | 0.103 | 0.096 | 0.097 | 0.101 | 0.097 | 0.082 | 0.062 | 0.089 | 0.082 |
| 124 | 76.47 | -0.47 | 0.079 | 0.083 | 0.099 | 0.116 | 0.126 | 0.123 | 0.112 | 0.126 | 0.118 |
| 126 | 65.96 | -0.78 | 0.031 | 0.060 | 0.098 | 0.137 | 0.173 | 0.184 | 0.185 | 0.187 | 0.178 |
| 128 | 58.76 | -1.04 | 0.007 | 0.052 | 0.107 | 0.162 | 0.212 | 0.231 | 0.240 | 0.234 | 0.222 |
| 130 | 51.66 | -1.33 | -0.019 | 0.046 | 0.118 | 0.188 | 0.252 | 0.279 | 0.294 | 0.280 | 0.270 |
| 132 | 44.56 | -1.65 | -0.057 | 0.026 | 0.120 | 0.204 | 0.288 | 0.319 | 0.340 | 0.321 | 0.310 |
| 134 | 37.64 | -1.90 | -0.101 | 0.008 | 0.123 | 0.226 | 0.327 | 0.366 | 0.392 | 0.367 | 0.357 |
| 136 | 30.64 | -2.23 | -0.164 | -0.023 | 0.117 | 0.247 | 0.368 | 0.421 | 0.444 | 0.419 | 0.408 |
| 137 | 27.08 | -2.41 | -0.201 | -0.039 | 0.116 | 0.261 | 0.393 | 0.453 | 0.481 | 0.451 | 0.439 |
| 138 | 23.94 | -2.56 | -0.253 | -0.068 | 0.111 | 0.273 | 0.421 | 0.479 | 0.510 | 0.478 | 0.467 |
| 139 | 20.74 | -2.70 | -0.320 | -0.104 | 0.097 | 0.281 | 0.444 | 0.511 | 0.546 | 0.509 | 0.497 |
| 140 | 15.96 | -2.86 | -0.459 | -0.180 | 0.079 | 0.304 | 0.498 | 0.576 | 0.608 | 0.572 | 0.560 |

Table 2 (continued)

| Run No. | | | 38 | 37 | 36 | 35 | 39 | 40 | 79 | 87 | 7 |
|---|---|---|---|---|---|---|---|---|---|---|---|
| 141 | 12.80 | -2.90 | -0.568 | -0.236 | 0.082 | 0.342 | 0.558 | 0.644 | 0.678 | 0.637 | 0.626 |
| 142 | 8.10 | -2.78 | -0.742 | -0.282 | 0.140 | 0.469 | 0.709 | 0.791 | 0.828 | 0.789 | 0.778 |
| 143 | 5.06 | -2.49 | -0.886 | -0.345 | 0.216 | 0.607 | 0.852 | 0.930 | 0.946 | 0.921 | 0.911 |
| 144 | 2.83 | -2.04 | -1.496 | -0.480 | 0.309 | 0.778 | 0.980 | 0.995 | 0.980 | 0.990 | 0.997 |
| 145 | 0.82 | -1.16 | -1.728 | -0.118 | 0.801 | 0.978 | 0.534 | 0.155 | 0.012 | 0.168 | 0.240 |
| 36 | -0.03 | 0.31 | 0.356 | 0.990 | 0.259 | -1.738 | -4.759 | -6.280 | -6.617 | -6.209 | -5.939 |
| 35 | 1.45 | 2.62 | 0.841 | 0.220 | -0.908 | -2.390 | -4.542 | -5.285 | -4.562 | -5.121 | -5.205 |
| 34 | 2.96 | 3.67 | 0.617 | -0.021 | -1.042 | -2.258 | -3.166 | -3.712 | -3.660 | -3.680 | -3.557 |
| 33 | 4.89 | 4.68 | 0.384 | -0.238 | -1.092 | -2.014 | -3.042 | -3.437 | -3.317 | -3.409 | -3.311 |
| 32 | 7.52 | 5.77 | 0.178 | -0.416 | -1.178 | -1.971 | -2.796 | -3.111 | -2.975 | -3.078 | -2.988 |
| 31 | 10.09 | 6.63 | 0.052 | -0.501 | -1.183 | -1.855 | -2.559 | -2.808 | -2.628 | -2.770 | -2.699 |
| 30 | 12.83 | 7.38 | -0.050 | -0.567 | -1.180 | -1.785 | -2.378 | -2.583 | -2.380 | -2.559 | -2.482 |
| 29 | 15.24 | 7.94 | -0.124 | -0.616 | -1.189 | -1.742 | -2.273 | -2.444 | -2.220 | -2.423 | -2.356 |
| 28 | 18.32 | 8.53 | -0.194 | -0.654 | -1.178 | -1.680 | -2.144 | -2.268 | -2.034 | -2.237 | -2.186 |
| 27 | 21.45 | 9.00 | -0.245 | -0.678 | -1.160 | -1.603 | -2.014 | -2.108 | -1.836 | -2.096 | -2.042 |
| 26 | 24.82 | 9.39 | -0.290 | -0.696 | -1.140 | -1.545 | -1.893 | -1.958 | -1.675 | -1.949 | -1.896 |
| 25 | 28.27 | 9.66 | -0.329 | -0.707 | -1.117 | -1.480 | -1.782 | -1.828 | -1.472 | -1.819 | -1.773 |
| 24 | 31.89 | 9.83 | -0.352 | -0.708 | -1.084 | -1.412 | -1.680 | -1.686 | -1.314 | -1.680 | -1.651 |
| 23 | 35.08 | 9.88 | -0.356 | -0.686 | -1.034 | -1.336 | -1.552 | -1.555 | -1.223 | -1.556 | -1.522 |
| 22 | 38.99 | 9.84 | -0.348 | -0.653 | -0.965 | -1.237 | -1.430 | -1.388 | -1.059 | -1.395 | -1.373 |
| 21 | 42.51 | 9.69 | -0.336 | -0.611 | -0.905 | -1.147 | -1.301 | -1.262 | -0.910 | -1.254 | -1.243 |
| 20 | 46.02 | 9.49 | -0.325 | -0.577 | -0.848 | -1.061 | -1.194 | -1.145 | -0.833 | -1.133 | -1.135 |
| 19 | 49.41 | 9.24 | -0.315 | -0.554 | -0.805 | -0.994 | -1.097 | -1.005 | -0.807 | -1.017 | -1.039 |
| 18 | 52.97 | 8.92 | -0.306 | -0.528 | -0.755 | -0.941 | -1.002 | -0.881 | -0.759 | -0.898 | -0.940 |
| 17 | 56.63 | 8.54 | -0.291 | -0.493 | -0.699 | -0.852 | -0.905 | -0.786 | -0.724 | -0.792 | -0.838 |

Table 2 (continued)

| Run No. | | | 38 | 37 | 36 | 35 | 39 | 40 | 79 | 87 | 7 |
|---|---|---|---|---|---|---|---|---|---|---|---|
| 16 | 59.71 | 8.18 | -0.278 | -0.466 | -0.651 | -0.805 | -0.815 | -0.690 | -0.729 | -0.702 | -0.760 |
| 15 | 62.83 | 7.77 | -0.261 | -0.435 | -0.610 | -0.729 | -0.740 | -0.623 | -0.698 | -0.630 | -0.693 |
| 14 | 65.90 | 7.33 | -0.247 | -0.408 | -0.566 | -0.679 | -0.658 | -0.577 | -0.687 | -0.574 | -0.637 |
| 13 | 69.13 | 6.84 | -0.225 | -0.373 | -0.514 | -0.606 | -0.575 | -0.537 | -0.672 | * | -0.578 |
| 12 | 71.98 | 6.37 | -0.204 | -0.342 | -0.471 | -0.548 | -0.512 | -0.503 | -0.665 | -0.493 | -0.536 |
| 11 | 74.27 | 5.97 | -0.184 | -0.318 | -0.436 | -0.498 | -0.464 | -0.489 | -0.669 | * | -0.506 |
| 10 | 78.93 | 5.09 | -0.152 | -0.268 | -0.359 | -0.404 | -0.384 | -0.466 | -0.646 | -0.444 | -0.463 |
| 9 | 83.77 | 4.10 | -0.109 | -0.201 | -0.271 | -0.300 | -0.332 | -0.436 | -0.627 | * | -0.429 |
| 8 | 88.78 | 2.99 | -0.051 | -0.117 | -0.167 | -0.198 | -0.302 | -0.423 | -0.632 | -0.407 | -0.410 |
| 7 | 93.07 | 1.95 | 0.029 | -0.022 | -0.071 | -0.127 | -0.283 | -0.430 | -0.623 | -0.408 | -0.402 |
| 6 | 95.09 | 1.44 | 0.071 | 0.025 | -0.031 | -0.103 | -0.277 | -0.432 | -0.620 | -0.406 | + |
| 5 | 97.41 | 0.83 | 0.118 | 0.075 | 0.008 | -0.081 | -0.267 | -0.432 | -0.590 | -0.402 | -0.411 |
| 4 | 98.56 | 0.52 | 0.155 | 0.106 | 0.025 | -0.075 | -0.267 | -0.421 | -0.569 | -0.397 | -0.411 |
| 2 | 100.00 | -0.02 | 0.204 | 0.138 | 0.044 | -0.058 | -0.237 | -0.374 | -0.478 | -0.353 | -0.338 |
| 52 | 41.83 | (orifices at $\frac{1}{4}$-span) | | | | | | | -0.732 | -1.253 | -1.027 |
| 51 | 45.81 | | | | | | | | -0.762 | -1.089 | -0.861 |
| 50 | 50.11 | | | | | | | | -0.695 | -0.965 | -0.758 |
| 49 | 54.12 | | | | | | | | -0.716 | -0.842 | -0.685 |
| 48 | 58.57 | | | | | | | | -0.696 | -0.732 | -0.657 |
| 47 | 62.39 | | | | | | | | -0.685 | -0.639 | -0.645 |
| 46 | 65.95 | | | | | | | | -0.718 | -0.580 | -0.635 |
| 45 | 69.58 | | | | | | | | -0.658 | -0.536 | -0.627 |
| 44 | 73.04 | | | | | | | | -0.696 | -0.507 | -0.618 |
| 43 | 75.27 | | | | | | | | -0.649 | -0.492 | -0.605 |

Table 2 (concluded)

| Run No. | 38 | 37 | 36 | 35 | 39 | 40 | 79 | 87 | 7 |
|---|---|---|---|---|---|---|---|---|---|
| 42 | 80.14 | | | | | | -0.712 | -0.469 | -0.586 |
| 41 | 84.26 | | | | | | -0.690 | -0.459 | -0.575 |
| 40 | 90.66 | | | | | | -0.681 | -0.442 | -0.567 |
| 39 | 92.40 | | | | | | -0.647 | -0.440 | -0.552 |
| 38 | 97.18 | | | | | | -0.603 | -0.439 | -0.527 |
| 37 | 100.00 | | | | | | -0.490 | -0.371 | -0.450 |
| 81 | 39.72 | (orifices at $\frac{3}{4}$-span) | | | | | -0.963 | -1.364 | -1.119 |
| 80 | 43.18 | | | | | | -1.071 | -1.230 | -0.964 |
| 79 | 46.95 | | | | | | -0.905 | -1.101 | -0.841 |
| 78 | 50.59 | | | | | | -0.784 | -0.985 | -0.775 |
| 77 | 54.17 | | | | | | -0.775 | -0.877 | -0.720 |
| 76 | 57.62 | | | | | | -0.723 | -0.788 | -0.696 |
| 75 | 61.46 | | | | | | -0.683 | -0.690 | -0.680 |
| 74 | 65.57 | | | | | | -0.673 | -0.610 | -0.670 |
| 73 | 68.70 | | | | | | -0.668 | -0.563 | -0.663 |
| 72 | 73.27 | | | | | | -0.596 | -0.511 | -0.645 |
| 71 | 77.53 | | | | | | -0.586 | -0.482 | -0.639 |
| 69 | 86.30 | | | | | | + | + | + |
| 68 | 90.64 | | | | | | + | + | + |
| 67 | 96.52 | | | | | | + | + | + |
| 66 | 100.00 | | | | | | -0.491 | -0.372 | -0.477 |

* Intermittent leak in pressure-scanning valve
\+ Pressure-scanning valve skipped these ports

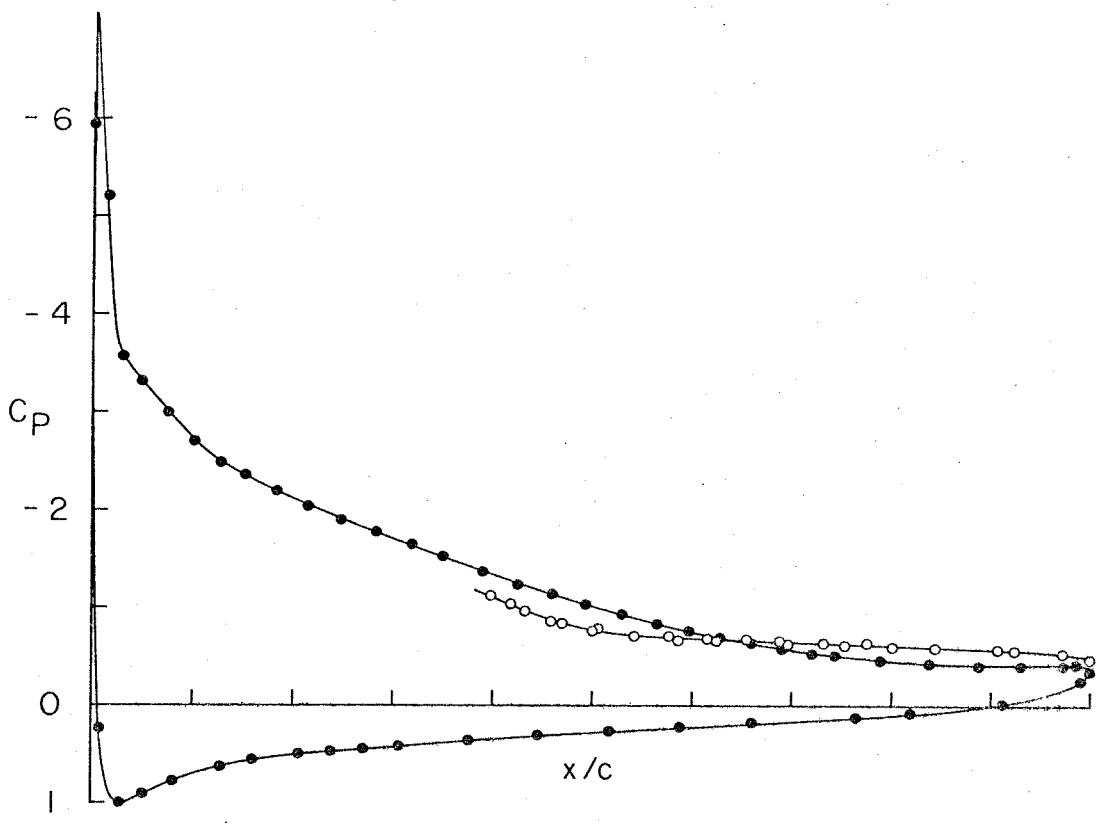


Figure 9. Surface-pressure distribution at 14 degrees angle of incidence, with no flow control (Run 7). Solid symbols: data at midspan. Open symbols: data at $\frac{1}{4}$- and $\frac{3}{4}$-span.

pressure distribution, even near the leading edge. At midspan, according to Figure 9, trailing-edge separation occurred at about x/c = 0.7. At $\frac{1}{4}$-span and $\frac{3}{4}$-span, however, separation occurred at or before x/c = 0.5. Thus there was a streamwise displacement of the separation line of about 20 cm in a spanwise distance of 50 cm. This evidence of severe three-dimensionality made the flow in question a poor prospect as a vehicle for detailed hot-wire measurements. A program of flow control was therefore begun.

Active Flow Control. -- To obtain a rapid indication of any progress being made in improving the two-dimensionality of the mean flow, three vertical total-pressure rakes were placed across the wake. The rakes were about 115 cm downstream from the trailing edge of the airfoil and were in line with the surface-pressure orifices at $\frac{1}{4}$-, $\frac{1}{2}$-, and $\frac{3}{4}$-span. Figure 1 above is a photograph of the rake installation. Rake total pressures were read manually on a multiple-tube manometer bank using butyl alcohol as manometer fluid. The readings were not made with particular care, because the object at the time was not to document the flow but only to improve it.

Methods tried for active flow control included suction or blowing through perforated plates (61 by 24 cm; 30 percent open) placed in the false walls in the vicinity of the separated region, and also two-dimensional blowing using slot jets directed downstream along the false walls from about the airfoil trailing edge. In the present instance none of these methods was effective, although they have apparently served well in other research (see, for example, de Vos 1973). Our blower was probably undersized, and the structural design of the false walls restricted the location of our flow-control devices. Two examples of unacceptable wake flow are shown at the left in Figure 10. The first example, Run 12, shows the worst flow ever observed. The perforated plates were present, but the blower was off, so that flow was permitted through the walls. Downstream of the airfoil at midspan, the wake was about 35 cm thick. At the two lateral

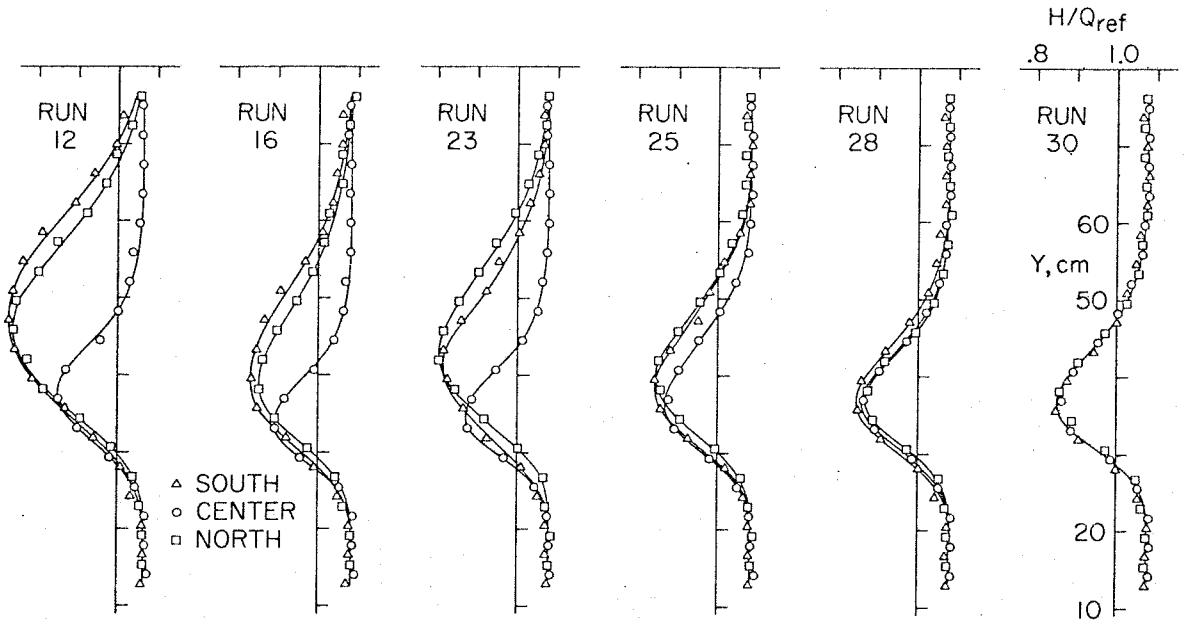


Figure 10. The struggle to achieve two-dimensional mean flow in the wake. All data are for 14 degrees angle of incidence and $Q_{nom}$ = 10 lbf/ft$^2$. H is total pressure in wake (referred to atmospheric pressure) as measured about 1.28 chords downstream of trailing edge. Origin for Y is 64.3 cm from tunnel center line; airfoil is lifting in direction of increasing Y.

Run 12 Perforated plate, blower off.
Run 16 Slot jet, blower on.
Run 23 Perforated plate, blower off, flow guides at +3°.
Run 25 Slot jet, blower off, flow guides horizontal.
Run 28 Slot jet, blower off, flow guides at -3°.
Run 30 Solid wall, flow guides at -3°.

stations, 50 cm to each side, the wake thickness increased to about 60 cm, with an appreciably larger momentum deficit. The second example in Figure 10, Run 16, shows the best flow obtained with the available blower and with the most effective method of active control, which was slot blowing.

Passive Flow Control. -- In the uncontrolled flow, interaction between the boundary layers on the airfoil and on the side

walls apparently led to premature separation and to the appearance of large trailing vortices (having the same sense as tip vortices for a wing of finite span) which greatly thickened the wake near the side walls. It occurred to us that the entire flow might be improved if the flow near the walls could be forced to take the direction wanted at midspan. After Run 19, therefore, in what was essentially a measure of desperation, flow guides of sheet metal were attached to each wall. The guides were 51 cm long and extended 10 cm out from the wall. The leading edges were level with the lowest point of the airfoil, and the trailing edges were directly below the airfoil trailing edge (see Figure 22b below). The guides were tested at different angles of incidence measured with respect to the tunnel axis. Various methods of active flow control were also tried in combination with this passive method, as indicated by some examples in Figure 10. The final configuration, Run 30, at the right in the figure, used only passive control, with the guides pitched about 3 degrees oppositely to the airfoil. The two-dimensionality of the wake over the central 100 cm of span was markedly improved, with an essentially constant wake thickness of about 35 cm.

Surface pressures measured on the airfoil at 14 degrees angle of incidence with the flow guides in their final configuration are shown in Figure 11 and are tabulated in Table 2 (Run 87; cf. also Run 40). Comparison with Figure 9 confirms that improved two-dimensionality in the wake was accompanied by improved two-dimensionality near the airfoil. It is remarkable

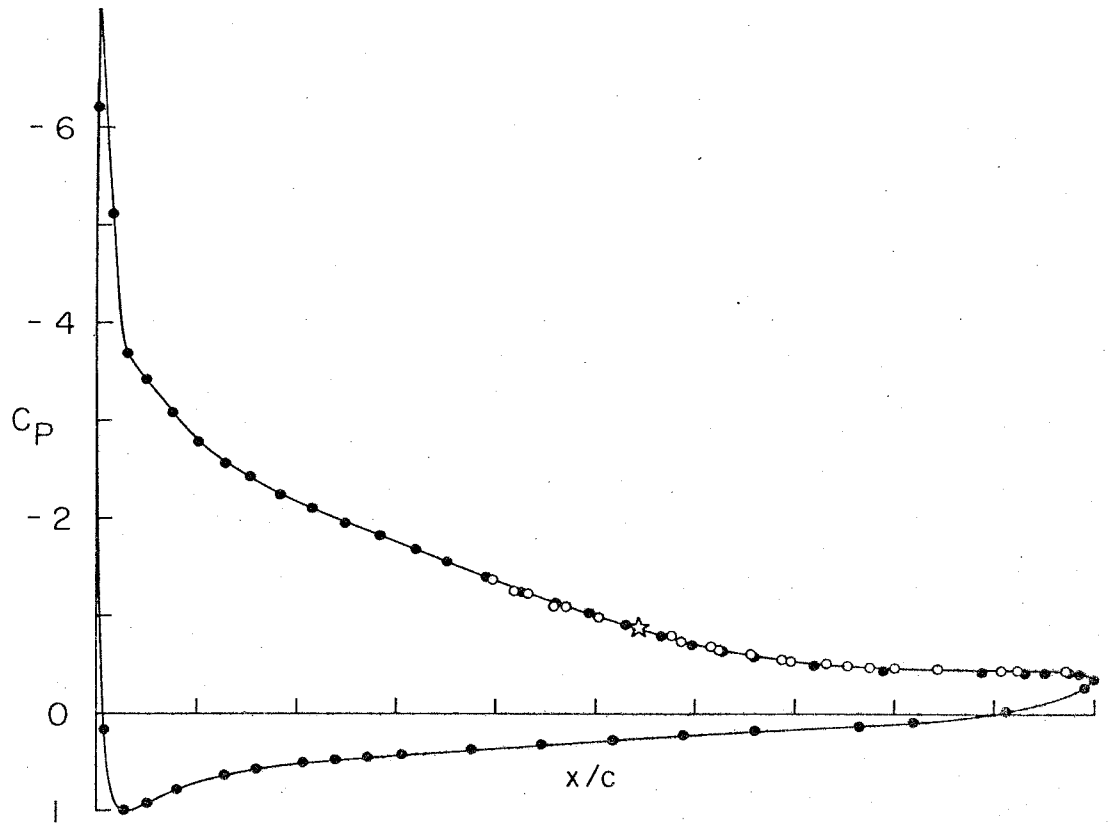


Figure 11. Surface-pressure distribution at 14 degrees angle of incidence, with flow guides in optimum position (Run 87). Solid symbols: data at midspan. Open symbols: data at $\frac{1}{4}$- and $\frac{3}{4}$-span. For pressure variation with time at starred point, see Figure 17b.

that pressures measured at midspan were not much affected, either on the airfoil or in the wake, by large changes taking place in the flow near the side walls.

To test the quality of the flow in a different way, some rather unprofessional flow visualization was carried out at the very end of the experiments. A photograph of the pattern left near the trailing edge by a kerosene-talcum powder mixture is shown in Figure 12. The airflow is from bottom to top. The

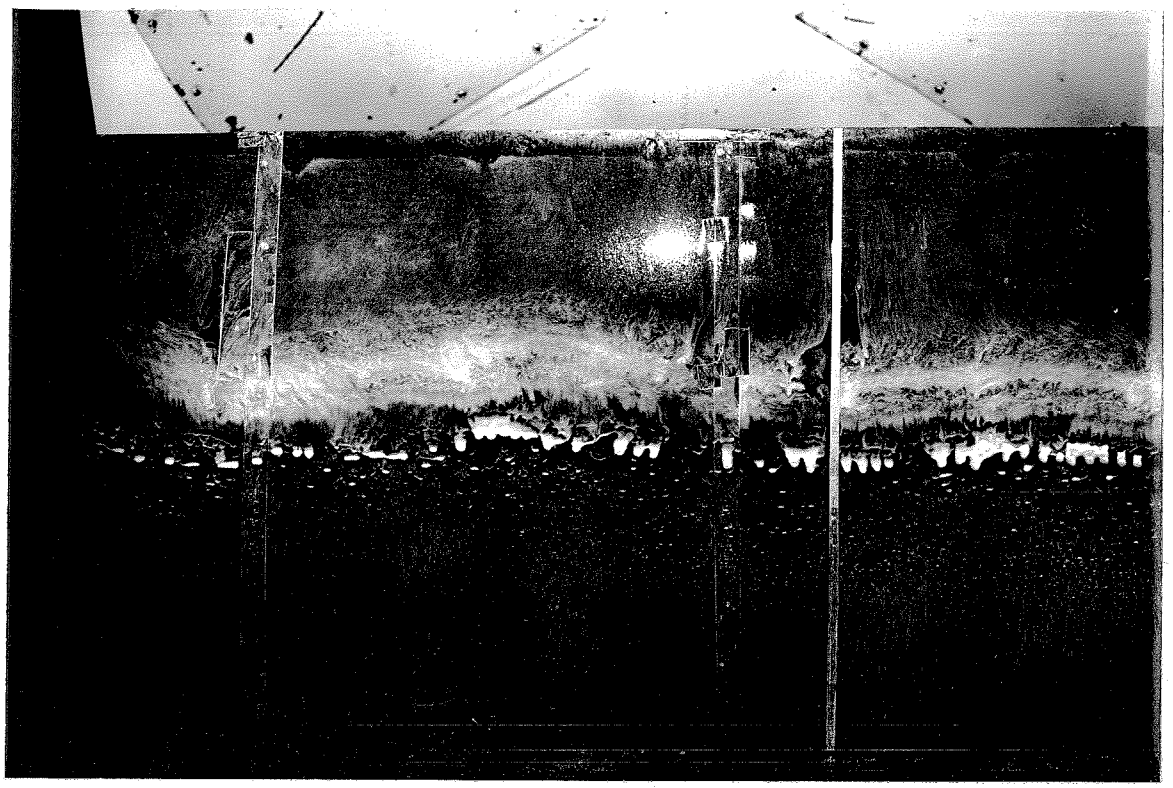

Figure 12. Visualization of surface flow pattern during main hot-wire measurements, using mixture of kerosene and talcum powder. Flow direction is from bottom to top. Photograph shows rear 70 cm of 90-cm chord and about 130 cm of 200-cm span. At probe station (bright vertical line), separation is indicated by accumulation of powder at about $x/c = 0.67$. White tears are excess liquid flowing under gravity (tunnel is off).

photograph shows an area about 70 cm by 130 cm; the transparent tape protecting the pressure holes at the very bottom of the photograph is at $x/c = 0.25$. The bright vertical line is a strip of reflecting tape used with an optical proximity sensor, as described in Section 4.1 below. This line marks the path of the hot-wire probe, 11 cm from midspan. The pattern suggests that

the separation line was reasonably straight and that the mean flow direction near the surface in the separated region was nearly upstream. Much less regular patterns have sometimes been observed in similar circumstances (see, for example, Gregory, Quincey, O'Reilly, and Hall 1971).

A photograph of one of the flow guides in its final position is shown in Figure 13. Tuft studies showed the flow to be

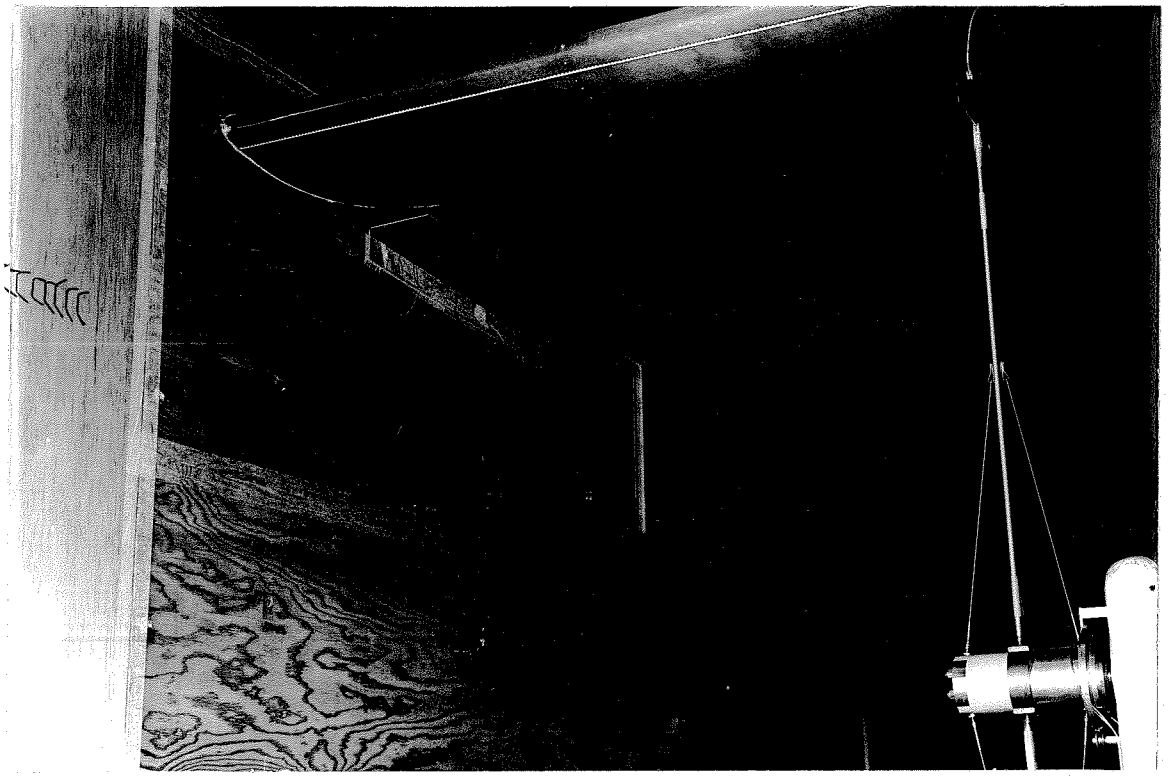

Figure 13. View of flow guide in final position on side wall. Rotor is clamped in vertical position with Kiel probe mounted in place of hot-wire probe. Upper rectangle on wall behind flow guide is plenum chamber for flow control; lower rectangle is window.

attached to the outer surface of the flow guides and to the side walls outside the guides, but violently separated inside. We suspect that the slight angle of incidence was important, and that it caused the flow guides to act like vortex generators whose shed vorticity interfered favorably with the secondary vorticity of the same sense generated in the wing-wall interaction.

In summary, the strategy of passive flow control was entirely successful. It was a blessed byproduct of this success that the blower was not needed, as the noise level from the blower was very uncomfortable. A similar strategy might be useful as a means for improving two-dimensionality for other flow configurations, such as flow over a backward-facing step.

Other Findings. -- Finally, the airfoil was pitched through the range from -4 degrees to 16 degrees, and the wake profiles were found to remain essentially two-dimensional, as demonstrated in Figure 14. One important constraint on the location of the flow guides, incidentally, was that they should not interfere physically with the airfoil as the latter was pitched through at least this range. Two sketches of the model, flow guides, and wake are shown in Figure 15 to illustrate the point.

Note that Figure 14 shows a gradual change in the value of the dependent variable $H/Q_{ref}$ in the free stream as the angle of incidence changes. In Figure 14, as in Figure 10, the quantity H is total pressure referred to atmospheric pressure. The static pressure at the rake position was not measured, but was evidently slightly less than atmospheric pressure at low

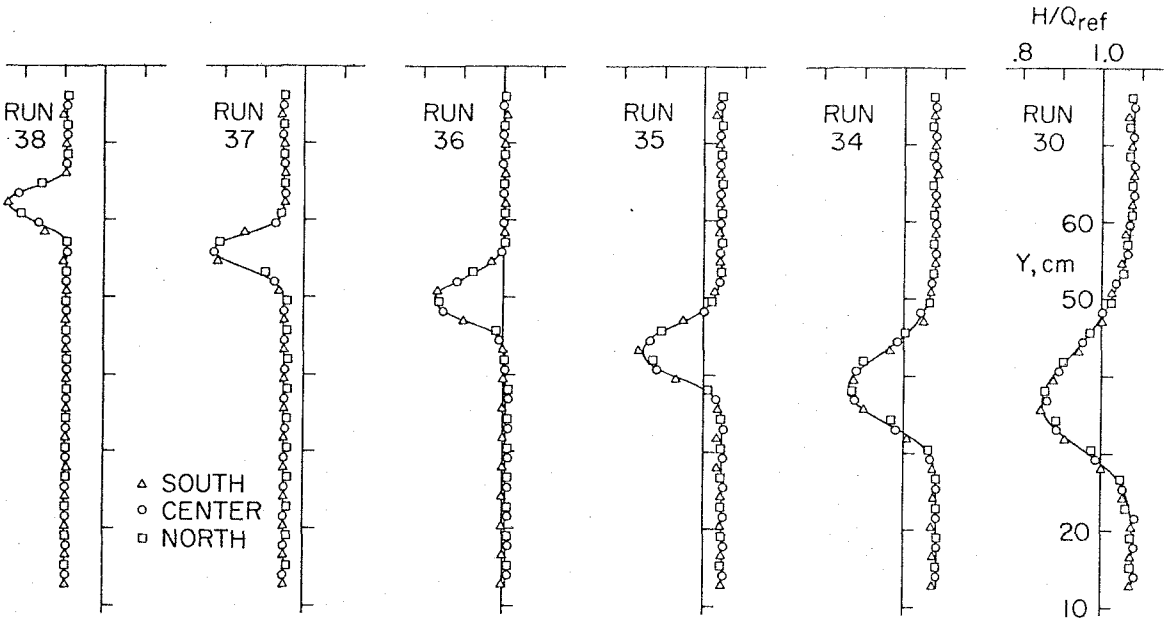


Figure 14. Two-dimensionality of wake for various angles of incidence, with flow guides in optimum position; $Q_{nom}$ = 10 lbf/ft$^2$ (cf. Figure 10). Origin for Y is 64.3 cm from tunnel center line; airfoil is lifting in direction of increasing Y.

Run 38 Airfoil at -4 degrees (angle for zero lift)
Run 37 Airfoil at 0 degrees
Run 36 Airfoil at 4 degrees
Run 35 Airfoil at 8 degrees
Run 34 Airfoil at 12 degrees
Run 30 Airfoil at 14 degrees (angle for main experiments)

angles of incidence and slightly greater at high angles.

There are no wake data in Figure 14 for an airfoil angle of incidence of 16 degrees, although this angle was included in the preliminary flow study and was expected to be a strong candidate for the main experiments because of the more fully developed stall. The problem was that the flow for this angle of incidence was grossly unsteady. For practical purposes, the

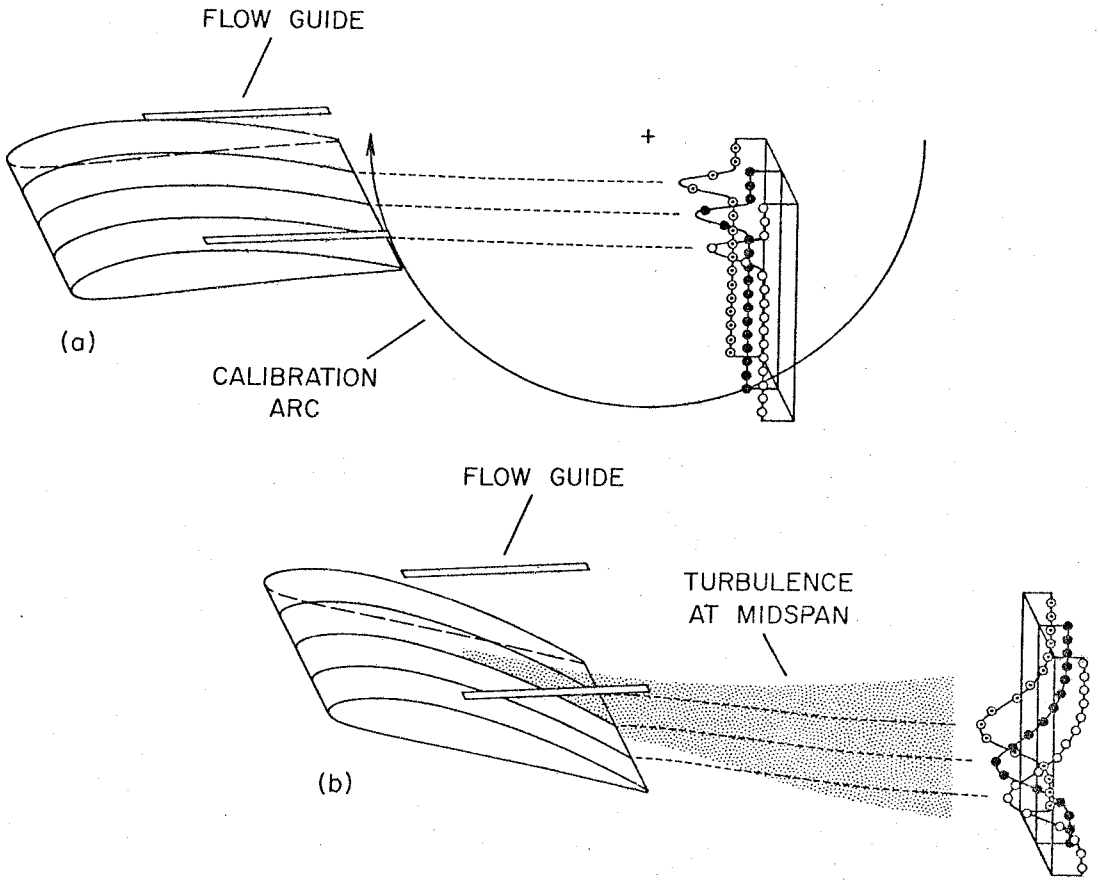


Figure 15. Configuration of model and wake (a) during probe calibration and (b) during main experiments. View is inverted from actual orientation in tunnel. Note clearance between flow guides and airfoil.

flow was out of control. The wake tended to be abnormally thick on one side of the center plane and abnormally thin on the other side. This situation would continue for perhaps 10 to 20 seconds and then reverse. It was not possible to record usable values for mean total pressure in the wake by manual methods. However, the pressure on the airfoil itself was eventually recorded with the aid of the data system (Run 79), with the result listed in Table 2 and plotted in Figure 16. The variation of pressure

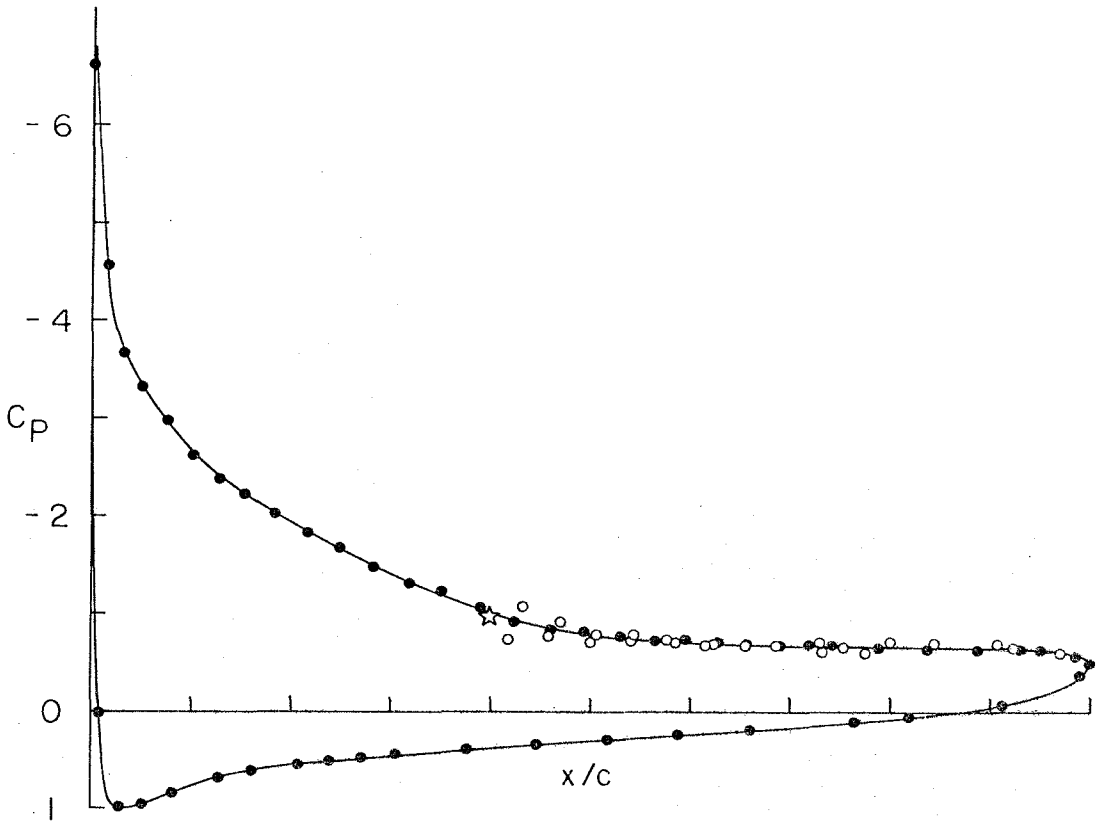


Figure 16. Surface-pressure distribution at 16 degrees angle of incidence, with flow guides in optimum position (Run 79). Solid symbols: data at midspan. Open symbols: data at $\frac{1}{4}$- and $\frac{3}{4}$-span. For pressure variation with time at starred point, see Figure 17a.

with time at the starred station in Figure 16, close to the mean separation position at $\frac{3}{4}$-span at 16 degrees, is compared in Figure 17 with a similar but much steadier record at 14 degrees. The plotted data are local averages over about $\frac{1}{4}$-second, to suppress high frequencies. The time constant for the pressure system was about two seconds.

We were not expecting a global instability of this kind, and were glad to receive a partial explanation from M. Gaster

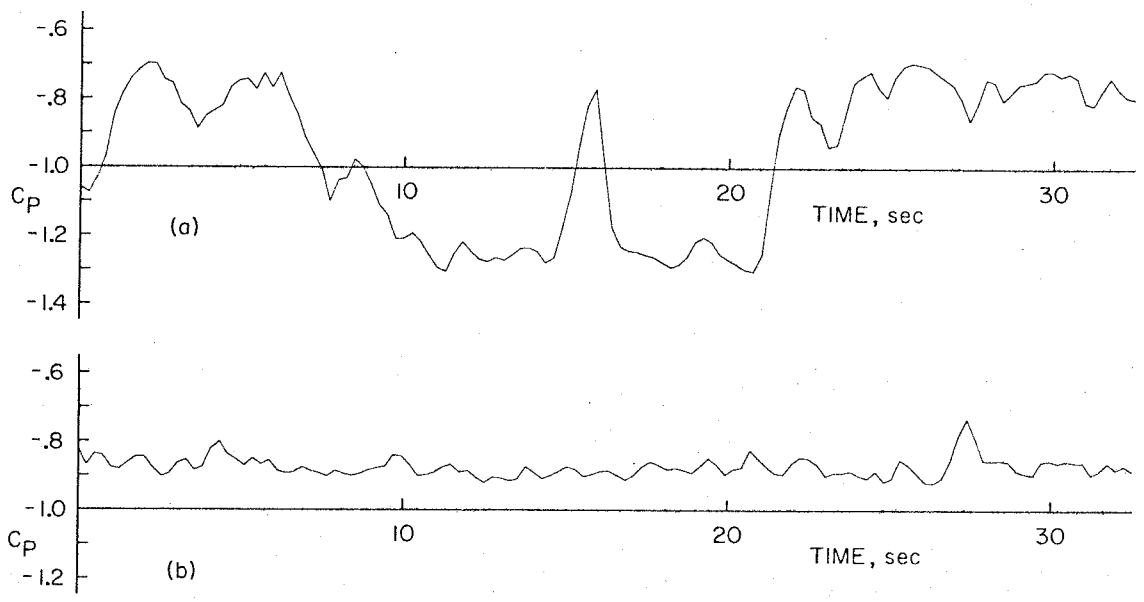


Figure 17. Comparison of grossly unsteady flow beyond stall with relatively steady flow at maximum lift.

(a) Unsteady flow at starred point in Figure 16 (Run 79); $\alpha$ = 16 degrees, x/c = 0.397, mean $C_p$ = -0.963.

(b) Steady flow at starred point in Figure 11 (Run 87); $\alpha$ = 14 degrees, x/c = 0.542, mean $C_p$ = -0.877.

during a private discussion of the present experiments. The argument is illustrated in Figure 18, which is a view of the flow looking along the tunnel axis. Suppose that the distribution of lift (i.e., circulation) is momentarily non-uniform. The associated trailing vorticity will induce a downwash velocity which reduces the angle of attack where the lift is large and increases the angle of attack where the lift is small. If a larger angle means a larger lift, the situation is stable, and will tend toward uniform lift. However, if a larger angle means a smaller lift--if $dC_L/d\alpha$ is negative--the non-uniformity in

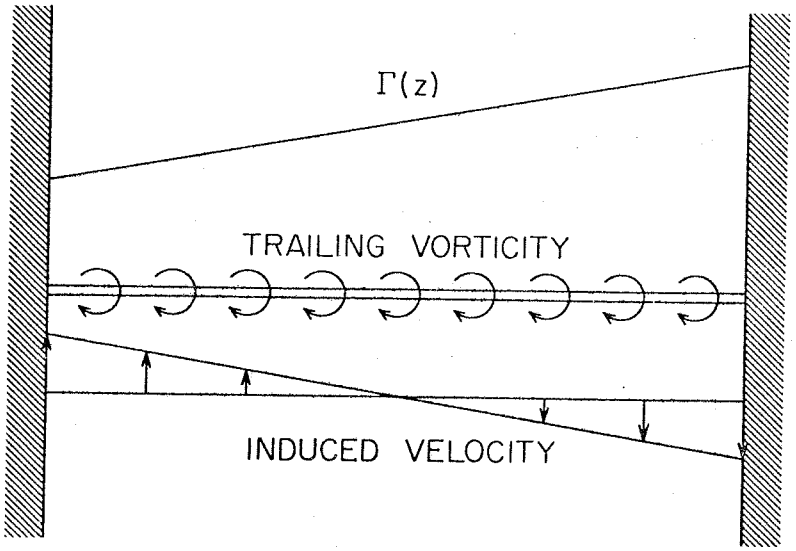


Figure 18. Sketch to illustrate instability mechanism for flow beyond stall.

circulation is reinforced, and produces what in steady flow is often called a stall cell. Our flow was unsteady, with the whole tunnel circuit involved in something resembling a Dutch-roll oscillation. It may be that the unsteadiness occurs only for a compound test section. In any case, we recommend that other experimenters be on guard.

3.2 Airfoil Performance

Lift and Drag. -- During the rest of the experiment, the flow guides were left fixed at the optimum position determined during the wake measurements just described. At angles of incidence from -4 degrees to 16 degrees, lift and drag coefficients were obtained from surface-pressure distributions recorded by the data system and listed in Table 2. One group of such measurements has already been cited in Figure 14. These

runs provided surface-pressure data at midspan only, with the wake rake still present downstream of the wing and with the strut and rotor not yet installed. At the two higher angles of incidence cited in Figures 11 and 16, complete pressure surveys were made after the rake was removed. In both cases the strut and rotor were present, with the rotor clamped in the vertical position. Run 79, at 16 degrees, was made just before the main hot-wire measurements, with the traverse system set at the standard position for probe calibration; i.e., X = 122 cm, Y = 28 inches (see Figure 26 below for the meaning of these coordinates). Run 87, at 14 degrees, was made after the main hot-wire measurements had been completed and the entire traverse system had been moved 66 cm downstream to prepare for measurement of pressure and velocity along the probe calibration arc. We consider the data from this Run 87 to be free of any substantial flow interference due to the presence of the strut and rotor in the test section (see Section 5.1 below for a discussion of the interference problem).

The various pressure distributions tabulated in Table 2 are compared in Figure 19 with measurements by Pinkerton (1938, Table If, Re = 3,400,000; same actual Re). The effective Reynolds numbers quoted by Pinkerton are the actual Reynolds numbers multiplied by a factor of 2.64 (a factor apparently obtained from sphere drag measurements, in the fashion of that time) to account for tunnel turbulence. Lift and drag coefficients obtained by integration of our own pressure data are listed at

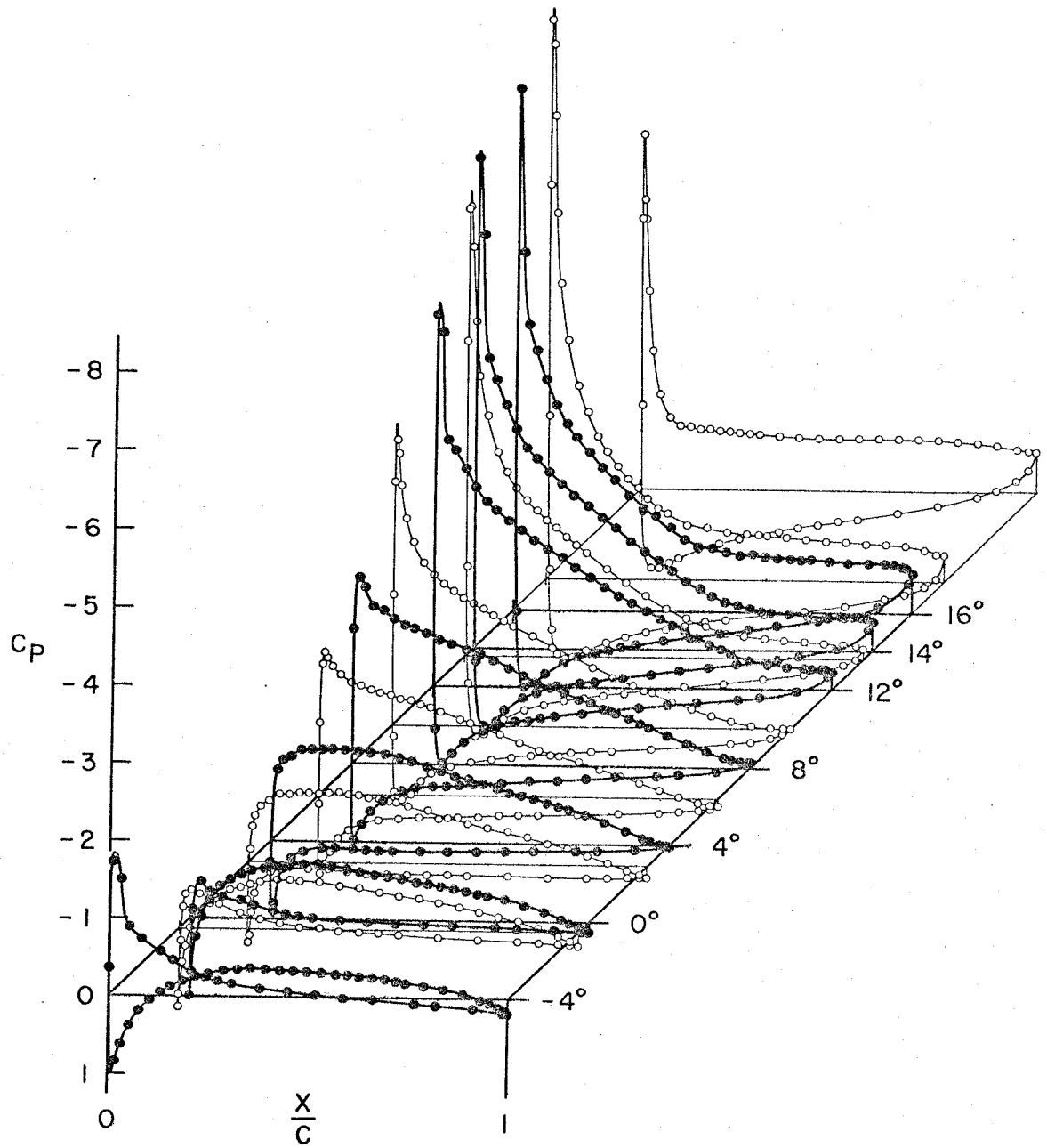


Figure 19. Measured surface-pressure distributions at mid-span. Solid symbols: present data, Table 2. Open symbols: data from Pinkerton (1938), Table If.

the top of Table 2 and are compared in Figure 20 with some of Pinkerton's data (Table IIg, Re = 6,300,000; same $C_{L_{max}}$).

Pinkerton's values were obtained by integrating pressure distributions at midspan for a finite rectangular wing of aspect ratio 6. Pinkerton made a rough correction for induced downwash velocity at midspan, but Figure 20 suggests that the correction may have been too small, especially at large angles of attack.

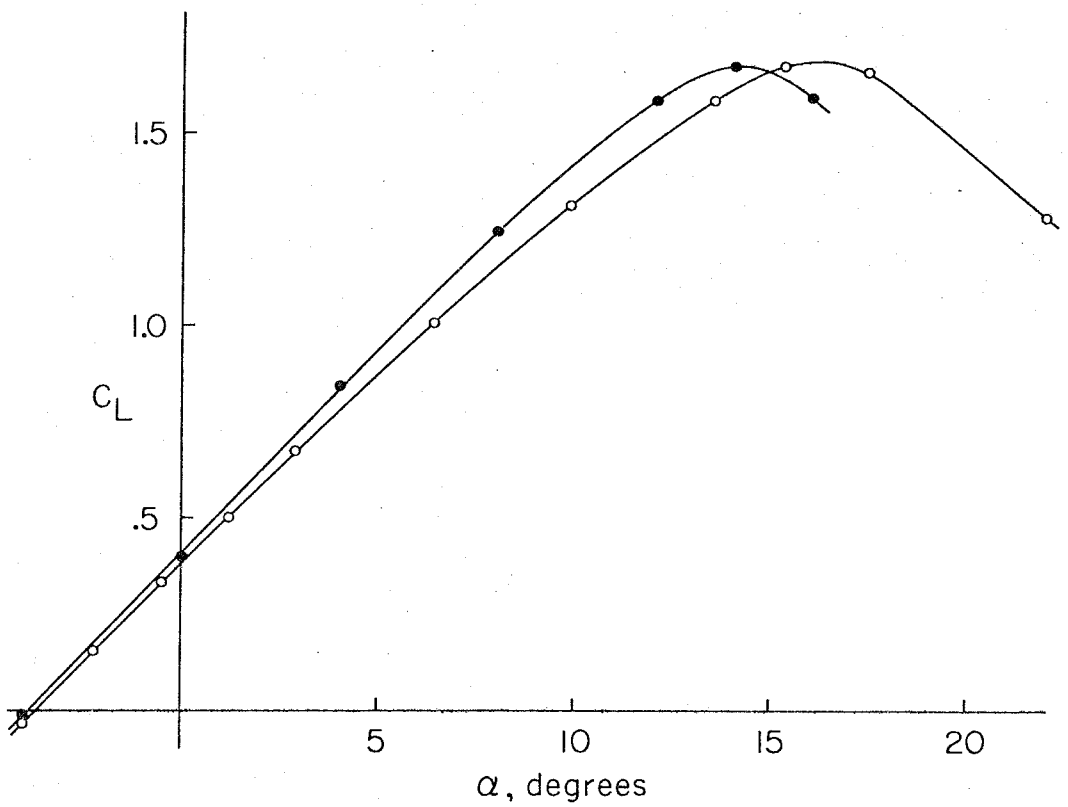


Figure 20. Section lift coefficient as a function of angle of attack. Solid symbols: present data, Table 2. Open symbols: data from Pinkerton (1938), Table IIg.

Because three-dimensional effects are almost absent in the present measurements, (the slope $dC_L/d\alpha$ for small angles of incidence in Figure 20 is very close to $2\pi$ per radian), the pressure distributions and section properties in Table 2 may be valuable in themselves for development or test of simple calculation methods.

Blockage. -- Figure 21 compares pressure distributions observed near zero lift and near maximum lift for the two experiments. As always, the present data are made dimensionless using the static and dynamic pressure indicated by the roof-mounted pitot-static tube; thus

$$C_{p_{ref}} = \frac{p - p_{s_{ref}}}{Q_{ref}} \qquad (6)$$

If the same model were imagined to be in an infinite stream, the corresponding definition would be

$$C_{p_\infty} = \frac{p - p_{s_\infty}}{Q_\infty} \qquad (7)$$

Provided that the total pressure is the same for the two situations, these definitions imply

$$C_{p_\infty} - 1 = \frac{Q_{ref}}{Q_\infty}(C_{p_{ref}} - 1) \qquad (8)$$

A blockage correction usually represents an attempt to estimate the factor $Q_{ref}/Q_\infty$ in Equation (8), and thus a scale change for the quantity $C_p - 1$. Such a correction ignores the fact that walls may significantly change the nature of the local flow, particularly

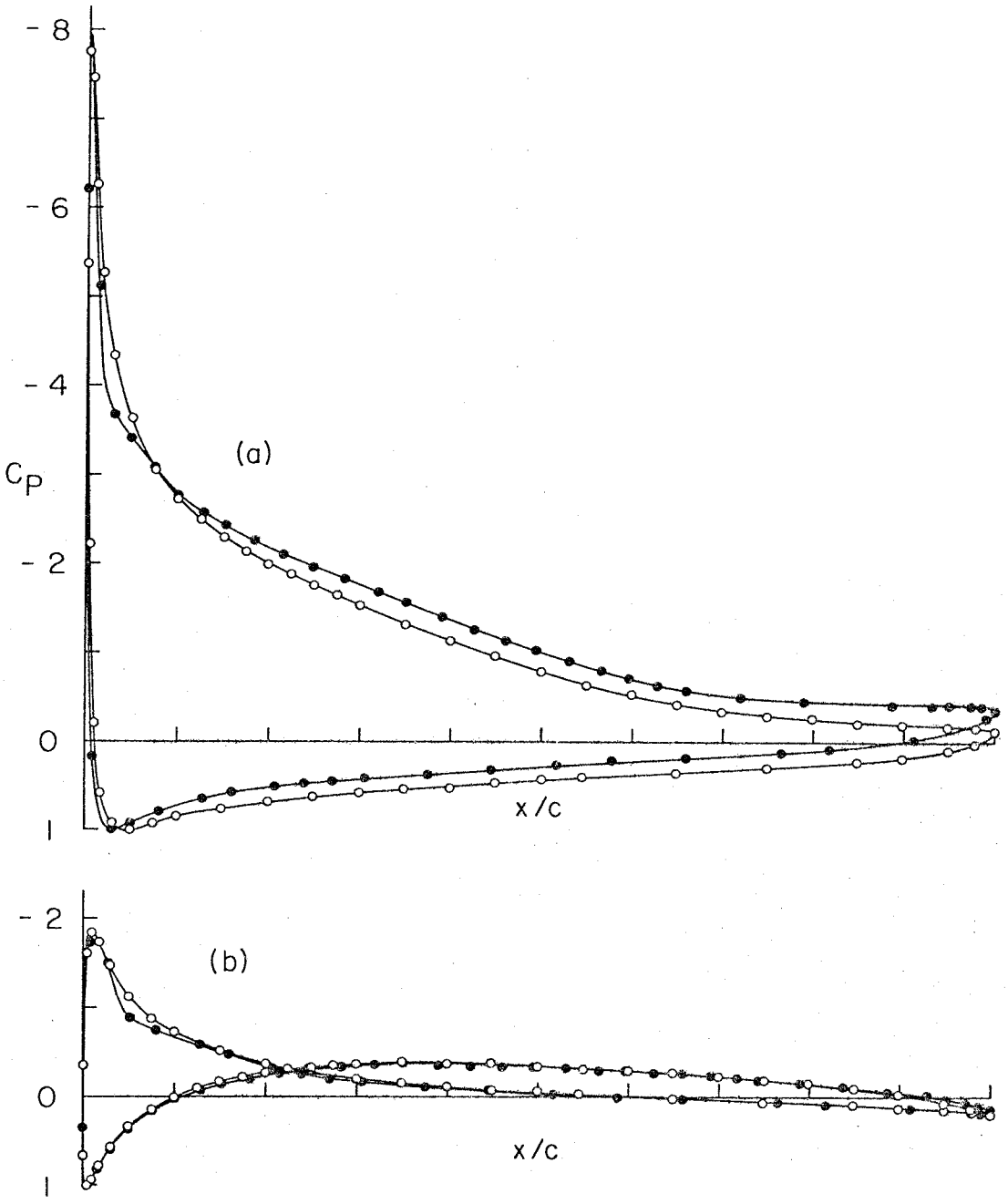


Figure 21. Measured surface-pressure distributions at mid-span. Solid symbols: present data, Table 2, Runs 87 and 38. Open symbols: data from Pinkerton (1938), Table Ig, $\alpha = 18°$ and $-4°$.

(a) Maximum lift: $C_L \sim 1.68$.
(b) Zero lift.

when three-dimensional effects and boundary-layer separation are involved. One practice is to measure $Q_\infty$ (with the model absent) and $Q_{ref}$ (with the model present) at the same flow rate, as indicated by the same pressure difference for two upstream piezometer rings. This practice is not applicable for a compound test section. During Runs 35-40 of the present experiments, for example, Table 2 shows that the dynamic pressure at the roof-mounted pitot-static tube decreased by about 15 percent as the airfoil was pitched from zero lift to maximum lift. Presumably a larger fraction of the air flow was diverted outside the false walls at higher angles of incidence.

We expected that Pinkerton's data at maximum lift in Figure 21a would show less blockage effect than our data, because of his relatively larger test section. However, the figure makes a discussion of blockage in normal terms ($Q_{ref}/Q_\infty$ = constant > 1) almost pointless. There is no factor $Q_{ref}/Q_\infty$ which will bring the measurements into coincidence. For the data near the trailing edge, the evidence even suggests that $Q_{ref}/Q_\infty$ was larger for Pinkerton's data than for ours. In these mysterious circumstances, we simply report our data as measured, without adjustment for tunnel blockage. Note also in Figures 21a and 21b that there is a local discrepancy in pressure coefficient near the nose, in the region $0.02 < x/c < 0.10$, for both airfoil surfaces. This discrepancy is not caused by the presence of a tripping device. It is probably caused by local flat spots in our airfoil contour resulting from a small

gap between the skin and ribs of the airfoil mold in this region of large and rapidly changing surface curvature.

To the extent that the present data will eventually be used in the development of numerical calculation methods, it may even be an advantage to bound the region of calculation by including the tunnel walls. We have been careful in Section 2 to give all the information required for this purpose, subject to two additional minor caveats. The test section of the GALCIT tunnel is relatively short, and the flow in the empty tunnel may behave a little like flow in a weakly convergent-divergent nozzle. It is also known that the total pressure was not quite constant over the tunnel cross-section under the conditions of the main hot-wire measurements, being lower (by about 0.007 $Q_{ref}$) near the center line than at the reference point near the roof (see the footnote under "Static and Total Pressure" in the next Section 3.3).

3.3 The Boundary Layer and Wake

Static and Total Pressure. -- In support of the main hot-wire measurements at $\alpha$ = 14 degrees, a few measurements were made of static pressure and total pressure outside the boundary layer and wake. A conventional pitot-static tube was installed on one arm of the rotor, which was then clamped at a suitable angle and traversed to the desired position. Total and static pressure were both referred to atmospheric pressure and were measured separately, using the same electronic differential manometer. The averaging time was about one minute. The

location of the data points (i.e., the location in airfoil coordinates of the static orifice of the probe) and the results obtained are given in Figure 22 and in Table 3. At the time of these measurements, the boundary of the turbulent region was known approximately from Kiel-probe surveys mentioned below. Later

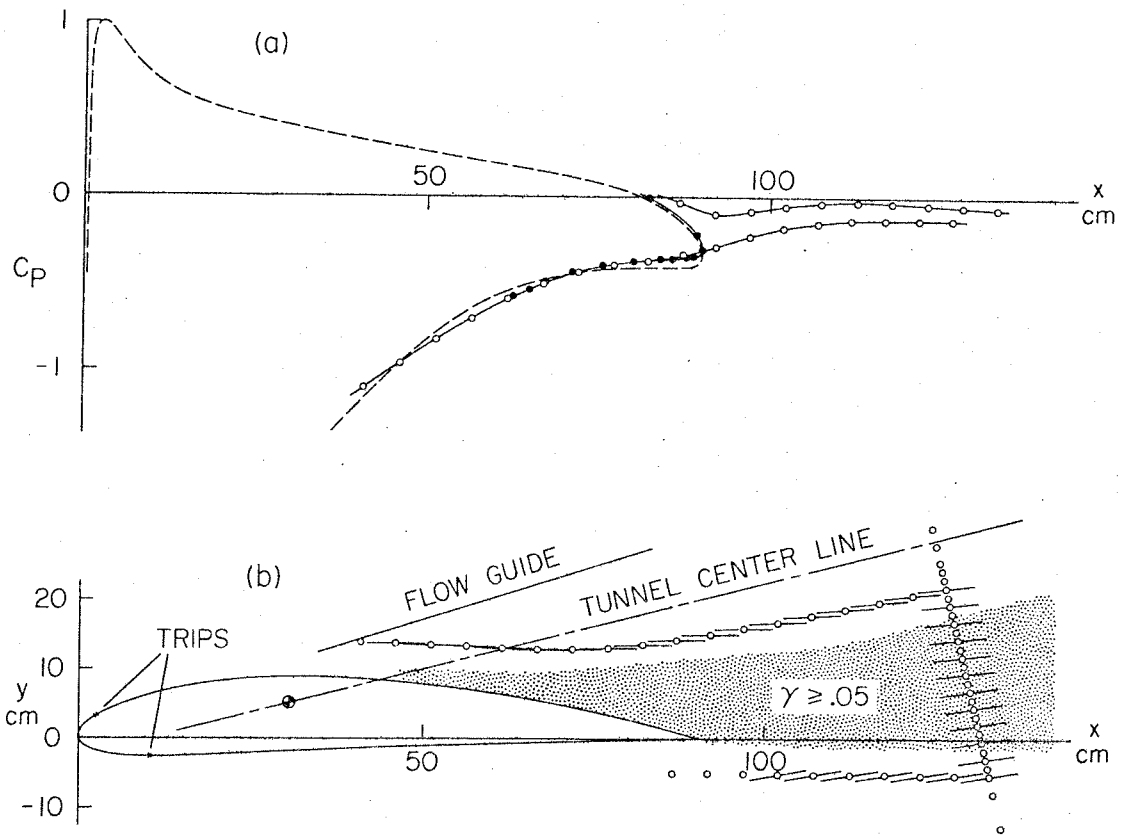


Figure 22. Measured static pressure for pitot-static-tube traverse in stream direction above and below airfoil, including location of data points.

(a) Open symbols: pressure coefficients from pitot-static tube. Dashed line: interference-free surface pressure distribution from Run 87. Solid symbols: surface pressure from Run 87 after correction (from Table 10) for effect of rotor hub at position listed in Table 3.

(b) Location of pitot-static probe with respect to airfoil.

Table 3

## PITOT-STATIC MEASUREMENTS

| Code | Traverse position X (cm) | x (cm) | y (cm) | Pitot-static probe angle (deg) | $\frac{p_t - p_{atm}}{Q_{ref}}$ | $\frac{q}{q_{ref}}$ | $C_p$ | Hot-wire flow angle (deg) | Angle error (deg) | $\frac{q_{h-w}}{q_{p-s}}$ |
|---|---|---|---|---|---|---|---|---|---|---|
| | | | | Suction side | | | | | | |
| H | 30.0 | 40.77 | 13.81 | -3.1 | 1.077 | 1.449 | -1.102 | 0.3 | -3.4 | (0.999) |
| I | 35.0 | 45.97 | 13.62 | -3.1 | 1.074 | 1.397 | -0.957 | -0.7 | -2.4 | (0.996) |
| J | 40.0 | 51.17 | 13.42 | -3.1 | 1.073 | 1.347 | -0.821 | -1.4 | -1.7 | (0.998) |
| K | 45.0 | 56.38 | 13.19 | -3.1 | 1.073 | 1.301 | -0.699 | -1.9 | -1.2 | (0.997) |
| L | 50.0 | 61.59 | 12.93 | -3.1 | 1.071 | 1.257 | -0.588 | -1.8 | -1.3 | (0.998) |
| F | 51.4 | 66.80 | 12.68 | -0.1 | 1.068 | 1.220 | -0.500 | -1.4 | 1.3 | (1.002) |
| G | 56.4 | 71.93 | 12.79 | -0.1 | 1.072 | 1.193 | -0.432 | -0.8 | 0.7 | (1.003) |
| P | 57.6 | 77.06 | 12.86 | 2.9 | 1.065 | 1.174 | -0.393 | -0.4 | 3.3 | 1.008 |
| S | 58.7 | 82.07 | 13.41 | 5.9 | 1.054 | 1.159 | -0.370 | 0 | 5.9 | 1.005 |
| T | 63.7 | 87.06 | 14.06 | 5.9 | 1.055 | 1.141 | -0.326 | 0.1 | 5.8 | 1.010 |
| W | 67.6 | 92.02 | 14.85 | 6.9 | 1.054 | 1.122 | -0.284 | 0.1 | 6.8 | 1.008 |
| X | 72.6 | 96.94 | 15.76 | 6.9 | 1.056 | 1.096 | -0.225 | 0.5 | 6.4 | 1.008 |
| Y | 77.6 | 101.88 | 16.63 | 6.9 | 1.062 | 1.077 | -0.177 | 1.3 | 5.6 | 1.002 |
| U | 81.2 | 106.80 | 17.55 | 7.9 | 1.061 | 1.062 | -0.146 | 2.5 | 5.4 | 1.003 |
| V | 86.2 | 111.72 | 18.50 | 7.9 | 1.066 | 1.057 | -0.130 | 3.6 | 4.3 | 0.997 |
| Z1 | 89.9 | 116.63 | 19.47 | 8.9 | 1.066 | 1.056 | -0.129 | 4.7 | 4.2 | 0.986 |
| Z2 | 94.9 | 121.51 | 20.54 | 8.9 | 1.067 | 1.055 | -0.127 | 5.4 | 3.5 | (0.998) |
| Z3 | 99.9 | 126.40 | 21.62 | 8.9 | 1.068 | 1.057 | -0.129 | 6.0 | 2.9 | (0.997) |

Table 3 (continued)

Pressure side

| | | | | | | | | | | |
|---|---|---|---|---|---|---|---|---|---|---|
| A | 66.4 | 86.63 | -5.06 | -0.1 | 1.073 | 1.012 | -0.030 | | | |
| B | 71.4 | 91.80 | -5.12 | -0.1 | 1.072 | 1.044 | -0.097 | | | |
| C | 76.4 | 96.96 | -5.15 | -0.1 | 1.073 | 1.036 | -0.080 | | | |
| D | 81.4 | 102.11 | -5.19 | -0.1 | 1.073 | 1.020 | -0.048 | 9.3 | -9.4 | 1.007 |
| E | 86.4 | 107.29 | -5.27 | -0.1 | 1.071 | 1.011 | -0.031 | 9.1 | -9.2 | 1.005 |
| M | 87.6 | 112.45 | -5.34 | 2.9 | 1.070 | 1.007 | -0.024 | 8.7 | -5.8 | 1.007 |
| N | 92.6 | 117.60 | -5.33 | 2.9 | 1.071 | 1.011 | -0.031 | 8.5 | -5.6 | 1.005 |
| O | 97.6 | 122.76 | -5.37 | 2.9 | 1.072 | 1.016 | -0.041 | 8.4 | -5.5 | 1.006 |
| Q | 98.7 | 127.91 | -5.36 | 5.9 | 1.070 | 1.022 | -0.053 | 8.5 | -2.6 | (1.004) |
| R | 103.7 | 133.05 | -5.32 | 5.9 | 1.075 | 1.028 | -0.062 | 8.5 | -2.6 | (0.999) |

Table 3 (concluded)

Wake traverse

| | | | | | | | | | | |
|---|---|---|---|---|---|---|---|---|---|---|
| 23.5 | 101.2 | 134.93 | -12.94 | 7.9 | | | -0.055 | | | |
| 21.5 | 101.2 | 133.71 | - 8.01 | 7.9 | 1.073 | 1.025 | -0.058 | 8.6 | -0.7 | (1.001) |
| 20.5 | 101.2 | 133.10 | - 5.54 | 7.9 | 1.072 | 1.026 | -0.061 | 8.6 | -0.7 | (1.001) |
| 20.0 | 101.2 | 132.80 | - 4.31 | 7.9 | 1.072 | 1.027 | -0.062 | 8.4 | -0.5 | (1.000) |
| 19.5 | 101.2 | 132.49 | - 3.08 | 7.9 | 1.074 | 1.029 | -0.063 | 8.3 | -0.4 | (0.998) |
| 19.0 | 101.2 | 132.19 | - 1.85 | 7.9 | 1.071 | 1.029 | -0.067 | 8.3 | -0.4 | 1.000 |
| 18.5 | 101.2 | 131.89 | - .61 | 7.9 | 1.063 | 1.028 | -0.074 | 8.3 | -0.4 | 0.997 |
| 18.0 | 101.2 | 131.58 | .62 | 7.9 | 1.027 | 1.017 | -0.086 | 8.4 | -0.5 | 0.996 |
| 17.5 | 101.2 | 131.28 | 1.85 | 7.9 | | 0.995 | -0.103 | 8.4 | -0.5 | 0.992 |
| 17.0 | 101.2 | 130.97 | 3.09 | 7.9 | | 0.957 | -0.121 | 8.8 | -0.9 | 0.985 |
| 16.5 | 101.2 | 130.67 | 4.32 | 7.9 | | 0.902 | -0.132 | 8.7 | -0.8 | 0.993 |
| 16.0 | 101.2 | 130.36 | 5.55 | 7.9 | | 0.859 | -0.138 | 8.4 | -0.5 | 0.986 |
| 15.5 | 101.2 | 130.06 | 6.79 | 7.9 | | 0.842 | -0.138 | 8.0 | -0.1 | 0.994 |
| 15.0 | 101.2 | 129.75 | 8.02 | 7.9 | | 0.850 | -0.137 | 7.4 | 0.5 | 0.982 |
| 14.5 | 101.2 | 129.45 | 9.25 | 7.9 | | 0.882 | -0.133 | 6.9 | 1.0 | 0.985 |
| 14.0 | 101.2 | 129.15 | 10.49 | 7.9 | | 0.929 | -0.129 | 6.7 | 1.2 | 0.967 |
| 13.5 | 101.2 | 128.84 | 11.72 | 7.9 | | 0.962 | -0.123 | 6.2 | 1.7 | 0.989 |
| 13.0 | 101.2 | 128.54 | 12.95 | 7.9 | | 1.001 ? | -0.116 | 6.3 | 1.6 | 0.974 |
| 12.5 | 101.2 | 128.23 | 14.18 | 7.9 | | 1.013 | -0.113 | 6.2 | 1.7 | 0.994 |
| 12.0 | 101.2 | 127.93 | 15.42 | 7.9 | 1.023 | 1.026 | -0.110 | 6.3 | 1.6 | 0.995 |
| 11.5 | 101.2 | 127.62 | 16.65 | 7.9 | 1.044 | 1.036 | -0.109 | 6.1 | 1.8 | 1.001 |
| 11.0 | 101.2 | 127.32 | 17.88 | 7.9 | 1.059 | 1.044 | -0.111 | 6.1 | 1.8 | 0.995 |
| 10.5 | 101.2 | 127.01 | 19.12 | 7.9 | 1.068 | 1.051 | -0.115 | 6.1 | 1.8 | 0.990 |
| 10.0 | 101.2 | 126.71 | 20.35 | 7.9 | 1.071 | 1.054 | -0.119 | 6.1 | 1.8 | 0.996 |
| 9.0 | 101.2 | 126.10 | 22.81 | 7.9 | 1.074 | 1.060 | -0.129 | 6.0 | 1.9 | (0.998) |
| 8.0 | 101.2 | 125.49 | 25.28 | 7.9 | 1.073 | 1.065 | -0.141 | | | |
| 7.0 | 101.2 | 124.88 | 27.75 | 7.9 | | | -0.152 | | | |
| 6.0 | 101.2 | 124.27 | 30.21 | 7.9 | | | -0.162 | | | |
| 5.0 | 101.2 | 123.67 | 32.68 | 7.9 | | | -0.173 | | | |
| 4.0 | 101.2 | 123.06 | 35.14 | 7.9 | | | -0.183 | | | |
| 3.0 | 101.2 | 122.45 | 37.61 | 7.9 | | | -0.192 | | | |

and more accurate hot-wire observations showed the turbulent region, defined (say) by the value $\langle\gamma\rangle \geq 0.05$, to lie as shown by the shaded area in Figure 22b. The pitot-static traverse above the airfoil may have trespassed slightly on this turbulent region near the trailing edge, although an equally plausible explanation for the low total pressure in this region* (see the column "$(p_t - p_{atm}) / Q_{ref}$" in Table 3) may be probe misalignment. The mean flow direction at the various measurement points was not known even approximately, and therefore had to be guessed. A later comparison with flow directions derived from the flying-hot-wire data (these directions are indicated by the short line segments through the data points in Figure 22b; see also the column "Angle error" in Table 3) showed that the guess was correct to within a few degrees except above and below the airfoil near the trailing edge.

The dashed line in Figure 22a represents the pressure measured on the airfoil surface during Run 87, with the rotor far downstream. It is known that these pressures were noticeably perturbed when the rotor and hub were moved to a more upstream location, as was automatically the case for the pitot-static measurements. Thus the difference between the dashed line and the open points in Figure 22a should be taken as a

---

* Note in Table 3 that the total pressure, expressed as $(p_t - p_{atm})/Q_{ref}$, is about 1.073 on both sides of the wake. For the roof-mounted pitot-static tube, the same quantity was measured as 1.080. Hence the total pressure was not quite constant across the test section.

measure of rotor interference, not as a measure of pressure gradient normal to the airfoil surface. A further discussion of this question appears under "Observed Effects" in Section 5.1 below, where the solid points in Figure 22a are explained.

Part of Table 3 represents a vertical traverse through the wake with the pitot-static probe inclined at 6 degrees to the tunnel axis (7.9 degrees to the airfoil chord line). The purpose of these measurements was to establish, by direct comparison with the flying-hot-wire data, the errors likely to be associated with use of such conventional instrumentation in regions of moderate turbulence level. The comparison in terms of mean velocity is made in Figure 23 and shows fair agreement; but note that the static pressure was measured and not simply assumed to be constant. Also shown in the figure are the measured mean static pressure and the measured value (from the hot-wire data) of $\langle v'v' \rangle / (q_{ref})^2$, a quantity which is sometimes added to the mean static pressure to obtain an approximate integral of the boundary-layer equation normal to the general flow direction. The data cannot be said to support the notion of an approximate integral. However, the coordinates are not properly oriented, and the usual boundary-layer approximation is not quite appropriate for the present flow, which is sufficiently curved so that there are substantial gradients in velocity and static pressure outside the wake.

Boundary-layer Profiles. -- Figure 24 is a photograph of a 7-tube boundary layer rake attached by a suction cup to the

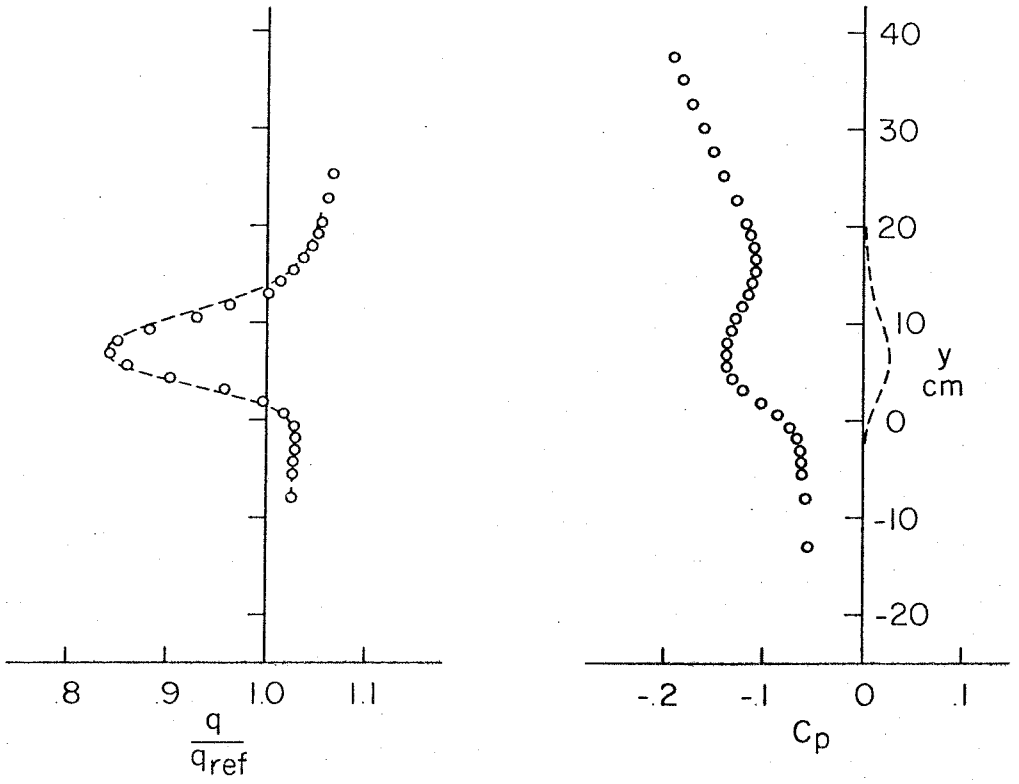


Figure 23. Velocity and static pressure from pitot-static-tube traverse across wake. Dashed lines are flying-hot-wire data; $q/q_{ref}$ at left and $\langle v'v' \rangle / (q_{ref})^2$ at right.

suction surface of the airfoil near the trailing edge. Total pressures from this rake were read on an alcohol manometer bank. The static pressure for each profile was taken as the surface value from Run 87. The mean-velocity profiles obtained are listed in Table 4, for what they are worth (the first point of each profile, for example, can be treated as a Preston-tube point for a tube 0.081 cm in outside diameter). With one exception, however, they are not plotted. These profiles are traverses along lines roughly normal to the airfoil surface; the distance from the surface is denoted by $y_n$ in the table. The

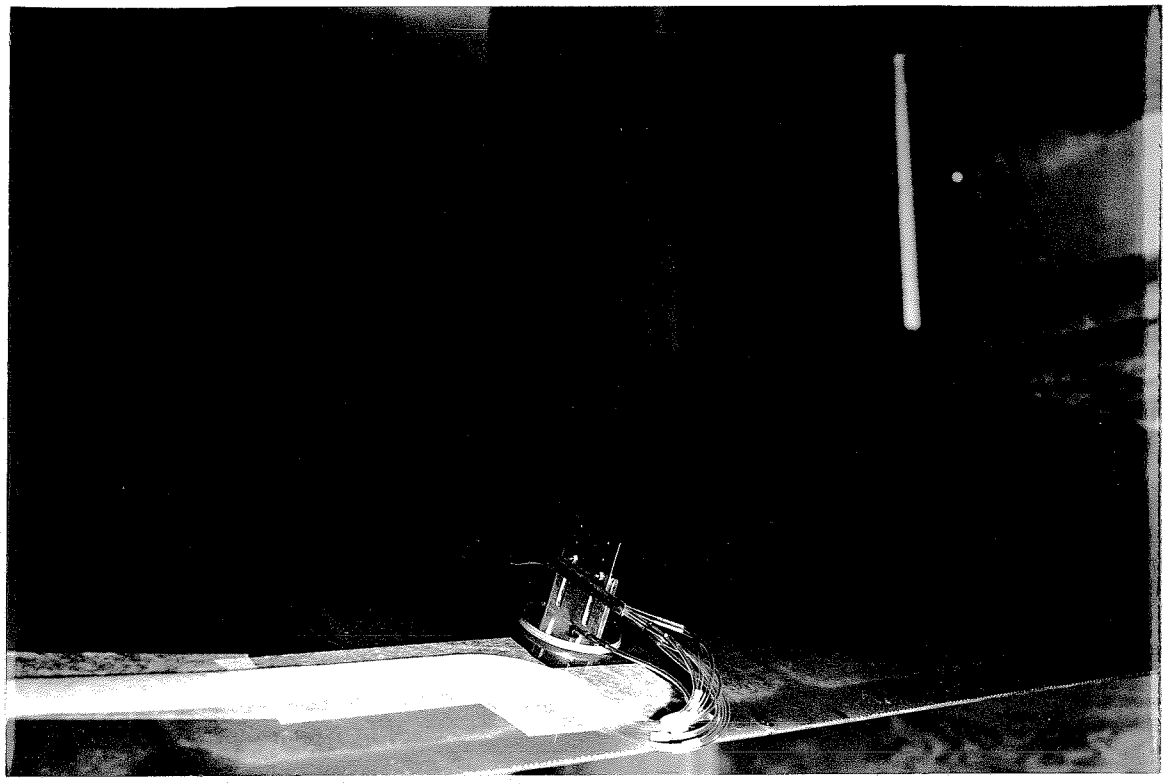

Figure 24. Installation of boundary-layer rake near trailing edge of airfoil.

profiles should not be compared directly to the hot-wire data, because they were obtained with the rotor far downstream, and they are also subject to unknown interference from the rake device itself. They may provide a check on any calculation of boundary-layer development upstream of separation in the interference-free flow defined by the pressure distribution of Run 87.

The most important result obtained from the rake was a single boundary-layer profile on the pressure surface of the airfoil, at $x/c = 0.820$. The data, shown in logarithmic

Table 4

## BOUNDARY-LAYER (RAKE) PROFILES

### Suction Surface

| $\frac{x}{c}$ = 0.372 | | 0.455 | | 0.536 | | 0.620 | | 0.705 | | 0.789 | |
|---|---|---|---|---|---|---|---|---|---|---|---|
| $y_n$ (cm) | $\frac{q}{q_{ref}}$ | $y_n$ (cm) | $\frac{q}{q_{ref}}$ | $y_n$ (cm) | $\frac{q}{q_{ref}}$ | $y_n$ (cm) | $\frac{q}{q_{ref}}$ | $y_n$ (cm) | $\frac{q}{q_{ref}}$ | $y_n$ (cm) | $\frac{q}{q_{ref}}$ |
| 0.041 | 0.731 | 0.041 | 0.596 | 0.041 | 0.451 | 0.041 | 0.274 | 0.041 | 0.118 | 0.041 | 0.118 |
| 0.295 | 1.045 | 0.295 | 0.838 | 0.295 | 0.647 | 0.295 | 0.444 | 0.295 | 0.241 | 0.295 | 0.145 |
| 0.549 | 1.266 | 0.549 | 1.018 | 0.549 | 0.785 | 0.549 | 0.551 | 0.549 | 0.307 | 0.549 | 0.152 |
| 0.803 | 1.463 | 0.699 | 1.140 | 0.803 | 0.957 | 0.803 | 0.688 | 0.803 | 0.415 | 0.803 | 0.224 |
| 1.057 | 1.556 | 0.803 | 1.209 | 1.057 | 1.104 | 1.057 | 0.817 | 1.057 | 0.520 | 1.057 | 0.281 |
| 1.311 | 1.571 | 0.953 | 1.323 | 1.207 | 1.199 | 1.219 | 0.914 | 1.232 | 0.596 | 1.311 | 0.361 |
| 1.565 | 1.571 | 1.057 | 1.359 | 1.311 | 1.238 | 1.311 | 0.951 | 1.311 | 0.616 | 1.435 | 0.387 |
| | | 1.207 | 1.425 | 1.461 | 1.315 | 1.473 | 1.051 | 1.486 | 0.729 | 1.565 | 0.412 |
| | | 1.311 | 1.445 | 1.565 | 1.326 | 1.565 | 1.066 | 1.565 | 0.726 | 1.689 | 0.471 |
| | | 1.461 | 1.463 | 1.715 | 1.355 | 1.727 | 1.147 | 1.740 | 0.833 | 1.943 | 0.535 |
| | | 1.565 | 1.464 | 1.969 | 1.367 | 1.981 | 1.230 | 1.994 | 0.923 | 2.197 | 0.633 |
| | | 1.715 | 1.468 | 2.223 | 1.369 | 2.235 | 1.263 | 2.248 | 1.013 | 2.451 | 0.722 |
| | | 1.969 | 1.469 | 2.477 | 1.370 | 2.489 | 1.277 | 2.502 | 1.100 | 2.705 | 0.801 |
| | | 2.223 | 1.466 | 2.731 | 1.368 | 2.743 | 1.279 | 2.731 | 1.154 | 2.819 | 0.823 |
| | | | | | | | | 2.756 | 1.154 | 2.959 | 0.865 |
| | | | | | | | | 2.985 | 1.192 | 3.073 | 0.907 |
| | | | | | | | | 3.239 | 1.213 | 3.327 | 0.973 |
| | | | | | | | | 3.493 | 1.220 | 3.581 | 1.061 |
| | | | | | | | | 3.747 | 1.222 | 3.835 | 1.105 |
| | | | | | | | | 4.001 | 1.228 | 4.089 | 1.138 |
| | | | | | | | | 4.255 | 1.226 | 4.166 | 1.144 |
| | | | | | | | | | | 4.343 | 1.166 |
| | | | | | | | | | | 4.420 | 1.170 |
| | | | | | | | | | | 4.674 | 1.182 |
| | | | | | | | | | | 4.928 | 1.189 |
| | | | | | | | | | | 5.182 | 1.192 |
| | | | | | | | | | | 5.436 | 1.196 |
| | | | | | | | | | | 5.690 | 1.194 |

### Pressure Surface

| $\frac{x}{c}$ = 0.820 | |
|---|---|
| $y_n$ (cm) | $\frac{q}{q_{ref}}$ |
| 0.041 | 0.652 |
| 0.295 | 0.866 |
| 0.549 | 0.923 |
| 0.803 | 0.946 |
| 1.057 | 0.951 |
| 1.311 | 0.954 |
| 1.565 | 0.951 |

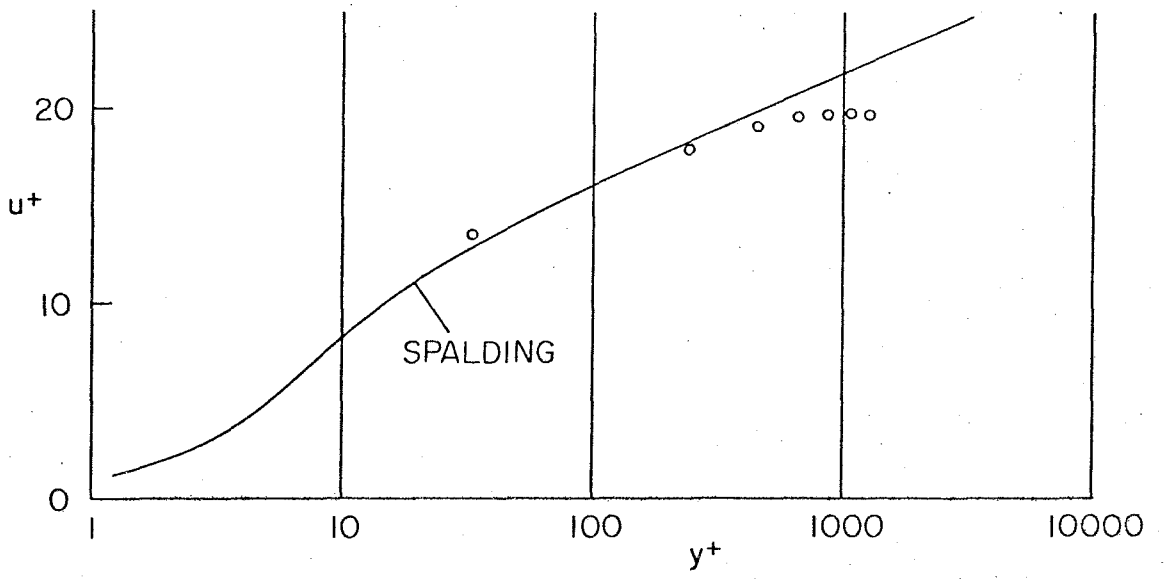


Figure 25. Boundary-layer profile on pressure surface, at x/c = 0.820, in law-of-the-wall coordinates ( $\kappa$ = 0.41, c = 5.0).

coordinates in Figure 25, provide the only available information about the development of the boundary layer on the pressure surface. The profile is clearly turbulent, with a Reynolds number based on momentum thickness and $q_{ref}$ of about 1090. A difficult fit to Spalding's formula (1961) for the law of the wall, with $\kappa$ = 0.41 and c = 5.0, yields a rough value of 0.0047 for a local friction coefficient based on $q_{ref}$. The parameter $(\delta^*/\tau_w)dp/dx$, with dp/dx taken from the pressure data of Run 87, is estimated to be about -0.152.

At one stage of the experiment, considerable time was spent in recording data from a small Kiel probe (a shrouded total-pressure probe alleged to be quite insensitive to flow angle). Figure 13 shows this probe installed in one end of the rotor arm,

which is clamped in the vertical position. Traverses were made through the boundary layer and wake at some 17 stations. The measurements were not originally intended to be so elaborate; they were in fact busy work, carried out to fill a gap of two or three days while the analog-to-digital converter was recovering from a cracked transistor. The data have for practical purposes been discarded, because the Kiel probe did not approach the surface very closely, because the static pressure was very uncertain, and because the rotor hub was further forward than normal.

## IV. FLYING-HOT-WIRE MEASUREMENTS

### 4.1 Geometry

During the experiment, all measurements of probe position were referred to a coordinate system (X, Y) defined by the traverse mechanism, whose motion was accurately aligned with the tunnel axis. However, this coordinate system is an awkward one for presenting the processed hot-wire data to potential users. Mostly for the sake of convenience in describing the airfoil surface, the processed data are eventually offered at points on a rectangular grid (x, y) defined by the chord line of the airfoil, as shown in Figure 26. For the hot-wire data to be fully useful, the position of the probe relative to the airfoil must be known to within a fraction of a millimeter under actual test conditions, with the tunnel running and the probe flying. The necessary measurements were complicated by the fact that the probe and

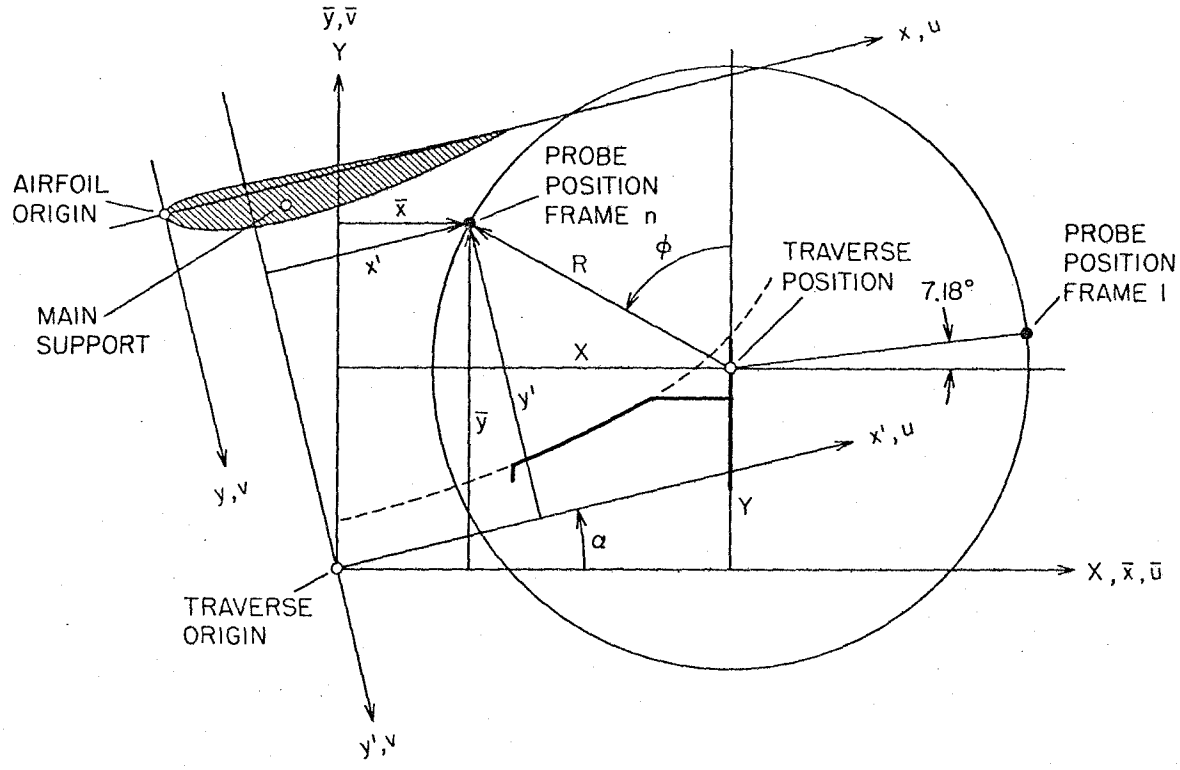


Figure 26. Coordinate systems used for data analysis and presentation:

- (X, Y) define position of rotor hub; i.e., displacement of traverse system from its origin, with Y increasing vertically upward.
- $(\bar{x}, \bar{y})$ give probe position in same system; corresponding velocity components are $(\bar{u}, \bar{v})$
- (x', y') have same origin as $(\bar{x},\bar{y})$ but are aligned with airfoil chord line; corresponding velocity components are $(\bar{u}, \bar{v})$. Sense of y' and v is opposite to sense of $\bar{y}$ and $\bar{v}$.
- (x, y) are like (x', y') but with origin translated to upstream end of chord line.

Dashed line is collision limit for traverse position. Heavy line is traverse trajectory during main experiments and shows boundary-layer traverse, grazing traverse, horizontal traverse, and vertical traverse.

the airfoil were attached to the building at points several meters apart (cf. Figure 5).

Probe Radius. -- The radial distance along the rotor arm from the rotor axis to the probe body axis was 75.25 cm. The probe offset (the tangential distance from the neutral axis of the rotor arm to the center of the X-array; see Figure 6) was 7.43 cm. The probe offset angle was therefore 5.64 degrees, as illustrated for another purpose in Figure 31 below. If the probe and arm were at right angles, the radius R to the center of the X-array would be 75.62 cm. To measure this distance R directly, a cathetometer was improvised by mounting a transit telescope on the vertical traverse mechanism. Measured radii R for the six available probes are listed in Table 5. The consistent difference in R of about 0.08 cm for the same probe on different arms means that the probe holder and the arm were not quite at right angles. The larger difference in R of up to

Table 5

PROBE RADIUS

| | R to center of X (cm) | | R to outside of X (cm) | |
|---|---|---|---|---|
| Probe | on arm 1 | on arm 2 | on arm 1 | on arm 2 |
| 1 | 75.761 | 75.684 | 75.816 | 75.738 |
| 2 | 75.748 | 75.667 | 75.799 | 75.717 |
| 3 | 75.651 | 75.573 | 75.702 | 75.626 |
| 4 | 75.644 | 75.560 | 75.689 | 75.608 |
| 5 | 75.580 | 75.507 | 75.636 | 75.562 |
| 6 | 75.669 | 75.593 | 75.725 | 75.649 |

0.18 cm for different probes on the same arm (cf. probes 1 and 5) was caused by lack of concentricity between the probe stem and the metal sleeve used for registration (see Figure 6).

Model Position (air off). -- With the tunnel off, the position of the airfoil with respect to the traverse system was measured by a combination of methods. The traverse was set at several uniformly spaced streamwise positions and then moved vertically until the outer needle of one probe (probe 6 on arm 2) cleared the model by about 0.005 to 0.010 cm, as judged by viewing the probe together with its reflection in the model surface while moving the rotor by hand. This process defined the rear portion of the airfoil surface as the envelope of a number of circular arcs of known center and radius. The measurements were verified and smoothed with the aid of a small dial indicator clamped to one arm of the rotor. The value of the constant radius corresponding to zero indicator reading at closest approach was inferred by comparison with the previous results. This radius, once known, also allowed the streamwise location of the trailing-edge corner to be determined to an accuracy of about 0.02 cm.

The result of these measurements is recorded in Table 6. The variables X and Y denote various positions of the rotor hub such that a circle of radius 75.656 cm was just in contact with the airfoil surface. The actual points of contact are denoted by $\bar{x}_m$, $\bar{y}_m$, (air off). They were found by iterating on successive values for local surface slope, as defined by adjacent contact

Table 6

## MODEL POSITION IN TEST SECTION

| Traverse | | Air off | | Air on | | Air on | | Air on | | |
|---|---|---|---|---|---|---|---|---|---|---|
| X | Y | $\bar{x}_m$ | $\bar{y}_m$ | $\bar{x}_m$ | $\bar{y}_m$ | $x'_m$ | $y'_m$ | $x_m$ | $y_m$ | $y-c\eta_s$ |
| (cm) | (in.) | (cm) | (cm) | (cm) | (cm) | (cm) | (cm) | (cm) | (cm) | (cm) |
| 5 | 5.434 | -12.441 | 87.422 | -12.404 | 87.272 | 8.879 | -87.701 | 29.743 | 8.888 | .002 |
| 10 | 5.920 | - 9.058 | 88.252 | - 9.021 | 88.102 | 12.362 | -87.696 | 33.226 | 8.893 | -.009 |
| 15 | 6.460 | - 5.738 | 89.167 | - 5.701 | 89.017 | 15.804 | -87.788 | 36.668 | 8.801 | -.010 |
| 20 | 7.043 | - 2.372 | 90.162 | - 2.335 | 90.012 | 19.310 | -87.948 | 40.174 | 8.641 | .006 |
| 25 | 7.676 | 1.120 | 91.285 | 1.157 | 91.135 | 22.970 | -88.200 | 43.834 | 8.389 | .006 |
| 30 | 8.350 | 4.933 | 92.591 | 4.970 | 92.441 | 26.985 | -88.554 | 47.849 | 8.035 | .005 |
| 35 | 9.062 | 8.606 | 93.919 | 8.643 | 93.769 | 30.869 | -88.963 | 51.733 | 7.626 | .009 |
| 40 | 9.819 | 12.248 | 95.324 | 12.285 | 95.174 | 34.742 | -89.454 | 55.606 | 7.135 | -.003 |
| 45 | 10.611 | 16.160 | 96.896 | 16.197 | 96.746 | 38.916 | -90.042 | 59.780 | 6.547 | -.004 |
| 50 | 11.440 | 20.064 | 98.539 | 20.101 | 98.389 | 43.100 | -90.702 | 63.964 | 5.887 | -.002 |
| 55 | 12.307 | 24.013 | 100.279 | 24.050 | 100.129 | 47.352 | -91.444 | 68.216 | 5.145 | .002 |
| 60 | 13.209 | 27.836 | 102.029 | 27.873 | 101.879 | 51.483 | -92.227 | 72.347 | 4.362 | .013 |
| 65 | 14.157 | 31.552 | 103.820 | 31.589 | 103.670 | 55.520 | -93.075 | 76.384 | 3.514 | .009 |
| 70 | 15.149 | 35.418 | 105.768 | 35.455 | 105.618 | 59.740 | -94.039 | 80.604 | 2.550 | -.001 |
| 75 | 16.182 | 39.401 | 107.859 | 39.438 | 107.709 | 64.108 | -95.114 | 84.972 | 1.475 | -.009 |
| 80 | 17.252 | 43.391 | 110.030 | 43.428 | 109.880 | 68.502 | -96.266 | 89.366 | 0.323 | -.002 |
| Trailing edge | | 44.087 | 110.419 | 44.124 | 110.269 | 69.271 | -96.476 | 90.135 | 0.113 | 0 |

points, until the local normal passed through the rotor axis.

All of the measurements just described were made with a man standing on the floor of the test section. The deflection of the tunnel (and the model) with respect to the traverse system under these conditions was measured as no more than 0.003 cm. This deflection has been neglected in the calculations.

Model Position (air on). -- The deflection of the airfoil model under air load was measured with the aid of a small optical proximity sensor mounted on one arm of the rotor. The sensor is the black trapezoid-shaped object at the tip of the arm in Figure 6. It consists of a light-emitting diode and a photo-transistor which illuminate and view along lines intersecting a few millimeters from the face of the detector. To obtain a strong sensor signal, a strip of gold-coated reflective tape, 0.9 cm wide and 0.007 cm thick, was attached to the wing surface in the plane of rotation of the rotor, some 11 cm to one side of the midspan pressure orifices (this tape is conspicuous in Figure 12). The reflective tape extended from $x/c = 0.18$ to the trailing edge and remained in place throughout the experiments. The sensor output was fed to a peak-detector circuit which was reset by the INDEX pulse. With the tunnel off and the rotor rotating at standard speed (6.25 rev/sec), the mean peak sensor voltage was recorded as a function of vertical traverse position, with the result shown in Figure 27. The same procedure was then repeated with the tunnel on at standard speed ($Q_{nom} = 10$ lbf/ft$^2$). Note that the relative displace-

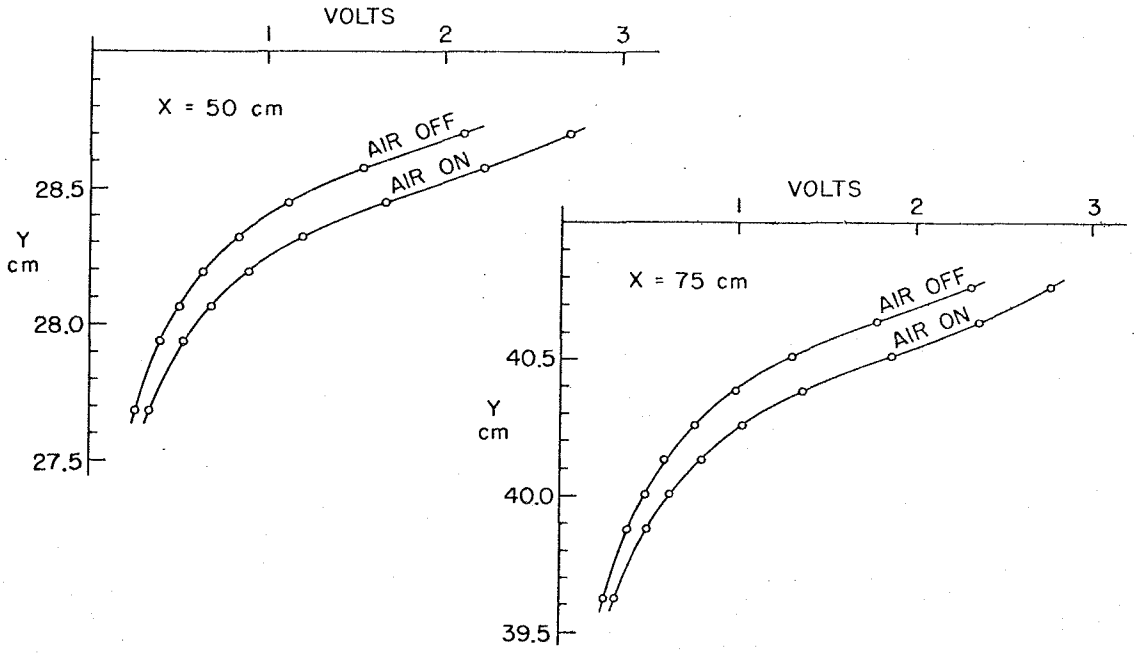


Figure 27. Output of optical proximity sensor during vertical traverse toward airfoil at two fixed values of X. Rotor is rotating at standard speed (375 rpm). When tunnel is turned on, downward displacement of airfoil is 0.152 cm at X = 50 cm and 0.147 cm at X = 75cm.

ment is defined operationally and need not be resolved into a part due to airfoil deflection and a part due to strut deflection. The measurements were made at two streamwise traverse positions, X = 50 cm and X = 75 cm. The observed vertical displacements as scaled from the figure were 0.152 cm and 0.147 cm respectively. After a little algebra, these became 0.142 cm and 0.134 cm normal to the chord line. This motion was conveniently resolved into a plane deflection of 0.155 cm normal to the chord and a rotation of 0.022 degrees (increase in angle of incidence) about the main spar. The measured deflection of 0.155 cm normal to the chord, incidentally, was consistent with

the estimated normal force on the wing and the spring rate observed during the static proof test described under "Fabrication" in Section 2.2 above.

Repeatability. -- As wires failed and were replaced during the various hot-wire measurements, the nominal angle of incidence of the model was frequently changed between 14 degrees (for data) and -4 degrees (for wire calibration; see Section 4.2 below). During this process, occasional checks were made of model position, using the grazing-probe method. The airfoil adjustment was quite stiff, mainly because of friction on the end seals, and the various measurements showed that the angle of incidence (viewed as a rotation about the main spar) was not repeatable to better than about $\pm$ 0.03 degrees. The particular air-off setting during the main measurements was relatively uncertain, and differed from the setting for the air-off data in Table 6 by about 0.029 degrees (decrease in angle of incidence). Because of the uncertainty, this angle has been taken for simplicity to be equal and opposite to the observed torsional deflection of 0.022 degrees from the air-off to the air-on condition. The model displacement under aerodynamic load has therefore been approximated as a simple translation of 0.155 cm normal to the chord line. This is the value used to calculate the entries for $\bar{x}_m$, $\bar{y}_m$ (air on) in Table 6.

Model Coordinates. -- The measurements just described established the location of a portion of the real model surface in Figure 26 under actual test conditions. It remained to find the

angle of incidence $\alpha$, which was needed to define the transformation from $(\bar{x}, \bar{y})$ coordinates to $(x, y)$ coordinates. From Figure 26, after a preliminary rotation to intermediate coordinates $(x', y')$ and a change in sign for $y'$,

$$\begin{aligned} x' &= \bar{x} \cos \alpha + \bar{y} \sin \alpha \\ y' &= \bar{x} \sin \alpha - \bar{y} \cos \alpha \end{aligned} \qquad (9)$$

The procedure was to superpose the ideal airfoil on the measurements in these intermediate coordinates $(x', y')$. The calculation was iterative, because the angle $\alpha$ was not known initially. The surface of the ideal airfoil of unit chord is defined by Equations (4) - (5). The chord of the real airfoil was 90.12 cm. After some experimenting, it was found that acceptable agreement could be achieved by taking the angle of incidence as

$$\alpha = 13.87 \text{ degrees}$$

and by placing the chord line in Figure 26 along the line

$$y' = -96.59 \text{ cm}$$

between the end points

$$-20.86 < x' < 69.26 \text{ cm}$$

After these preliminaries, the airfoil surface in coordinates $(x, y)$ was finally obtained by a translation,

$$\begin{aligned} x &= x' + 20.86 \text{ cm} \\ y &= y' + 96.59 \text{ cm} \end{aligned} \qquad (10)$$

Residual discrepancies between the real and ideal surfaces are listed in the last column in Table 6, where the notation $c\eta_s$

denotes a value computed from Equation (5) above. By coincidence, the rear corner at the trailing edge coincided for the real and ideal airfoils. The real surface showed a wavy pattern, with a wave length of about 25 cm and an amplitude of about 0.01 cm. This irregularity was probably caused by poor technique in bonding the skin and ribs of the airfoil mold to each other, inasmuch as epoxy was applied in several spanwise strips, working forward from the trailing edge, on successive days. The discrepancies are unlikely to be important from the aerodynamic point of view.

Data Placement. -- Finding the position of the sampled data in Figure 26 was a separate problem whose solution involved a second application of the optical proximity sensor. Data acquisition was controlled by a square-wave ENCODER signal having 256 pulses per revolution. At each positive-going transition of this ENCODER signal, a burst of 12 data samples was transferred to the computer at a word rate of 200 kHz. To mark the beginning of each revolution, a magnetic pickup and a single-tooth gear generated an INDEX pulse when the rotor was approximately horizontal. This INDEX pulse was positioned electronically to fall in the gap between two data bursts. Its primary purpose was to aid in self-synchronization and error detection, in a manner described under "Programming and Control" in Section 2.5 above and in more detail in Section 5.3 of CCW.

To determine the angular position of the rotor when the

first burst of hot-wire data was acquired following the INDEX pulse, the rotor was first leveled in the horizontal position, using a sensitive spirit level, and clamped. The rotor was next traversed vertically past a narrow reflecting target. The measured sensor output as a function of traverse position is shown in Figure 28. The vertical traverse was then placed at the position corresponding to half-amplitude output on the leading edge of this signal; i.e., the point marked "trigger level", and the rotor was set in motion at standard speed (6.25 rev/sec). Two time intervals, from the trigger point of the sensor signal

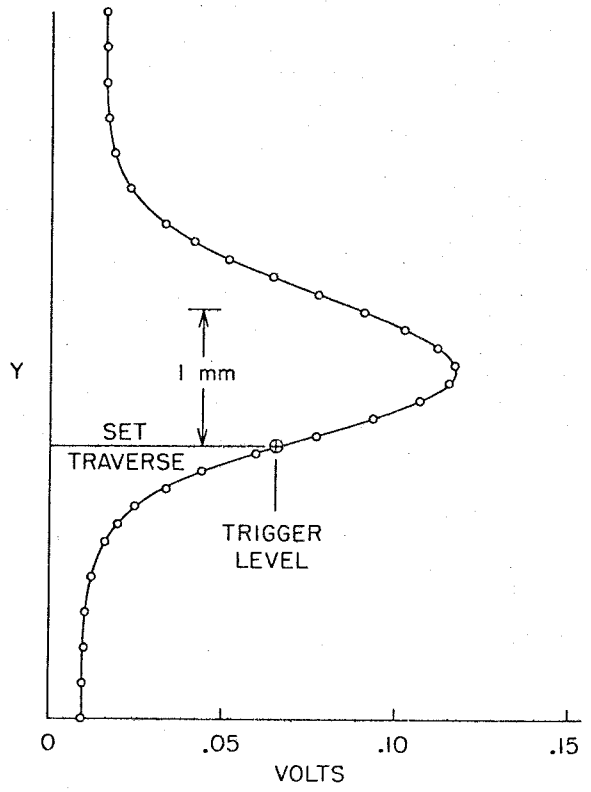


Figure 28. Output of optical proximity sensor during vertical traverse past narrow stationary target with rotor clamped in horizontal position.

to the leading edge of the INDEX pulse, and from the leading edge of the INDEX pulse to the leading edge of the next ENCODER pulse, were measured separately. The sum was 481 + 153 = 634 μsec, corresponding to 1.43 degrees of rotation. To this was added 50 μsec for the average delay to the center of the four hot-wire samples, giving 684 μsec or 1.54 degrees. Finally, the probe offset angle of 5.64 degrees was added, giving a total angle of 7.18 degrees from the horizontal reference to the probe position for the first data frame, as indicated in Figure 26.

Hot-wire data are identified by file, by revolution, by frame, and by wire. The probe angular position for frame n, measured in degrees from the vertical, is denoted by $\phi$ in Figure 26. Evidently

$$\phi_n = \phi_1 + \frac{360}{256}(n-1) \qquad (11)$$

where, from the measurement just described,

$$\phi_1 = -82.82 \text{ degrees}$$

During the main experiments of this research, probe 2 was mounted on arm 1 and connected to ADC channels L-0, L-1. Probe 1 was mounted on arm 2 and connected to ADC channels L-2, L-3 (the system used for naming the individual wires is explained in Figure 31c below). From Table 5, the corresponding radii are

$$R_1 = R_{01} = 75.748 \text{ cm}$$

$$R_2 = R_{23} = 75.684 \text{ cm}$$

where the subscripts identify the arm (not the probe) and/or the ADC channel assignments. From Figure 26, the probe position $(\overline{x}, \overline{y})$ in traverse coordinates is

$$\begin{aligned} \overline{x} &= X - R \sin \phi \\ \overline{y} &= Y + R \cos \phi \end{aligned} \qquad (12)$$

The probe position (x, y) in airfoil coordinates then follows from Equations (9) and (10).

Accuracy. -- Our best estimate of the accuracy of these rather delicate measurements is that the airfoil may be misplaced by 0.02 cm in x, by 0.01 cm in y, and by 0.01 degrees in angle of incidence. The probe radius is uncertain by 0.005 cm. The position of the data points along the probe arc may be uncertain by as much as 0.1 cm over and above the effect of non-simultaneous sampling, because of strut deflection and also because of systematic local irregularities in the ENCODER signal.

Some further uncertainty in relative position arises from vibration and buffeting of both model and strut. During the main measurements, the recorded data routinely included the peak voltage reading from the optical proximity sensor (as an average over each revolution). The boundary-layer traverse (files 73-84 of Table 8 below) showed a sensor sensitivity of about 4.4 volts/cm at closest approach as the probe arc was displaced nearly normal to the airfoil surface. During the grazing traverse (files 52-73 of Table 8), the observed peak-to-peak excursion in sensor voltage during a file was about 0.15

volts, corresponding to a peak-to-peak displacement of about 0.034 cm. The rms voltages and displacements were about one-fourth of these values. If this excursion were all caused by displacement of the airfoil normal to the chord, the peak-to-peak motion would be 0.035 cm, i.e., about a quarter of the mean deflection under aerodynamic load. If the excursion were all caused by displacement of the strut and rotor hub in the streamwise or soft direction, the peak-to-peak motion would be 0.080 cm. Both estimates are reasonable, and the actual motion is probably a combination of the two. According to these data, incidentally, the smallest clearance ever observed between probe and model was 0.055 cm, during some revolution of File 57.

4.2 Hot-wire Calibration

An attractive feature of the flying hot wire is access to automatic calibration of X-arrays in pitch. From the point of view of a probe rotating in a uniform stream, the relative velocity consists of a steady head-on component $\omega R$ and an unsteady component of fixed magnitude $u_\infty$ whose direction rotates at a constant rate. The relative importance of the two components is specified by a parameter $K = \omega R/u_\infty$. The resultant velocity q in laboratory coordinates is illustrated in Figure 29 for a value of K near unity.

Probe Acceptance Angle; Wake Interference.--It is useful to know in advance the part of the probe arc for which the flow direction relative to a conventional 90-degree X-array lies within

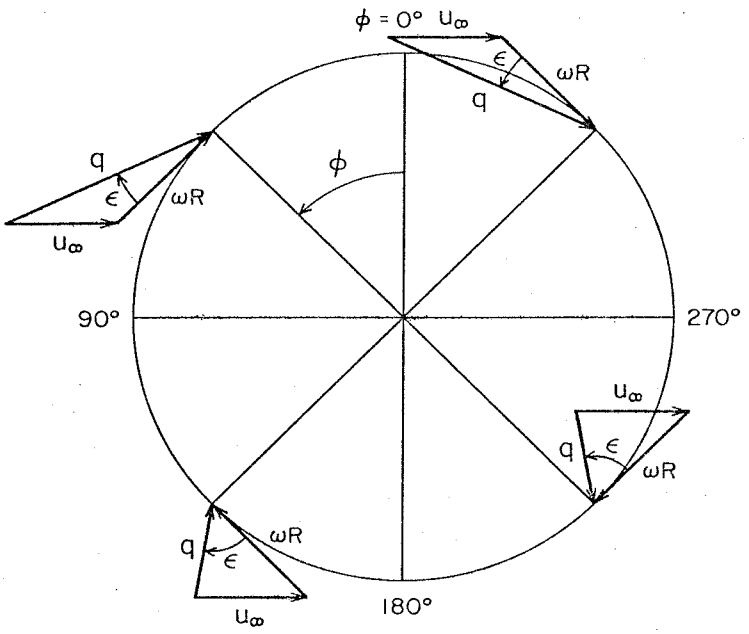


Figure 29. Flow relative to flying-hot-wire probe in laboratory coordinates. Uniform ambient flow is from left to right. Probe angular displacement $\phi$ is measured from top dead center and increases for counter-clockwise rotation. Relative flow angle $\varepsilon$ is measured from direction of probe motion to direction of relative velocity vector and is positive when relative flow is toward rotor hub.

the theoretical acceptance angle of $\pm$ 45 degrees from the probe axis. For very slow or no rotation ($K << 1$), the useful range is $\pm$ 45 degrees on either side of top dead center for the rotor arm. For very fast rotation ($K >> 1$), the relative flow direction will always be within the acceptance angle. The boundary observed experimentally for one of our probes, as defined by a shallow minimum in one or the other wire voltage, is shown by the open points in Figure 30. The dashed line is an ideal or calculated boundary (for details of the calculation, see Section 2.1 of CCW).

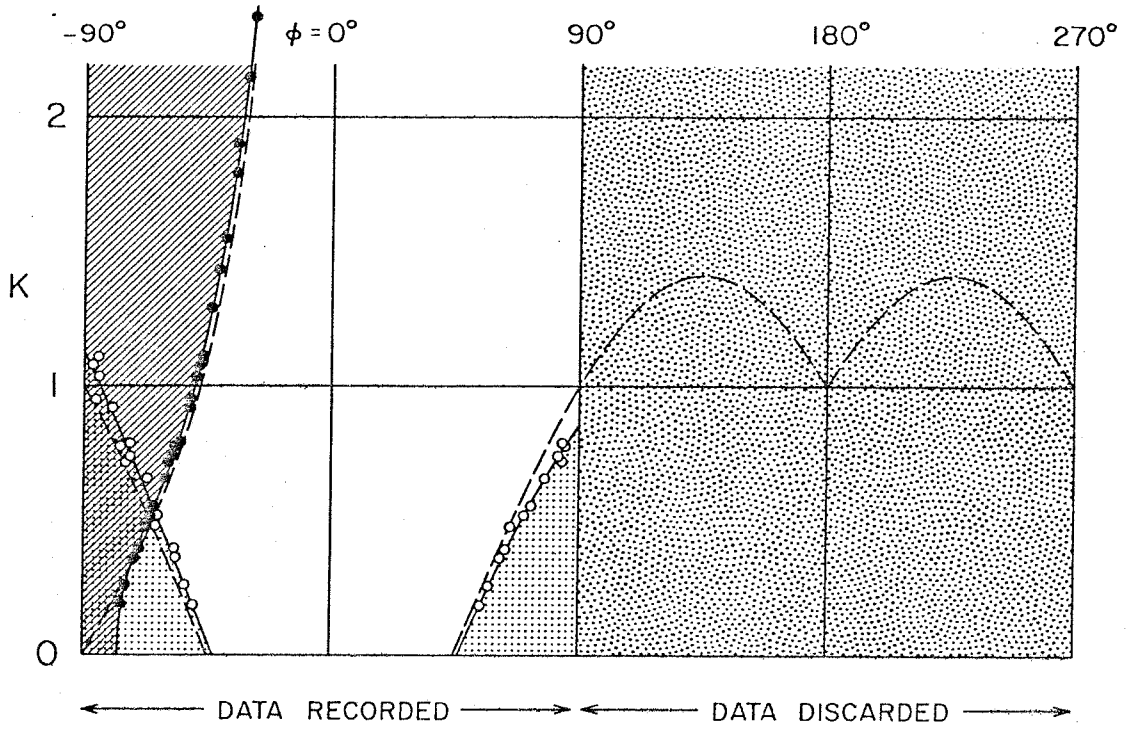


Figure 30. Experimental wake-interference boundary (solid points) and maximum-flow-angle boundary (open points) compared to ideal boundaries (dashed lines) calculated for a uniform stream. Angle $\phi$ is arm position defined as in Figure 26, without regard to probe offset angle or timing of INDEX pulse.

The relative flow angle exceeds $\pm$ 45 degrees, and the probe is therefore unusable, in the dot-shaded region.

As the rear rotor arm passes through the horizontal position, moving upward, the rear probe encounters the wake left behind by the front rotor arm during the preceding half-revolution. The experimentally observed boundary for such encounters, as defined by a non-zero value for intermittency, is shown by the solid points in Figure 30. Wake interference occurs in the slant-shaded region. The dashed line is again a calculated boundary (see Section 2.2 of CCW). The probe trajectory in the

figure is horizontal, from left to right, at the level defined by the ratio $K = \omega R/u_\infty$. The left half of the figure represents the upper half-revolution for a given probe, and is the region for which data are normally recorded. If the ratio K is close to unity, as in the present experiments, approximately the first quarter of the upper half-revolution is subject to wake contamination of the kind just described.

In practice, the tip speed during calibration was usually fixed at about one-third to one-half of the stream speed, primarily to avoid wake interference. The tip speed was increased to be essentially equal to the stream speed during the actual measurements, primarily to reduce the probability of encountering unacceptable angles for the relative flow.

Calibration Flow. -- Figure 30 and the preceding discussion apply for wire calibration in a uniform stream. For the present experiments, it was impractical to remove the airfoil model from the test section during wire calibration. Instead, the airfoil was pitched to its angle of incidence for zero lift, -4 degrees, and the calibration arc was placed as high and as far to the rear as possible. The resulting calibration geometry is shown in Figure 31a. To define the real calibration flow experimentally, one hot-wire probe was replaced by a pitot-static tube. The rotor was then clamped in the vertical position, and the dynamic and static pressures were measured at six points along the calibration arc. This process was repeated at each of the dynamic pressures used for wire calibration. The results

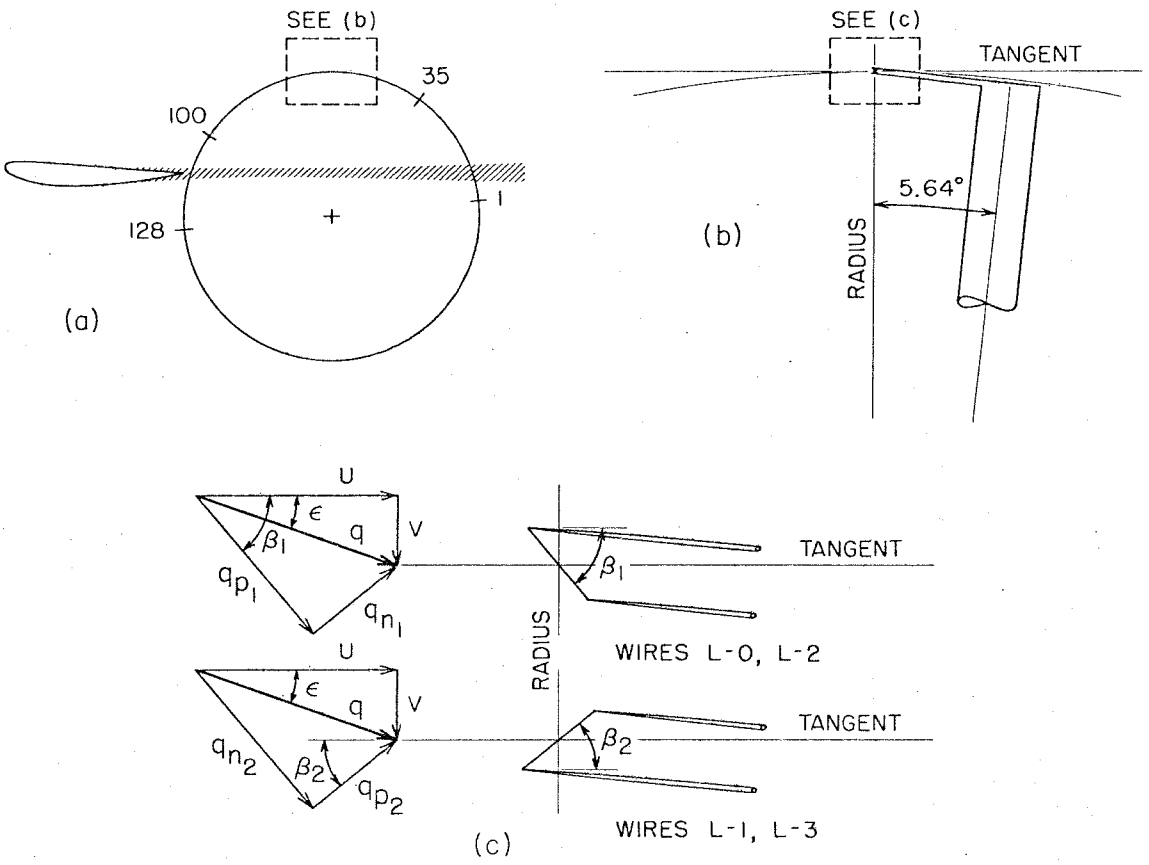


Figure 31. Details of probe geometry, including notation for relative velocity components.

(a) Probe trajectory during wire calibration. Flow is from left to right, with airfoil at zero lift. Probe rotation is counter-clockwise. Location of frames 1, 35, 100, 128 is marked on calibration arc.

(b) Closeup view of rotor tip showing probe angular offset of 5.64° (cf. Figure 6).

(c) Resolution of relative velocity (q) into tangential (U) and radial (V) components with respect to probe circle, and also into normal ($q_n$) and parallel ($q_p$) components with respect to wires. All quantities are positive as shown.

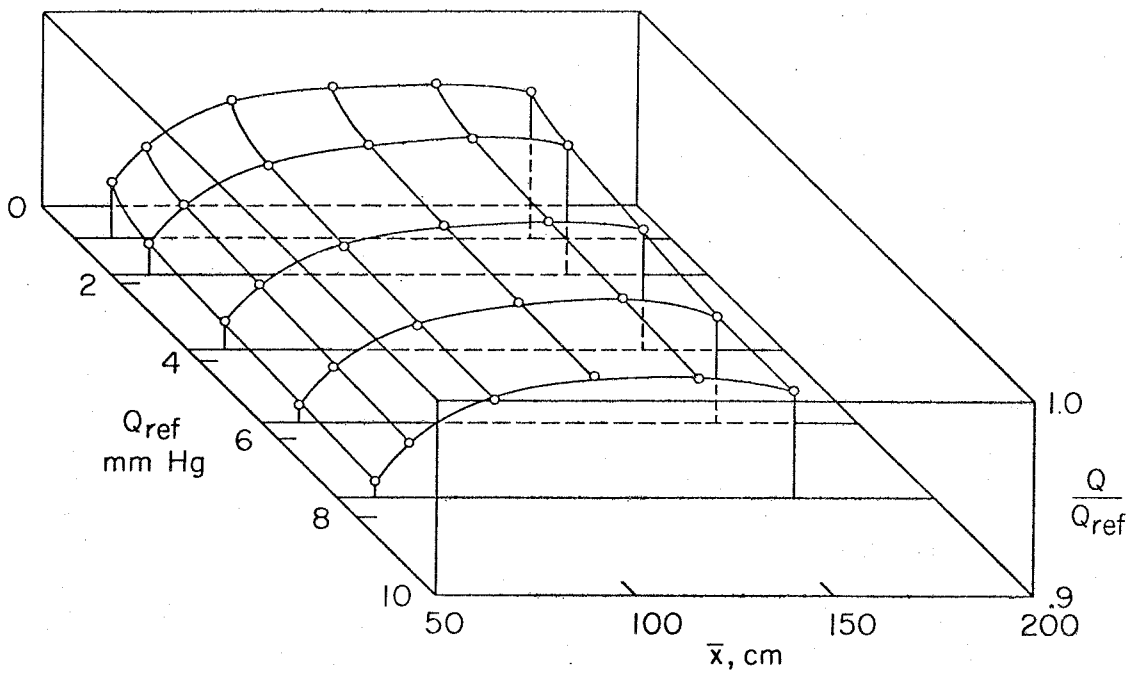


Figure 32. Dynamic pressure along calibration arc (as a function of probe position $\bar{x}$ in tunnel coordinates) for several tunnel dynamic pressures $Q_{ref}$.

for the five highest tunnel speeds, together with a fit to a quartic polynomial in $\bar{x}$, are shown in Figure 32. The magnitude of the free-stream velocity vector along the calibration arc was thus known to sufficient accuracy (the direction of the free-stream velocity vector is discussed under "Practical Example" below).

Inversion Algorithm. -- The flying-hot-wire technique encounters several problems which are not typical of the ordinary art of hot-wire anemometry. One problem is that the probe calibration arc occupies a considerable fraction of the tunnel test section, and nonuniformities of the calibration flow along this arc may be important. A second problem is that absolute errors

in measured velocity are conserved, and relative errors are therefore at least doubled, during conversion from a reference frame fixed in the probe to a reference frame fixed in the tunnel. A third problem is that calibration of wire arrays is required over an unusually large range of velocities. Finally, a fourth problem is that the technique, being by definition digital, requires the operation of inversion of voltage pairs to obtain velocity vectors to be carried out a very large number of times in a digital computer. The first three problems involve accuracy, and are eased by increasing the number of parameters in the formulas representing wire response. The fourth problem involves cost, and is eased by decreasing the number of parameters, for the sake of an efficient inversion algorithm. Our experience suggests that the fourth problem should take precedence unless computing costs are dominated by processing which takes place after inversion. In the present experiments, for example, the inversion operation was carried out nearly thirty million times. An extra two milliseconds of core time per inversion (say) should therefore really be viewed as an extra fifteen hours of core time per experiment.

An X-array is calibrated by subjecting the probe to known velocities (U, V) in the plane of the array and measuring the resulting wire voltages ($e_1$, $e_2$) for a fixed difference $\Delta T$ between wire temperature and air temperature. It is common practice to express the calibration parametrically in terms of effective velocity components ($q_{e_1}$, $q_{e_2}$) which are normal or nearly normal

to the two wires of the array. In what follows, the variables are dimensioned. All velocities, for example, have the units m/sec. Schematically, then,

$$\left.\begin{aligned} \frac{e_1^2}{\Delta T_1} &= F_1(q_{e_1}) \\ \frac{e_2^2}{\Delta T_2} &= F_2(q_{e_2}) \end{aligned}\right\} \qquad (13)$$

where

$$\left.\begin{aligned} q_{e_1} &= G_1(U, V) \\ q_{e_2} &= G_2(U, V) \end{aligned}\right\} \qquad (14)$$

Any practical use of such a calibration must consider the opposite operation of inversion. It is assumed here that a given voltage pair implies a given velocity vector, and vice versa, without regard to wire separation, signal amplitude, the unknown third velocity component, frequency and scale of the fluctuations, and the like. Then, again schematically,

$$\left.\begin{aligned} q_{e_1} &= f_1\left(\frac{e_1^2}{\Delta T_1}\right) \\ q_{e_2} &= f_2\left(\frac{e_2^2}{\Delta T_2}\right) \end{aligned}\right\} \qquad (15)$$

and finally

$$\left.\begin{aligned} U &= g_1(q_{e_1}, q_{e_2}) \\ V &= g_2(q_{e_1}, q_{e_2}) \end{aligned}\right\} \qquad (16)$$

This calibration-inversion machinery must run smoothly in both directions. There is no difficulty with Equations (13). These are made explicit as usual by using King's law,

$$\left.\begin{aligned} \frac{e_1^2}{\Delta T_1} &= A_1 + B_1 (q_{e_1})^{n_1} \\ \frac{e_2^2}{\Delta T_2} &= A_2 + B_2 (q_{e_2})^{n_2} \end{aligned}\right\} \qquad (17)$$

The inversion equations (15) then become

$$\left.\begin{aligned} q_{e_1} &= \left( \frac{\frac{e_1^2}{\Delta T_1} - A_1}{B_1} \right)^{1/n_1} \\ q_{e_2} &= \left( \frac{\frac{e_2^2}{\Delta T_2} - A_2}{B_2} \right)^{1/n_2} \end{aligned}\right\} \qquad (18)$$

The key to efficient digital hot-wire anemometry is the form chosen for Equations (14), since these are the equations which have to be solved for (U, V). For the present experiments, the probe geometry and the notation for the relative velocities are as shown in Figure 31c. A frequent choice for $q_e$ is $q_n$, the component of velocity normal to the wire. The calibration equations (14) then take the explicit form

$$\left.\begin{aligned} q_{e_1} &= U \sin \beta_1 - V \cos \beta_1 \\ q_{e_2} &= U \sin \beta_2 + V \cos \beta_2 \end{aligned}\right\} \qquad (19)$$

and solution for U and V gives for Equations (16)

$$\left.\begin{aligned} U &= \frac{q_{e_2}\cos\beta_1 + q_{e_1}\cos\beta_2}{\sin(\beta_1 + \beta_2)} \\ V &= \frac{q_{e_2}\sin\beta_1 - q_{e_1}\sin\beta_2}{\sin(\beta_1 + \beta_2)} \end{aligned}\right\} \quad (20)$$

A more complicated form which has sometimes been proposed is $q_e = (q_n^2 + k^2 q_p^2)^{1/2}$, where $q_p$ is the component of velocity parallel to the wire, and k is a constant. Use of this form can significantly reduce the dispersion in the calibration data (see CCW, Table 2). However, the algebraic equations to be solved for U and V then become quadratic rather than linear. A modest simplification occurs if the probe axis is redefined at some intermediate stage of processing, so that $\beta_1 = \beta_2$; and this was in fact done in the present work. However, even if $k_1 = k_2$, which is unlikely, the equations which replace (20) are expensive from the computational point of view. The worst possible strategy would be to allow one or more of the wire parameters such as A, B, or n to depend on $q_e$; i.e., on Reynolds number. Inversion would then necessarily involve some iteration procedure which could be very expensive if it were pursued to a point where the increase in accuracy could justify the procedure in the first place.

The most general form for $q_e$ which preserves linearity in the inversion equations (16) is the form $q_e = q_n + \lambda q_p + C$,

where $\lambda$ and C are constants. This form should have been tried out for the present calibration, but was not, because we were not thinking clearly at the time. What was tried, with some success, was the form $q_e = q_n + C$. Thus

$$\left.\begin{aligned} q_{e_1} &= U \sin \beta_1 - V \cos \beta_1 + C_1 \\ q_{e_2} &= U \sin \beta_2 + V \cos \beta_2 + C_2 \end{aligned}\right\} \quad (21)$$

and

$$\left.\begin{aligned} U &= \frac{(q_{e_2} - C_2) \cos \beta_1 + (q_{e_1} - C_1) \cos \beta_2}{\sin (\beta_1 + \beta_2)} \\ V &= \frac{(q_{e_2} - C_2) \sin \beta_1 - (q_{e_1} - C_1) \sin \beta_2}{\sin (\beta_1 + \beta_2)} \end{aligned}\right\} \quad (22)$$

Practical Example. -- Given a commitment to Equations (17), (18), (21), and (22), wire calibration requires the determination of five wire parameters for each wire. Two of these parameters, $\beta$ and C, are needed to connect (U, V) with $q_e$. The other three, A, B, and n, are needed to connect $q_e$ with $e^2/\Delta T$.

Figure 33 shows the raw material of the post-test wire calibration for wires L-0, L-1 in terms of the relationship between the two Nusselt numbers $N = e^2/\Delta T$. Similar global response curves have recently been published by Tutu and Chevray (1975) and by Willmarth and Bogar (1977). The six symbols in the figure represent six different tunnel speeds. The two or three trajectories

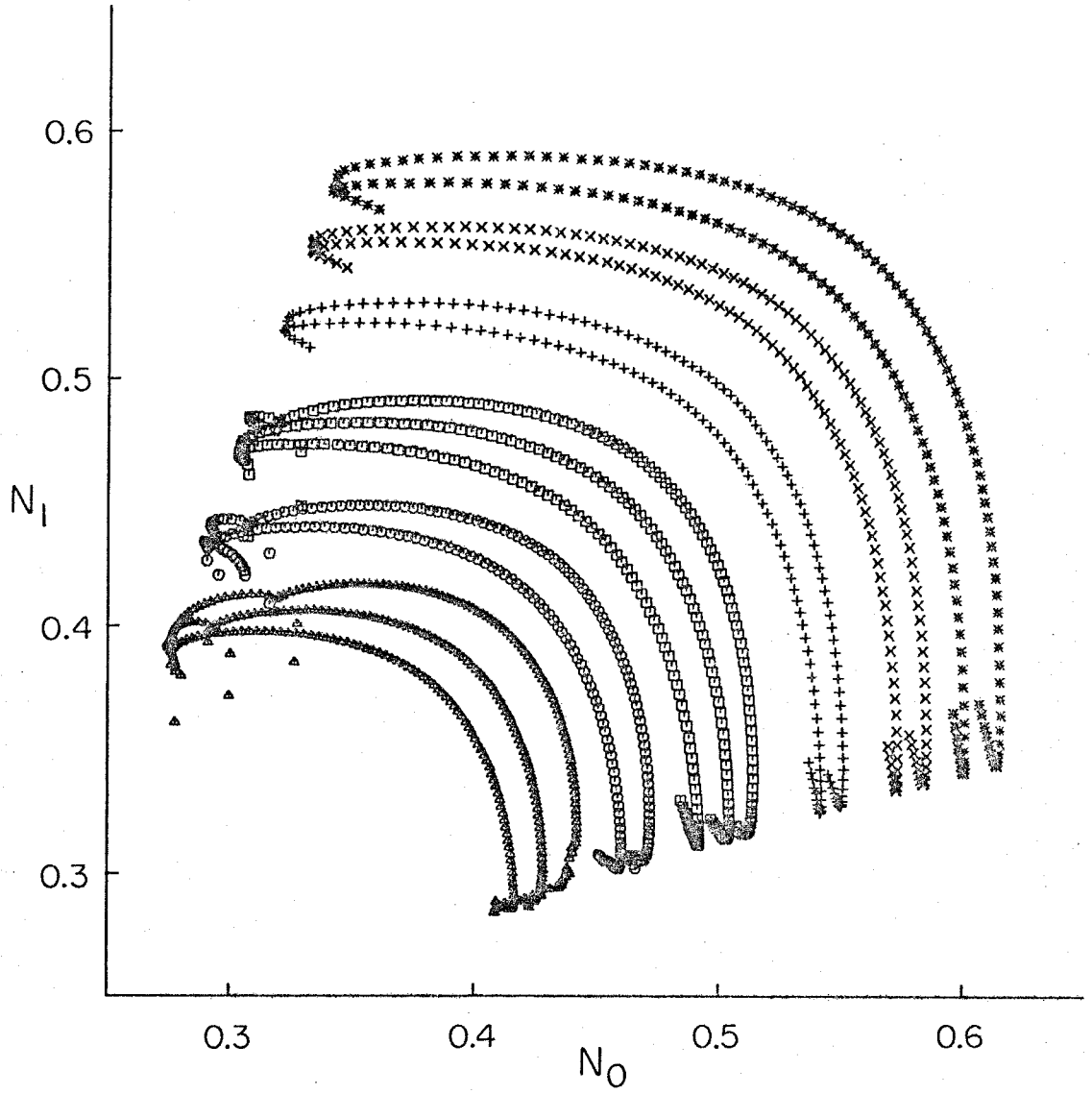


Figure 33. Raw data from one X-array (wires L-1, L-0) from post-test calibration. Quantity $N = e^2/\Delta T$ is dimensional, with units of volts$^2$/$^\circ$C. Six different symbols refer to six different values for tunnel dynamic pressure. Different curves with same symbol are for different values of $K = \omega R/u_\infty$.

with the same symbol represent different rotor speeds. The data along each trajectory are an average over 256 revolutions and represent from one to three minutes of observation. The entire calibration required a little less than two hours, mostly spent waiting for the tunnel to reach equilibrium after a change in tunnel speed.

In Figure 33, probe motion is from right to left along each trajectory. The extremities of the curves illustrate the probe behavior when the relative flow approaches $\pm$ 45 degrees to the probe axis. The voltage from the wire in nearly normal flow is then large and essentially constant, while the voltage from the wire in nearly parallel flow goes through a minimum. The disturbance at the left in some of the curves is caused by passage of the probe through the narrow airfoil wake. This disturbance, and the disturbance from the wake of the preceding rotor arm, were eliminated by restricting the calibration range to frames 35-100, which are located as indicated in Figure 31a. Within this range, only even-numbered frames were processed. The wire response, as represented by $e^2/\Delta T$, was averaged for each frame before processing, to take advantage of the low dispersion in wire voltage (about 10 to 20 millivolts rms) which is typical of data obtained during successive revolutions under calibration conditions.

The location of a given frame along the probe arc was calculated from Equation (11) of Section 4.1 above. As indicated in Figure 29, the relative velocity at the probe is the vector

resultant of the known tunnel velocity from Figure 32 (assumed temporarily to be horizontal) and the known tangential rotor velocity $\omega R$, with R taken from Table 5. The five wire parameters were determined simultaneously for each wire over the whole of the calibration range as the values which minimized the dispersion in $e^2/\Delta T$ in the parametric equations (17) and (21). Table 7 shows the values obtained (after a bootstrap correction for flow angle as described below). Note that the effect of the extra wire parameter C is to make the intercept A negative and to reduce the exponent n to about half its usual value. The angles $\beta$ listed in the table are the ones used in all subsequent processing. They are first evaluated with respect to a tangent to the probe arc, as indicated in Figure 31c, and are also listed after an adjustment of 5.64 degrees to account for nominal probe offset angle. With one exception, the adjusted values for $\beta$ are reasonably close to 45 degrees.*

Table 7

WIRE PARAMETERS (POST-TEST CALIBRATION)

| Wire | L-0 | L-1 | L-2 | L-3 |
|---|---|---|---|---|
| A (volts$^2$/°C) | -.13967 | -.30794 | -.68115 | -.34816 |
| B (volts$^2$/°C)/(m/sec)$^n$ | .28098 | .39324 | .75557 | .43348 |
| C (m/sec) | 3.30117 | 5.10370 | 4.81404 | 5.25060 |
| n | .24273 | .20569 | .13560 | .20125 |
| $\beta$ (deg) | 50.61 | 33.69 | 50.72 | 37.98 |
| $\beta \pm 5.64°$ (deg) | 44.97 | 39.33 | 45.08 | 43.62 |

*A direct optical measurement of the angle between the two wires of each probe agreed with values calculated from Table 7 within one degree. At least one of the wires was noticeably not straight.

There is one detail which was not important for the calibration, but which was perfected using the calibration for the sake of greater efficiency in later processing of the main bulk of the measurements. The velocity components (U, V) were actually resolved not along the tangent and radius, but along effective probe axes for which the two angles $\beta_1$ and $\beta_2$ were equal. The main objective was to insure symmetry in the acceptance criterion; simplification of Equations (22) was a side benefit. For a perfect probe, the effective axes would be rotated clockwise in Figure 31c by 5.64 degrees. For our real probes, symmetry in $\beta$ required rotation through an effective angle $\theta$ which was worked out with the aid of Figure 31c and Table 7. For arm 1 (L-0, L-1), this rotation $\theta$ was 8.46 degrees clockwise, and for arm 2 (L-2, L-3) it was 6.37 degrees clockwise. At an intermediate stage of processing of the calibration data, any frames were discarded for which the flow angle relative to these effective axes was outside the range $\pm$ 30 degrees.

After inversion of the calibration voltages to obtain U and V, the probe velocity $\omega R$ was resolved into the same effective axes and subtracted. A final rotation produced the desired components of absolute velocity in tunnel coordinates;

$$\left.\begin{aligned} \overline{u} &= (U - \omega R \cos\theta)\cos(\phi - \theta) + (V + \omega R \sin\theta)\sin(\phi - \theta) \\ \overline{v} &= (U - \omega R \cos\theta)\sin(\phi - \theta) - (V + \omega R \sin\theta)\cos(\phi - \theta) \end{aligned}\right\} \quad (23)$$

The assumption of a horizontal calibration flow led

to systematic small discrepancies in the fit of the calibration data to King's law, Equations (17). These discrepancies were removed by a bootstrap procedure in which the direction of the calibration flow was inferred for each calibration arc from the overall calibration rather than the local one (details are given in Section 6.2 of CCW). The inferred flow angles were typically one degree or less away from the horizontal and were essentially independent of rotor speed and tunnel speed. It is by no means certain that these angles are real; i.e., that they are not caused by a defect in the formulas (21) for effective velocity $q_e$ at large relative flow angles. Moreover, the bootstrap procedure reveals only the non-constant part of the error in flow direction. Any constant error would be absorbed in the effective wire angles $\beta$ and would affect equally all of the data obtained by inversion, either for the calibration flow or for the main experiments. If the angles are real, they suggest that the free-stream flow resembled the flow in a very slow contraction. In any future application of the flying-hot-wire technique we would certainly attempt to measure the flow direction in the calibration flow directly.

4.3 Drift in Wire Parameters

Our experience during these experiments confirms a basic fact of hot-wire anemometry, which is that no two wires ever behave in quite the same way. The wire parameters are subject to continuous and often erratic drift, and also to occasional sudden discontinuities. A hot wire ages. Its surface condition

and even its geometry change because of oxidation, thermal distortion, dirt accumulation, and particle impact. The associated electronic circuits also drift, because of sensitivity to changes in ambient temperature or otherwise. The wires used for the main measurements were new and uncooked, and their properties were far from constant during the 21 hours of their use. Considerable time was spent in struggling with this problem of drift. Whatever success was achieved was due to the fact that a particular set of measurements, called a benchmark file, was repeated at frequent intervals throughout the experiments.

Use of Benchmark Files. --Figure 34 shows the location relative to the airfoil of the several data arcs of the main experiments. The usable portion of each arc begins at frame 35,

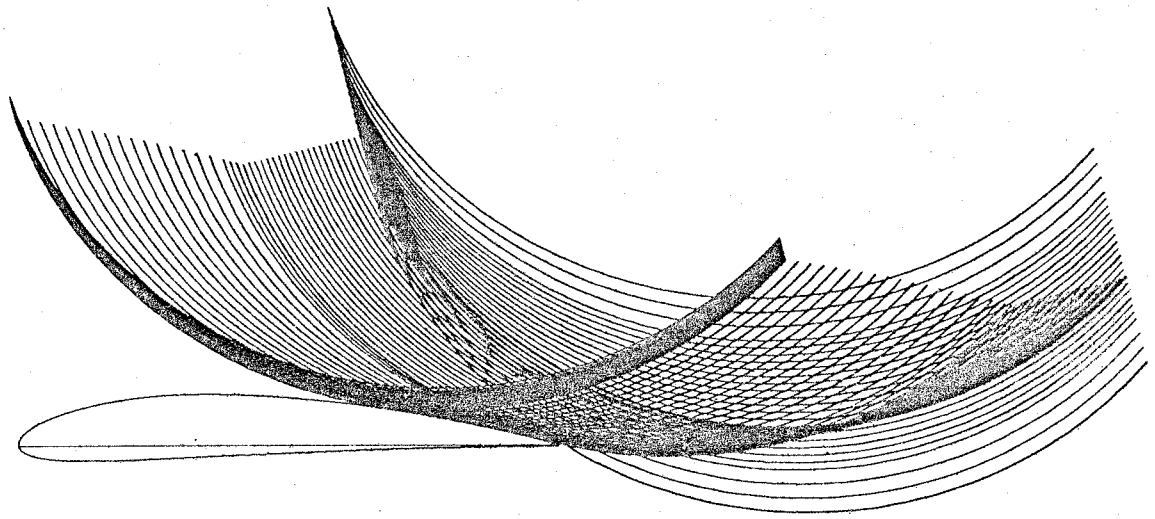

Figure 34. Location of probe trajectories for main experiments. Arcs extend from frame 35 to frame 120.

Table 8

SUMMARY OF TAPE FILES FOR MAIN EXPERIMENTS

| File No. | Time (min) | X (cm) | Y (in.) | First frame | Remarks |
|---|---|---|---|---|---|
| 1 | 0 | 75 | 16.016 | 79 | |
| 2 | 10 | 100 | 23.000 | 40 | Benchmark |
| 3 | 22 | 80 | 17.084 | 40 | |
| 4 | 29 | 81 | 17.084 | 40 | |
| 5 | 39 | 82 | 17.084 | 40 | |
| 6 | 47 | 83 | 17.084 | 40 | |
| 7 | 54 | 84 | 17.084 | 40 | |
| 8 | 63 | 85 | 17.084 | 40 | |
| 9 | 70 | 86 | 17.084 | 40 | |
| 10 | 79 | 87 | 17.084 | 40 | |
| 11 | 87 | 88 | 17.084 | 40 | |
| 12 | 94 | 89 | 17.084 | 40 | |
| (13) | 105 | 100 | 23.000 | 40 | Benchmark |
| 14 | 111 | 90 | 17.084 | 40 | |
| 15 | 148 | 91 | 17.084 | 40 | |
| 16 | 155 | 92 | 17.084 | 40 | |
| 17 | 162 | 93 | 17.084 | 40 | |
| 18 | 169 | 94 | 17.084 | 40 | |
| 19 | 176 | 95 | 17.084 | 40 | |
| 20 | 182 | 96 | 17.084 | 40 | |
| 21 | 189 | 97 | 17.084 | 40 | |
| 22 | 195 | 98 | 17.084 | 40 | |
| 23 | 201 | 99 | 17.084 | 40 | |
| 24 | 209 | 100 | 17.084 | 40 | |
| (25) | 216 | 100 | 23.000 | 40 | Benchmark |
| 26 | 224 | 100 | 22.000 | 40 | |
| 27 | 230 | 100 | 21.000 | 40 | |
| 28 | 236 | 100 | 20.000 | 40 | |
| 29 | 243 | 100 | 19.000 | 40 | |
| 30 | 249 | 100 | 18.000 | 40 | |
| 31 | 260 | 100 | 17.000 | 40 | |
| 32 | 267 | 100 | 16.000 | 40 | |
| 33 | 273 | 100 | 15.000 | 40 | |
| 34 | 280 | 100 | 14.000 | 40 | |
| 35 | 286 | 100 | 13.000 | 40 | |
| 36 | 292 | 100 | 12.000 | 40 | |
| (37) | 302 | 100 | 23.000 | 40 | Benchmark |
| 38 | 310 | 100 | 11.000 | 40 | |
| 39 | 317 | 100 | 10.000 | 40 | |
| 40 | 323 | 100 | 9.000 | 40 | |
| 41 | 330 | 100 | 8.000 | 40 | |
| 42 | 336 | 100 | 11.500 | 40 | |
| 43 | 343 | 100 | 12.500 | 40 | |
| 44 | 350 | 100 | 13.500 | 40 | |

Table 8 (continued)

| File No. | Time (min) | X (cm) | Y (in.) | First frame | Remarks |
|---|---|---|---|---|---|
| 45 | 356 | 100 | 14.500 | 40 | |
| 46 | 364 | 100 | 15.500 | 40 | |
| 47 | 382 | 100 | 16.500 | 40 | |
| 48 | 388 | 100 | 17.500 | 40 | |
| 49 | 395 | 100 | 18.500 | 40 | |
| 50 | 403 | 100 | 19.500 | 40 | |
| (51) | 412 | 100 | 23.000 | 40 | Benchmark |
| (52) | 423 | 80 | 17.084 | 40 | Repeat of file 3 |
| 53 | 432 | 79 | 16.870 | 80 | Error in tunnel temperature at revolution 1954 |
| 54 | 441 | 78 | 16.655 | 80 | |
| 55 | 453 | 77 | 16.441 | 80 | |
| (56) | 463 | 75 | 16.016 | 79 | Repeat of file 1 |
| 57 | 471 | 73 | 15.596 | 78 | |
| 58 | 482 | 71 | 15.184 | 78 | |
| 59 | 494 | 69 | 14.780 | 77 | |
| 60 | 504 | 67 | 14.381 | 76 | Followed by tunnel shutdown |
| (61) | 550 | 67 | 14.381 | 76 | Repeat of file 60; discontinuity for wire L-0 at rev 207; parity error in record 253 |
| 62 | 559 | 65 | 13.989 | 75 | |
| 63 | 573 | 63 | 13.605 | 75 | |
| (64) | 585 | 100 | 23.000 | 40 | Benchmark |
| 65 | 596 | 61 | 13.228 | 74 | |
| 66 | 607 | 59 | 12.858 | 73 | |
| 67 | 616 | 57 | 12.495 | 73 | |
| 68 | 626 | 55 | 12.139 | 72 | |
| 69 | 635 | 53 | 11.788 | 71 | |
| 70 | 643 | 51 | 11.443 | 70 | |
| 71 | 652 | 49 | 11.103 | 70 | |
| 72 | 661 | 47 | 10.770 | 69 | |
| 73 | 669 | 45 | 10.443 | 68 | |
| 74 | 677 | 45 | 10.343 | 68 | |
| 75 | 684 | 45 | 10.243 | 69 | |
| 76 | 690 | 45 | 10.143 | 69 | |
| 77 | 696 | 45 | 10.000 | 69 | |
| 78 | 702 | 45 | 9.850 | 69 | |
| 79 | 715 | 45 | 9.700 | 70 | |
| 80 | 722 | 45 | 9.550 | 70 | |
| 81 | 728 | 45 | 9.400 | 70 | |
| 82 | 735 | 45 | 9.250 | 70 | |
| 83 | 740 | 45 | 9.100 | 71 | |
| 84 | 747 | 45 | 8.900 | 71 | |
| (85) | 758 | 100 | 23.000 | 40 | Benchmark |

to avoid wake interference, and ends at frame 120, to avoid large relative flow angles. There are 85 data files, which are listed in sequence in Table 8. Of these, 76 are distinct. The other nine (marked by parentheses in the table) are duplicates, mostly benchmark files.

The main events of the main experiments were the pre-test calibration, the horizontal, vertical, grazing, and boundary-layer traverses, the post-test calibration, and two vertical traverses through the wake with the probe fixed rather than flying. The pre-test calibration was intended to anchor one end of the drifting data. However, at different times in the course of this calibration, three of the four wires showed sudden small changes in response. No way was found to pull the data together, and the pre-test calibration had to be discarded.

There remained the post-test calibration. Drift was ignored when these calibration data were processed as described under "Practical Example" in Section 4.2. As a normal precaution, one early calibration run was duplicated at the end. Excellent repeatability was found for three of the four wires. The fourth wire, L-2, showed a change of about 0.002 in $e^2/\Delta T$. If this change was sudden, it did not occur while calibration data were being recorded. The associated error in velocity or angle was small enough to be neglected.

The benchmark files are represented by the lowest arc in Figure 34. The traverse position was always X = 100 cm, Y = 23 inches (See Figure 26 above for the traverse geometry).

The key to control of drift was the determination of the mean velocity along the portions of the benchmark arc which lay outside the turbulent region. The various wire parameters could then be established for Files 2, 13, 25, 37, 51, 64, and 85, and could presumably be established for all other files by linear interpolation in time. Execution of this strategy required several months, and is described here only in outline.

The basic assumption, designed to be checked a posteriori, was that the wire parameters changed continuously and linearly with time during the 5.3-hour period spanning the last two benchmark runs (Files 64 and 85) and the post-test calibration. The procedure is illustrated in Figure 35. It became apparent early in this procedure that the two wire parameters B and $\beta$ could be held constant at the calibration values listed in Table 7 above. Only variations in the wire parameters A, C, and n had to be accounted for. The wire parameters obtained from the calibration (the star symbols in the figure) were first used to invert the data for the last benchmark run, File 85. For simplicity, since the benchmark data in question lay outside the turbulent region, a mean Nusselt number $e^2/\Delta T$ was defined for each wire for each frame of data using the mean square voltage. The velocity field thus determined for the benchmark arc was then treated as if it were a known calibration flow, and wire parameters were inferred for File 64. The values obtained in the case of wire L-1 and L-2 are shown by the triangles connected by a dashed line in Figure 35. To enforce the

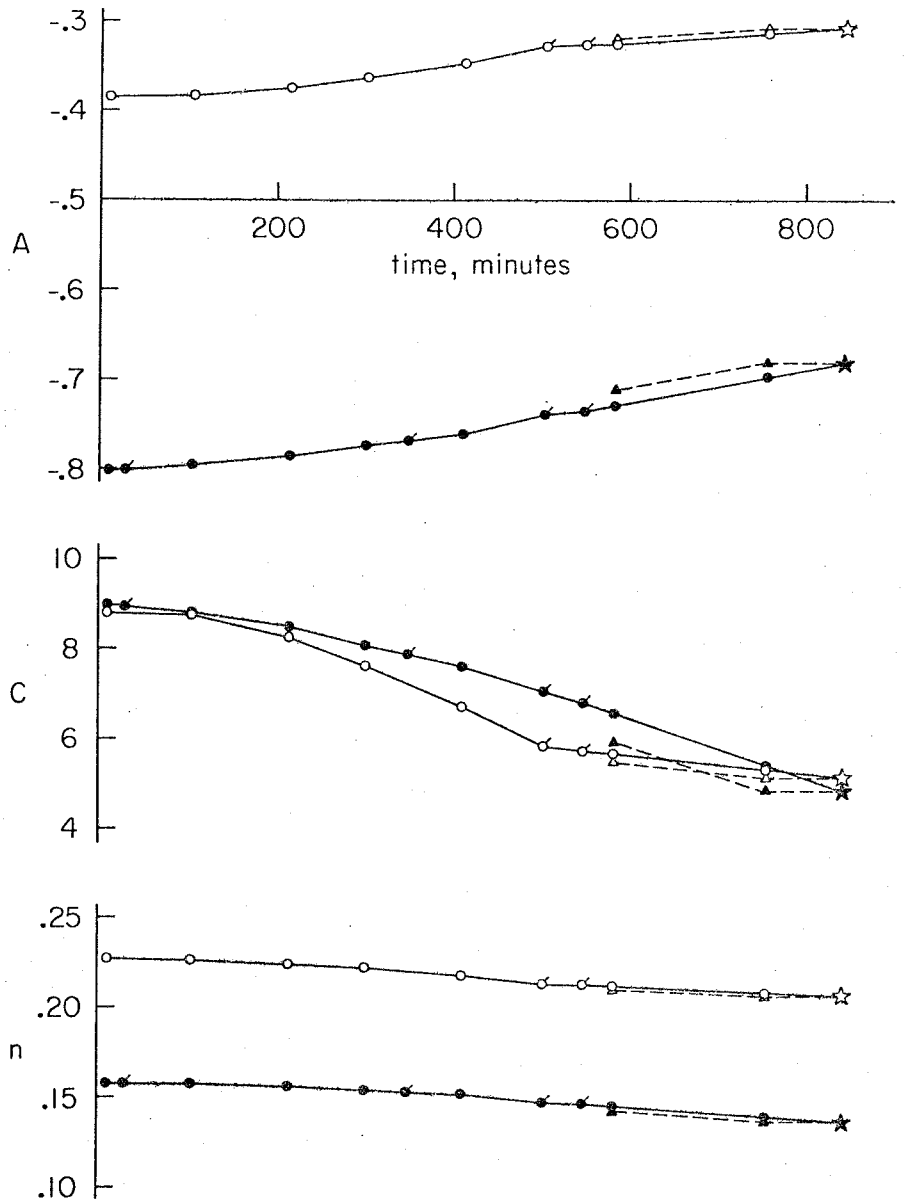


Figure 35. Drift in wire parameters A, C, and n with time. Open symbols: wire L-1. Solid symbols: wire L-2. Star: calibration value. Triangles connected by dashed lines: first approximation for last two benchmark runs. Circles connected by solid lines: final values for all benchmark runs. Flagged symbols show location of local adjustments described in text.

assumption of a constant drift rate, the wire parameters for the two benchmark runs were next displaced upward or downward to lie on a line through the wire parameters from the post-test calibration (the latter parameters were placed in time at the midpoint of the calibration period). This process defined new wire parameters for File 85 and eventually also for File 64. Iteration continued until there was no further change. Given the final velocity variation along the benchmark arc, wire parameters for the remaining benchmark files could then be calculated as shown by the circles connected by a solid line in Figure 35. The variation of the parameters with time was found to be monotonic, reasonably smooth, and large.

Since the wires did not necessarily have to be on the same arm, four wire arrays were available for this process of determining the velocity along the benchmark arc. All combinations were tried, and the final version of the benchmark processing was actually done with wires L-1, L-2, which were on different arms but which showed the most consistent overall behavior (in spite of the slight problem with repeatability during the post-test calibration for wire L-2). The small difference in arm radius of 0.064 cm (see probe 2 on arm 1 and probe 1 on arm 2 in Table 5) was accounted for by using the mean radius.

Glitches. -- The main measurements were made with a steady rhythm which was broken only once, between Files 60 and 61, when some adhesive tape holding several pressure lines to the tunnel floor came loose and had to be replaced. The tunnel

was shut down briefly. So was the rotor, because the moving probe was manifestly dangerous to a man in the test section. This shutdown was followed immediately, perhaps as punishment, by the appearance of the only parity error on the main data tapes (in record 253 of File 61) and also by a large discontinuity of about 100 millivolts in the response of wire L-0 (at revolution 207 of File 61). This discontinuity is displayed in Figure 36. The remedy was to discard the early part of File 61 for the wire pair L-0, L-1 and to apply the same procedure used for the benchmark files. That is, the velocity determined by the wire pair L-1, L-2 outside the turbulent region in File 61 was taken as a calibration flow for the other two wires for File 61 and then for the duplicate File 60 which preceded it.

At this stage the wire parameters were determined for all four wires for all 85 data files. These parameters were used with proper wire pairs in a pseudo-inversion of the whole of the data, each frame again being represented by four mean values of $e^2/\Delta T$ as in the benchmark processing already described. When mean velocities from the two probes were compared frame by frame and overall, three slight difficulties appeared elsewhere in the data.

The vertical traverse (Files 25-51 in Table 8) was a round trip which went from one edge of the flow field to the other and returned, stopping at intermediate positions. For several typical frames, the interleaved data were found to be smooth and consistent for arm 1 (wires L-0, L-1) but not for

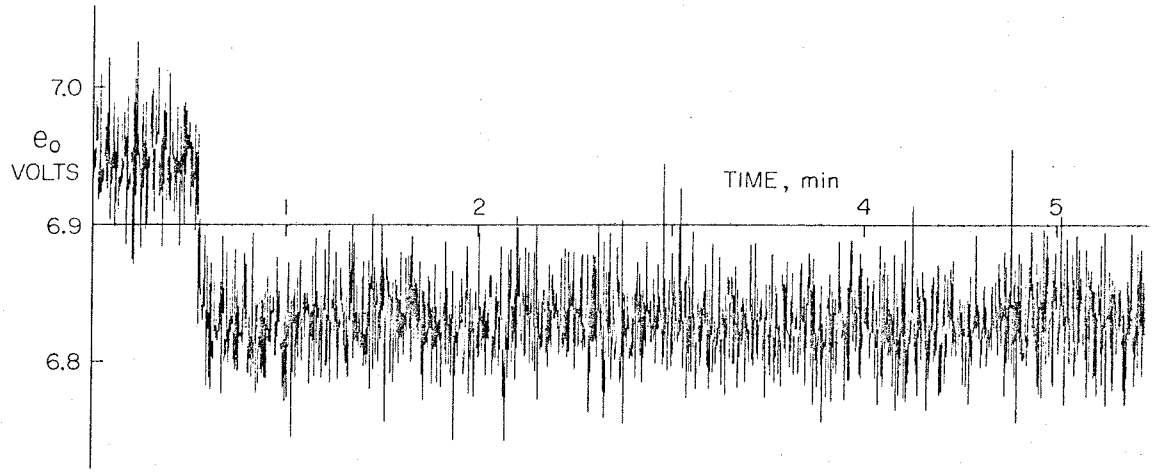


Figure 36. Discontinuity in voltage for wire L-0 at revolution 207 of File 61. Data shown are for frame 110, outside the turbulent region.

arm 2 (wires L-2, L-3). The latter array was therefore recalibrated at File 44, the point of maximum discrepancy, using the velocity indicated by arm 1. The same procedure was used for File 4, inasmuch as a comparison of duplicate Files 3 and 52 showed good repeatability for arm 1, but not for arm 2. In the grazing traverse (Files 52-73 of Table 8), the velocity indicated by the two probes showed a maximum discrepancy at File 73. In this case there was no reason to prefer one array over the other, so both were recalibrated at File 73 using the same procedure as for benchmark files (i.e., using the velocity derived from wires L-1, L-2). The points corresponding to Files 4, 44, 60, and 61 are shown flagged in Figure 35.

After these three repairs, the mean velocities in laboratory coordinates obtained from the two probes were in agreement

everywhere within one or at most two percent of the reference velocity. After the full inversion process was carried out, as described in the next Section 4.4, one additional error was found in File 53. For both arrays, the turbulence level in the free stream was abnormally large for this file, indicating a lack of homogeneity in the populations. Inspection revealed that the tunnel temperature for revolution 1954 was recorded with the wrong sign by the data system, so that $\Delta T$ was in error by about $50^{\circ}$ C. The four-revolution record containing the offending revolution was discarded, and the inversion of this file was repeated.

4.4 Data Inversion

Data Preparation. -- Inversion required application of Equations (18), (22), and (23) in sequence to each voltage pair obtained from a given wire array. The result was a sample of the instantaneous velocity vector in tunnel coordinates for the specified file, frame, and probe. Effects of slow changes in atmospheric conditions on the wire parameters A, C, and n were automatically compensated for by use of dimensioned variables and by use of benchmark files as fiducial files. During the main experiments, the tunnel temperature and reference velocity (in the form of reference dynamic pressure) were recorded only as 0.16-second averages over each revolution (see under "Editing" in Section 2.5 above). In the case of tunnel temperature, slow changes within a file were taken into account by using this local average in the calculation of the Nusselt

numbers $e^2/\Delta T$. To obtain the reference velocity required to put the data in dimensionless form after inversion, however, the average dynamic pressure over the entire file was used, together with the corresponding constant value for air density (typically $1.138 \times 10^{-3}$ gm/cc at 24.3 °C and 72.9 cm Hg). There were two related reasons, one inadvertent, for this procedure. The time constant for the pressure-measuring system was relatively long compared to the rotor period, so that use of the local average for $Q_{ref}$, which had an rms dispersion of about 0.2 percent, would by itself tend to dissociate the two variables (voltage and velocity) and increase the dispersion in the hot-wire data. The inadvertent reason emerged during the data reduction, after discovery of an interaction between the two differential manometers measuring $Q_{ref}$ and $p_m$. Both transducers had $pt_{ref}$ connected to one side. The pressure-scanning system ran in the automatic mode throughout the hot-wire measurements, switching to a new channel about every 20 seconds. When there was a large change in $p_m$ from one channel to the next, the pressure transient caused by volume adjustment in the associated transducer was detectable for two or three seconds as a spike in the signal for $Q_{ref}$. Instead of finding and discarding (or bridging) the contaminated sections of data, we chose to use the average of $Q_{ref}$ over the entire file. There was no sensible secular drift in $Q_{ref}$, and the spikes had a negligible effect on the average. One adverse effect of this choice, however, was to suppress even slow changes in $q_{ref}$ (cf. Figure 36 above)

and thus to increase slightly the dispersion in the hot-wire data. Where this dispersion was already very small, as in the free stream, the increase was by as much as a factor of two. The interaction effect just described is apparently well known to tunnel operators, and we would have been well advised to use a single fast, dedicated transducer for measurement of $Q_{ref}$.

Execution. -- The inversion process for the main experiments used the same algorithms which were earlier applied to calibration data in Section 4.2. Each voltage pair yielded a relative velocity vector (U, V), with units of m/sec, in effective probe coordinates. These vectors were treated as a homogeneous population of 2048 samples for each frame and each probe. The individual vectors were not saved. Only the mean vector and the double, triple and quadruple products of fluctuations were saved. Two passes were made through each population, one to obtain the mean and one to calculate the fluctuations and their products. This method substituted intermediate disc storage for the double-precision arithmetic which is usually required when, for example, mean and variance are determined in a single pass. For economy, the two final operations described by Equations (23) (i.e., subtraction of the relative velocity due to probe motion, and rotation of the resulting absolute velocities into tunnel coordinates) were carried out after ensemble averaging rather than before.

Except for a trivial quantity of data discarded from Files 61 and 53 (see under "Glitches" in Section 4.3 above), the number

of voltage pairs inverted was 2 x 85 x 2048 x (120 - 35 + 1) = 29,941,760. The inversion operation required about seven hours of core time in an IBM 370/158 computer (about one millisecond per inversion). We submit the results, which are preserved on 2 x 85 x 86 = 14,620 punched cards, as the raw data of the present research.* A few of the cards for the last benchmark file are listed here, to show the format;

```
85 88 1     0 0 10030  666    35   -11   38      0   0   0   0    0   0  0   0  0
85 89 1     0 0 10175  686    40   -12   41      0   0   0   0    0   0  0   0  0
85 90 1     1 0 10375  733    46   -10   44      0   0   0   0    0   0  0   0  0
85 91 1     1 0 10626  865    48    -8   40      0   0   0   0    0   0  0   0  0
85 92 1     9 0 10913 1133    65   -11   49     -1   0   0   0    0   0  0   0  0
85 93 1  2046 0  1272  243  1787  -133  381    106 -14   2  -1  114  -8  9  -2  6
85 94 1  1974 0 -1464 -717  1048   235  565     27  16  16  23   37  11 10   6 14
85 95 1  2035 0  -954 -734  1459   545  875     66  48  44  57   72  31 25  20 31
85 96 1  2040 0   -68 -441  2175  9791284    143  88  69  79  163  69 52  44 60
85 97 1  2043 0  1086  -13  3056 14321758    187 112  79  87  282 133 96  76101
85 98 1  2045 0  2752  641  4981 22592324    167  77  24  28  669 288181 126145
85 99 1  2047 0  5346 1458  7262 30052531   -572-273-221-149 1320 550311 191177
85100 1  2016 0  8261 2184  7087 26791944  -2071-808-489-322 1825 710370 211157
85101 1  1497 0 10387 2690  2444   878  728 -1119-411-239-158  745 273147  88 65
85102 1   518 0 11035 2785   334   121  211  -163 -81 -52 -39  119  60 34  21 16
85103 1    89 0 11165 2771    87    -1   81   -26  -7  -2  -5   18   4  1   1  1
85104 1    11 0 11209 2748    29   -13   57     0   0   0  -1    0   0  0   0  0
85105 1     2 0 11274 2722    21   -12   50     0   0   0  -1    0   0  0   0  0
85106 1     0 0 11322 2697    17   -10   45     0   0   0   0    0   0  0   0  0
85107 1     0 0 11386 2676    15    -9   44     0   0   0   0    0   0  0   0  0
85108 1     0 0 11456 2657    15    -9   43     0   0   0   0    0   0  0   0  0
```

*These punched cards have been lodged with the Large-scale Aerodynamics Branch, Flight Systems Research Division, NASA Ames Research Center. It is likely that they will be used for special purposes which are not satisfied by the results of the further processing described in Section 5.3 below. For example, they are the only surviving source of information about velocities and turbulence quantities obtained from the two probes separately.

The cards may be read with the aid of Table 9, which interprets one card quantitatively. All velocities are normalized with $q_{ref}$ (whose standard value is 27.13 m/sec), and all velocity components are resolved in tunnel coordinates; i.e., as $\bar{u}, \bar{v}$ in the notation of Figure 26 above.

Table 9

CODING OF PUNCHED CARDS (RAW DATA)

| Card columns | Variable name | Value | Divide by | To get |
|---|---|---|---|---|
| 1-2 | NFILE | 85 | | FILE 85 |
| 3-5 | NFRAME | 97 | | FRAME 97 |
| 6 blank | | | | |
| 7 | NARM | 1 | | ARM 1 |
| 8 blank | | | | |
| 9-12 | NINT | 2043 | 2048 | $\langle\gamma\rangle = 0.9976$ |
| 13-14 | NEPS | 0 | 2048 | Fraction of samples with $\lvert\varepsilon\rvert > 30^\circ$ (see Figure 29); if NEPS > 99, punch 99 |
| 15 blank | | | | |
| 16-20 | IU | 1086 | $10^4$ | $\langle u\rangle/q_{ref} = 0.1086$ |
| 21-25 | IV | -13 | " | $\langle v\rangle/q_{ref} = -0.0013$ |
| 26 blank | | | | |
| 27-30 | IU2 | 3056 | $10^5$ | $\langle u'u'\rangle/(q_{ref})^2 = 0.03056$ |
| 31-35 | IUV | 1432 | " | $\langle u'v'\rangle/(q_{ref})^2 = 0.01432$ |
| 36-39 | IV2 | 1758 | " | $\langle v'v'\rangle/(q_{ref})^2 = 0.01758$ |
| 40 blank | | | | |
| 41-45 | IU3 | 187 | $10^5$ | $\langle u'u'u'\rangle/(q_{ref})^3 = 0.00187$ |
| 46-49 | IU2V | 112 | " | $\langle u'u'v'\rangle/(q_{ref})^3 = 0.00112$ |
| 50-53 | IUV2 | 79 | " | $\langle u'v'v'\rangle/(q_{ref})^3 = 0.00079$ |
| 54-57 | IV3 | 87 | " | $\langle v'v'v'\rangle/(q_{ref})^3 = 0.00087$ |
| 58 blank | | | | |
| 59-62 | IU4 | 282 | $10^5$ | $\langle u'u'u'u'\rangle/(q_{ref})^4 = 0.00282$ |
| 63-66 | IU3V | 133 | " | $\langle u'u'u'v'\rangle/(q_{ref})^4 = 0.00133$ |
| 67-69 | IU2V2 | 96 | " | $\langle u'u'v'v'\rangle/(q_{ref})^4 = 0.00096$ |
| 70-73 | IUV3 | 76 | " | $\langle u'v'v'v'\rangle/(q_{ref})^4 = 0.00076$ |
| 74-76 | IV4 | 101 | " | $\langle v'v'v'v'\rangle/(q_{ref})^4 = 0.00101$ |
| 77-80 blank | | | | |

# V. ANALYSIS OF DATA

## 5.1 Probe Interference

Observed Effects. -- At an early stage of data processing, it became apparent from an inspection of intermittency data that there was a serious problem with probe interference. Our original expectation was that the passage of the rotor arm through the fluid would add a local increment of momentum in the direction of probe motion, but that the effect should be small because the affected fluid would move a substantial distance (two meters or more, in the case of the free stream) between successive probe passages. There is strong evidence that the effect just described was small, as expected, and that a different kind of interference was acting, arising from the extreme sensitivity of separation to slight changes in the external pressure field. Although the obstacle presented to the flow by the rotor hub was physically small, the drag was an appreciable fraction of the drag of the airfoil itself, and the blockage effect was substantial. The associated changes in velocity outside the boundary layer varied with rotor position and worked with strong leverage on the separation process.

The effect is best documented in terms of the surface pressure on the airfoil. All during the main hot-wire measurements, which required about seven hours of recording, the pressure-scanning system was running in the automatic mode, completing a cycle about every half hour (see under "Pressure

Instrumentation" in Section 2.2 above). The difference between repeated measurements of any one surface pressure was found to be strongly correlated with the streamwise position of the traverse system and almost independent of the vertical position. Some evidence on this point is shown in Figure 37 for the pressure orifices nearest the trailing edge of the airfoil. A complete quantitative record of the effect at midspan is given in Table 10. For each pressure orifice, the quantity $\Delta C_p$ is the increment between a smoothed curve of $C_p$ against rotor position and the literal (i.e., unsmoothed) value of $C_p$ from Table 2. Support for the assumed mechanism of blockage by the rotor hub is provided by the solid points in Figure 37. These points were obtained during two vertical hot-wire traverses through the wake, with the rotor clamped. They confirm that it was traverse position, and not probe rotation, which governed the magnitude of the effect. As further confirmation, surface pressures for the rear part of the airfoil have been corrected, using Table 10, for the various traverse positions associated with the pitot-static measurements of Table 3 and Figure 22. The correction for each pressure orifice was calculated using the rotor position for the nearest pitot-static-tube location. The results are plotted as the solid points in Figure 22a. The agreement between surface and external data is excellent, indicating that there was, in fact, no substantial pressure difference across the boundary layer.

Some further evidence is shown in Figure 38, in terms of

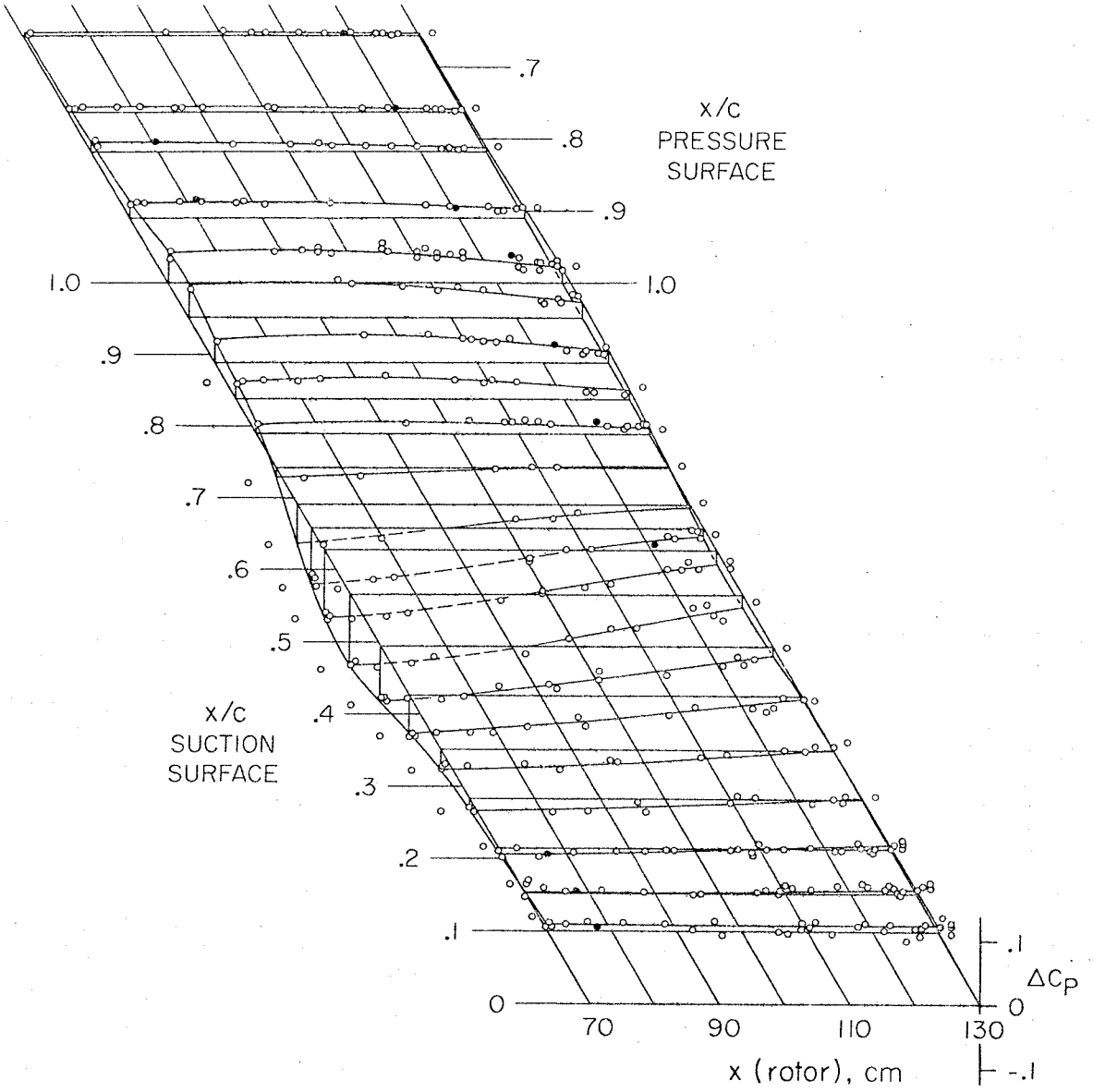


Figure 37. Effect of rotor position on surface-pressure coefficient at midspan. Quantities shown should be added to pressure coefficients from Run 87 (Table 2). Scale for x (rotor) specifies chordwise position of rotor hub in cm, measured from leading edge of airfoil. Open symbols: from main flying-hot-wire experiments. Solid symbols: from two vertical traverses with clamped rotor.

Table 10

EFFECT OF ROTOR INTERFERENCE ON $C_p$

| x(rotor) (cm) | | | 70 | 80 | 90 | 100 | 110 | 120 | 130 |
|---|---|---|---|---|---|---|---|---|---|
| Hole No. | $100\frac{x}{c}$ | $C_p$ | $\Delta C_p$ (add to $C_p$) | | | | | | |
| 1 | 100.00 | -0.352 | .045 | .049 | .050 | .050 | .045 | .035 | .025 |
| 117 | 99.14 | -0.259 | .040 | .042 | .043 | .040 | .034 | .027 | .018 |
| 120 | 91.18 | -0.022 | .023 | .024 | .024 | .023 | .021 | .018 | .015 |
| 122 | 81.87 | 0.089 | .013 | .014 | .013 | .012 | .009 | .008 | .005 |
| 124 | 76.47 | 0.126 | .007 | .008 | .008 | .008 | .007 | .005 | .004 |
| 126 | 65.96 | 0.187 | .003 | .004 | .005 | .006 | .006 | .005 | .003 |
| 128 | 58.76 | 0.234 | .004 | .004 | .004 | .004 | .004 | .003 | .003 |
| 130 | 51.66 | 0.280 | .004 | .004 | .004 | .004 | .003 | .003 | .003 |
| 132 | 44.56 | 0.321 | 0 | .001 | .001 | .001 | .001 | .001 | .001 |
| 134 | 37.64 | 0.367 | 0 | 0 | 0 | 0 | .001 | .001 | .001 |
| 136 | 30.64 | 0.419 | 0 | 0 | 0 | 0 | 0 | 0 | 0 |
| 137 | 27.08 | 0.451 | 0 | 0 | 0 | 0 | 0 | 0 | 0 |
| 138 | 23.94 | 0.478 | 0 | 0 | 0 | 0 | 0 | 0 | 0 |
| 139 | 20.74 | 0.509 | .001 | .001 | .001 | .002 | .002 | .002 | .002 |
| 140 | 15.96 | 0.572 | 0 | 0 | 0 | 0 | 0 | 0 | 0 |
| 141 | 12.80 | 0.637 | -.002 | -.001 | 0 | 0 | 0 | 0 | 0 |
| 142 | 8.10 | 0.789 | -.002 | -.001 | 0 | 0 | 0 | 0 | 0 |
| 143 | 5.06 | 0.921 | -.004 | -.004 | -.004 | -.003 | -.003 | -.002 | -.002 |
| 144 | 2.83 | 0.990 | .001 | .002 | .003 | .004 | .004 | .004 | .004 |
| 145 | 0.82 | 0.168 | .006 | .008 | .009 | .010 | .011 | .011 | .010 |
| 36 | -0.03 | -6.209 | .040 | .025 | .013 | .006 | .002 | 0 | 0 |
| 35 | 1.45 | -5.121 | 0 | -.013 | -.022 | -.025 | -.026 | -.027 | -.028 |
| 34 | 2.96 | -3.680 | .040 | .030 | .024 | .019 | .017 | .017 | .016 |
| 33 | 4.89 | -3.409 | .028 | .025 | .021 | .019 | .019 | .018 | .016 |
| 32 | 7.52 | -3.078 | .019 | .017 | .014 | .011 | .008 | .008 | .008 |

Table 10 (concluded)

| x (rotor) | (cm) | | 70 | 80 | 90 | 100 | 110 | 120 | 130 |
|---|---|---|---|---|---|---|---|---|---|
| 31 | 10.09 | -2.770 | .010 | .009 | .008 | .007 | .006 | .006 | .006 |
| 30 | 12.83 | -2.559 | .005 | .006 | .007 | .007 | .008 | .009 | .009 |
| 29 | 15.24 | -2.423 | .006 | .005 | .004 | .005 | .007 | .009 | .010 |
| 28 | 18.32 | -2.237 | -.014 | -.013 | -.012 | -.011 | -.010 | -.008 | -.005 |
| 27 | 21.45 | -2.096 | -.007 | -.006 | -.004 | -.002 | -.001 | .001 | .005 |
| 26 | 24.82 | -1.949 | -.015 | -.015 | -.014 | -.011 | -.007 | -.003 | 0 |
| 25 | 28.27 | -1.819 | -.018 | -.016 | -.013 | -.010 | -.005 | -.002 | .002 |
| 24 | 31.89 | -1.680 | -.031 | -.027 | -.024 | -.021 | -.018 | -.011 | -.006 |
| 23 | 35.08 | -1.556 | -.027 | -.024 | -.021 | -.017 | -.010 | 0 | .006 |
| 22 | 38.99 | -1.395 | -.045 | -.039 | -.032 | -.027 | -.020 | -.012 | -.005 |
| 21 | 42.51 | -1.254 | -.059 | -.053 | -.045 | -.038 | -.030 | -.019 | -.007 |
| 20 | 46.02 | -1.133 | -.070 | -.061 | -.051 | -.042 | -.031 | -.020 | -.010 |
| 19 | 49.41 | -1.017 | -.086 | -.077 | -.068 | -.056 | -.042 | -.028 | -.014 |
| 18 | 52.97 | -0.898 | -.107 | -.097 | -.086 | -.074 | -.060 | -.044 | -.026 |
| 17 | 56.63 | -0.792 | -.113 | -.106 | -.094 | -.078 | -.059 | -.038 | -.018 |
| 16 | 59.71 | -0.702 | -.116 | -.106 | -.095 | -.079 | -.060 | -.040 | -.018 |
| 15 | 62.83 | -0.630 | -.108 | -.103 | -.091 | -.074 | -.056 | -.040 | -.023 |
| 14 | 65.90 | -0.574 | -.090 | -.081 | -.070 | -.055 | -.037 | -.022 | -.011 |
| 13 | 69.13 | -0.529* | -.064 | -.055 | -.042 | -.029 | -.018 | -.008 | -.002 |
| 12 | 71.98 | -0.493 | -.034 | -.029 | -.023 | -.016 | -.008 | -.003 | 0 |
| 11 | 74.27 | -0.474* | -.016 | -.011 | -.005 | 0 | .004 | .005 | .006 |
| 10 | 78.93 | -0.444 | .015 | .017 | .017 | .018 | .017 | .014 | .010 |
| 9 | 83.77 | -0.420* | .025 | .031 | .035 | .035 | .027 | .020 | .012 |
| 8 | 88.78 | -0.407 | .033 | .040 | .043 | .043 | .035 | .025 | .015 |
| 7 | 93.07 | -0.408 | .050 | .053 | .054 | .051 | .046 | .036 | .025 |
| 6 | 95.09 | -0.406 | .048 | .052 | .055 | .050 | .045 | .036 | .025 |
| 5 | 97.41 | -0.402 | .057 | .060 | .057 | .051 | .043 | .032 | .021 |
| 4 | 98.56 | -0.397 | .047 | .050 | .053 | .050 | .044 | .032 | .018 |
| 2 | 100.00 | -0.353 | .045 | .049 | .050 | .050 | .045 | .035 | .025 |

* Interpolated value

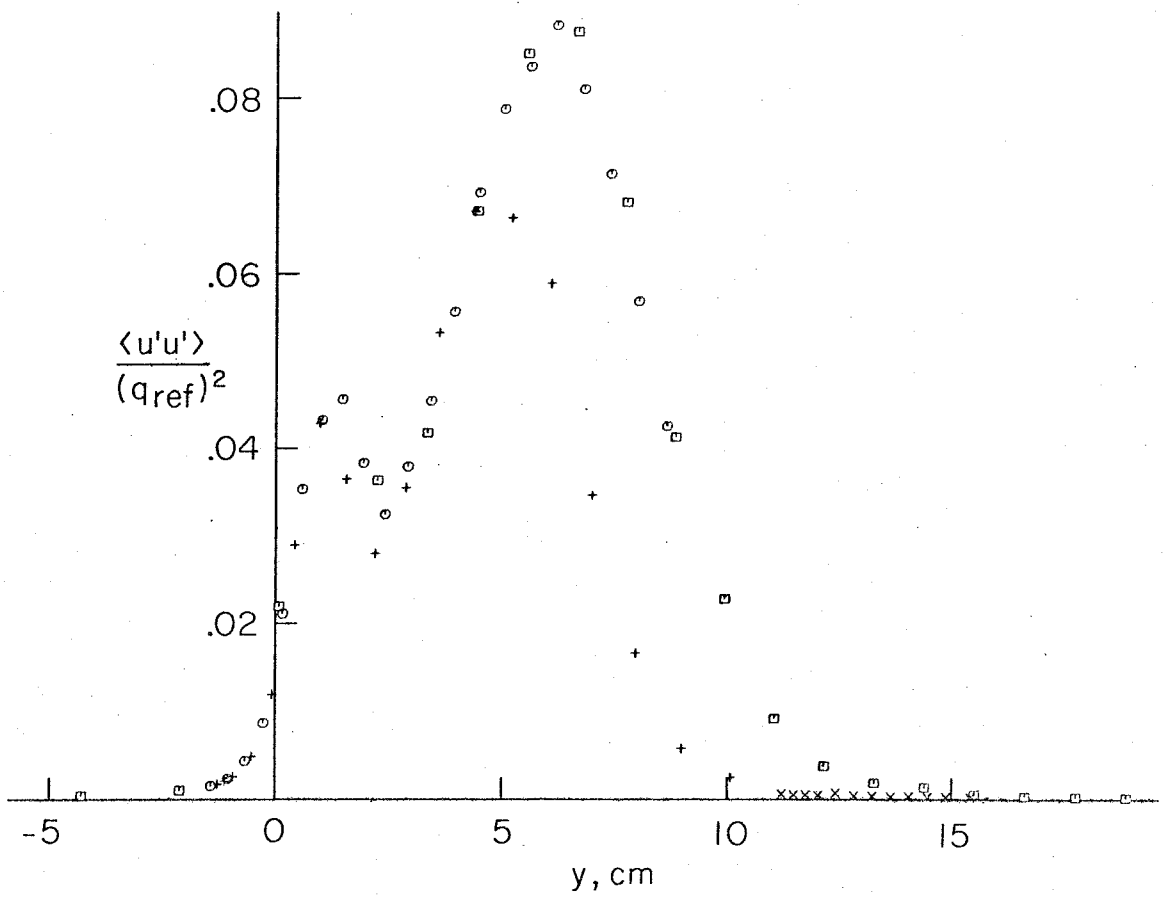


Figure 38. Effect of rotor interference on wake thickness. Dependent variable is chordwise component of turbulent energy, evaluated by linear interpolation in corrected raw data. Station is x = 98.86 cm (IX = 93; see Equations (25) ).

□ Vertical traverse
o Horizontal traverse
+ Grazing traverse
× Boundary-layer traverse

the distribution of one of the Reynolds normal stresses across the wake at a station slightly downstream from the trailing edge of the airfoil. The values plotted were obtained by linear interpolation in the raw data (after applying a correction described in Section 5.2 below). Linear interpolation means that the data from the two probes were first averaged, and then the variables

x, y, and $\langle u'u' \rangle$ were interpolated linearly for adjacent frames lying on opposite sides of the station x. The flow measured during the vertical and horizontal traverses (the symbols □ and o in Figure 38), with the rotor well downstream, is clearly not the same flow measured during the grazing and boundary-layer traverses (the symbols + and × ). In the latter case the boundary layer and wake are thinner, and the turbulence is less energetic, despite the fact that the probe is passing close to the airfoil surface near or ahead of separation. The reason is that the velocity perturbation from the rotor hub in the most upstream positions has reduced the pressure gradient over the rear part of the airfoil (cf. Figure 22a), and separation has moved rearward. The effect was not two-dimensional; the required corrections to $C_p$ at $\frac{1}{4}$- and $\frac{3}{4}$-span were found to be only 60 to 70 percent of the required corrections at midspan.

A Partial Solution. -- The scheme used to cope with this problem of blockage was to discard the hot-wire data for the part of each grazing or boundary-layer arc downstream of the last grazing or first horizontal arc. Thus the symbols + and × disappear from Figure 38. The original justification for this procedure emerged from a study of contour plots of intermittency factor. These showed that the boundary-layer thickness and wake thickness were sensibly the same for the two traverses which were exempted from the purge just described. The surviving arcs are shown in Figure 39. Because inspection of the raw data revealed slight traces of wake interference near

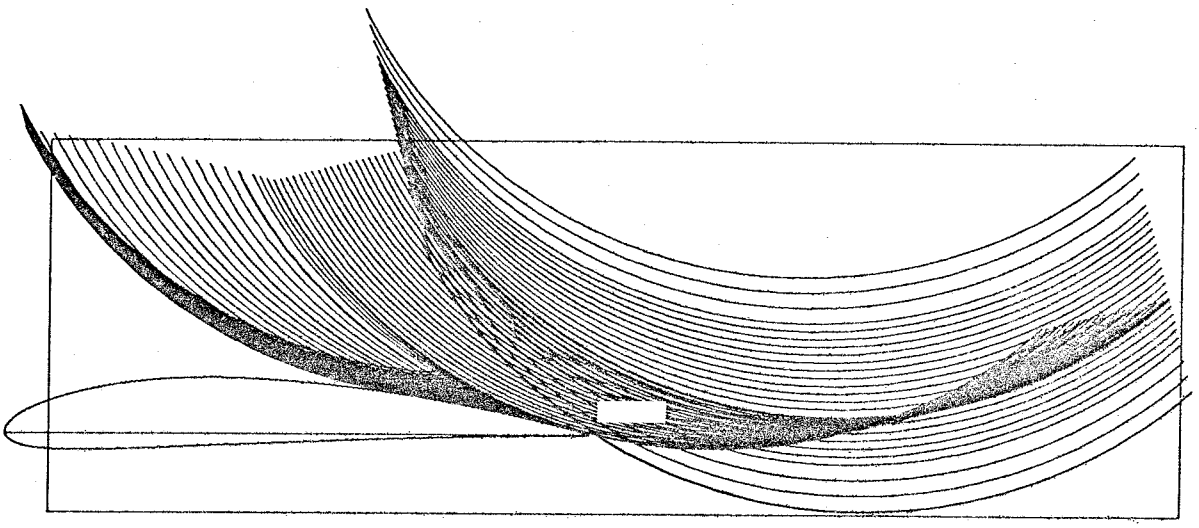

Figure 39. Location of probe trajectories for main experiments, after downstream portion of grazing and boundary-layer traverses have been deleted (cf. Figure 34). Arcs extend from frame 40 to frame 115. Small white rectangle shows region used for area interpolation. Large rectangle shows maximum extent of grid used for processed data.

frame 35 and slight traces of excessive flow angularity near frame 120, the arcs (except for those truncated as just described) now run from frame 40 to frame 115 inclusive. The first valid frame of each arc has been noted in Table 8 above. A comparison of Figures 34 and 39 shows that the scheme outlined here has sacrificed much of the redundancy of the original data, although two traverses at different angles remain in the important region of the separation bubble.

It is evidently necessary to think of the boundary layer and wake in the present experiments as corresponding to a gradually changing pressure distribution on the airfoil as the traverse and rotor move downstream. The pressure distribution for any traverse position can be obtained by adding the increments

$\Delta C_p$ in Table 10 to the pressure coefficients in the same table. The problem can be ignored (in the sense that the data for different arcs are in satisfactory agreement) when the rotor is at or downstream of X = 80 cm (x = 109 cm in airfoil coordinates). This is the position which marks the beginning of the horizontal traverse. The main part of the separation bubble can be taken as interference-free, but the boundary layer up to separation can not.

This problem was not foreseen. Most of the interference was presumably caused by the cylindrical excrescences which are visible on the rotor hub in Figure 2. On one side was a shaft extension whose purpose was to move the rotor blades away from the strut and to provide for cable bracing (see Section 3.1 of CCW). On the other side was a commercial mercury-slip-ring assembly whose dimensions were thought not to be under our control. If the problem had been foreseen, use of custom components and use of flow control near the rotor hub could probably have reduced the blockage effect to a much lower level.

5.2 Global Correction to the Data

Our original intention was to perfect the hot-wire data by exploiting three elements of redundancy. The first element was the use of two probes and the duplication of certain measurements. This element was exploited fully in Section 4.3 in dealing with drift in the instrumentation. The second element was the fact that measurements were made while passing through some parts

of the flow in the two or three different directions displayed in Figure 34. This element was practically nullified by the rotor interference effects which have just been described in Section 5.1 and which required deletion of an important fraction of the hot-wire data. The third element was the expectation that interference effects should be nearly the same for the surviving hot-wire measurements and for the pitot-static measurements documented above in Section 3.3 and Figure 22. Thus these measurements should agree.

Observed Errors. -- We were aware, during the processing described under "Use of Benchmark Files" in Section 4.3 above, that the velocities being obtained along the benchmark arc were too low by about three to four percent at the intersections of the benchmark arc with the pitot-static traverse lines which lie above and below the airfoil in Figure 22b. The discrepancy was nearly independent of the particular wire pair being used. It was not removed by assigning a later and perhaps more realistic time to the post-test calibration points (the stars in Figure 35; for timing, see Table 1 of CCW). A plausible explanation of the discrepancy is that the benchmark velocity field was characteristic of only a small fraction of the total wire calibration, being nearly equivalent to one of the trajectories in Figure 33. Thus the observed error of about two percent in (U, V) may have been incurred when wire parameters for the total calibration were used for inversion. This hypothesis was not tested directly, because its adoption could only lead to chaos in the values

assumed by the wire parameters. An alternative explanation of the discrepancy might be that the drift curves at late times in Figure 35 were not well enough represented by straight lines over the large time interval involved.

A Correction. -- Lacking a sound explanation of the discrepancy, we chose to prepare for further processing by making a global correction to the raw hot-wire data. Specifically, we increased the relative velocities (U, V) everywhere by exactly two percent. The correction was mechanically simple. It had to be made after applying Equations (18) and (22) but before applying Equations (23). The procedure therefore began with recovery of tangential and radial relative velocities (U, V) in m/sec from the dimensional version of the absolute velocities $(\overline{u}, \overline{v})$ in tunnel coordinates. The latter were already stored on punched cards as official raw data, as described under "Execution" in Section 4.4 above. Equations (23) with $\theta = 0$ were first solved for (U, V); thus

$$\left.\begin{aligned} U &= \overline{u} \cos \phi + \overline{v} \sin \phi + \omega R \\ V &= \overline{u} \sin \phi - \overline{v} \cos \phi \end{aligned}\right\} \qquad (24)$$

The values obtained for (U, V) from these equations were multiplied by 1.02, reconverted to $(\overline{u}, \overline{v})$ using Equations (23) with $\theta = 0$ directly, and again made dimensionless. Dimensionless products of fluctuations from the punched cards were simply multiplied by $(1.02)^s$, where s was the order of the product.

The magnitude of the correction just described was chosen to force agreement between the mean hot-wire data and the pitot-static data at certain points. These are the sixteen free-stream points (marked by parentheses in the last column of Table 3) for which the full total pressure was felt by the pitot-static probe and the error in probe angle was less than four degrees. The agreement in the magnitude of the velocity, after correction of the hot-wire data, is within a fraction of one percent in all cases, on both sides of the airfoil and for values of $q/q_{ref}$ from 1.0 to 1.4. Elsewhere in the flow, the hot-wire data have also changed. In the free stream, the flow angles have changed by as much as one degree at the extremities of the probe arcs. In the separation bubble, the dimensionless mean velocity has changed in magnitude by about 0.02, and in angle by unknown amounts. The Reynolds stresses and higher moments, however, have merely been multiplied everywhere by constant factors close to unity.

5.3 Smoothing and Interpolation

Area Interpolation. -- The data of the present experiment are defined at points which are closely spaced from the point of view of an experimenter, but which might be considered sparse and awkwardly placed from the point of view of a numerical analyst. We have therefore carried out some further processing to serve the needs of users whose interest is primarily in turbulence modeling. One objective was to redefine the data on a rectangular grid which is sufficiently fine to satisfy the analyst

without driving the data beyond their real accuracy. Moreover, because discrepancies will inevitably arise in any comparison of measured and calculated quantities, we considered it important to judge the accuracy of the measurements independently of their use. A second objective was therefore to examine the spatial derivatives which play a role in the mean continuity and momentum equations and in the definition of mean spanwise vorticity.

The need for some better interpolation scheme became apparent when the question of probe interference was first studied in terms of contour plots based on linear interpolation in the uncorrected raw data. Many of the contours showed local waves where probe arcs crossed contours at a shallow angle. Moreover, there was no hope of estimating spatial derivatives with acceptable accuracy where these were large. A better interpolation scheme was required. The one proposed here has served quite well, and may be adaptable to other research whenever there is a need to convert sparse data to a finer and more regular grid system.

Level Curves. -- The starting point for the interpolation was the information on punched cards characterized as "raw data" at the end of Section 4.4. The raw data were first reduced to the partial set depicted in Figure 39 to bypass the interference problem discussed in Section 5.1. The correction described in Section 5.2 was then applied to the raw data. Each variable was next averaged for the two probes for each frame, and the value obtained was assigned to the position calculated using the

mean probe radius. All velocity components were rotated into airfoil coordinates to obtain u, v and products of their fluctuations. Duplicate files, including benchmarks, were represented by a single average file. In principle, these operations and all subsequent ones could be duplicated or modified by any interested party. However, the processing was both tedious and expensive. The final results have therefore also been made available on punched cards, in which form they will be characterized as "processed data".*

The rectangular grid system used for processed data was aligned with the airfoil chord. The mesh size was one centimeter in the chordwise direction and 0.2 centimeters in the crossflow direction. Integer grid indices IX and IY were related to the coordinates x and y of Section 4.1 and Figure 26 by

$$IX = 1 + (x - 6.86)$$
$$IY = 1 + 5(y + 12.41) \qquad (25)$$

where x and y are in centimeters. The range of the grid was IX = 1(1)175 and IY = 1(1)296. The outline of the corresponding rectangle, 174 cm by 59 cm, is shown superposed on the airfoil and on the probe arcs in Figure 39.

---

*As of this writing, these cards have not yet been punched.

Each of the fifteen (dimensionless) experimental variables

| | | | | |
|---|---|---|---|---|
| $\langle u \rangle$ | $\langle u'u' \rangle$ | $\langle u'u'u' \rangle$ | $\langle u'u'u'u' \rangle$ | $\langle \gamma \rangle$ |
| $\langle v \rangle$ | $\langle u'v' \rangle$ | $\langle u'u'v' \rangle$ | $\langle u'u'u'v' \rangle$ | |
| | $\langle v'v' \rangle$ | $\langle u'v'v' \rangle$ | $\langle u'u'v'v' \rangle$ | |
| | | $\langle v'v'v' \rangle$ | $\langle u'v'v'v' \rangle$ | |
| | | | $\langle v'v'v'v' \rangle$ | |

was treated separately. In what follows, the symbol $z(x, y)$ can refer to any one of these variables. A small rectangle having its long dimension oriented parallel to the chord line (i.e., parallel to the general direction of the boundary layer and wake) was centered on each of the thousands of data points in succession. The rectangle finally used was 10 cm by 3 cm, the 3-cm dimension being chosen so that at least three data arcs would be involved in the downstream part of the wake region, where the traverse displacement between arcs was 0.5 inches. This rectangle is shown to scale as the white area near the trailing edge of the airfoil in Figure 39. Other data points were then sought within the rectangle such that the value of the dependent variable z differed from the value at the center point by no more than a specified increment.* For chordwise mean velocity, for example, the two values of $z = \langle u \rangle / q_{ref}$ could not differ by more than 0.1. A straight line was drawn connecting each such pair of points,

---

* This increment in all cases was the same as the contour interval used in Figures 42-46 below.

and linear interpolation was used to derive a value for z at any grid lines which lay between. In effect, short line segments were thus found, of length 5 cm or less, which lay close to a level curve of the surface z(x, y). To simplify bookkeeping, the set of several thousand data points was first sorted in order of increasing x, and the interpolation process was carried out from left to right. Consequently, data to the left of the center point were always among previously processed data.

Guard Lines. -- One complication appeared in the neighborhood of maxima or minima in z, since the end points used for interpolation might lie on different slopes of a ridge, valley, or saddle of the surface z(x, y). Use of the normal increment might then result in a kind of cut-and-fill operation near extrema in z. The remedy was to examine primitive contour plots obtained from raw data, and to construct guard lines in appropriate places. If the two data points destined for interpolation lay on opposite sides of a guard line, they were used only if they both fell within a specified small distance from the guard line (typically 0.2 cm).

Thinning and Fitting. -- This interpolation process was not very sensitive to details, and details are therefore not spelled out numerically. We were quite satisfied with the results, which were obtained in the form of a large and acceptably smooth array of data along each grid line at constant x. This array was finally thinned, so that no more than two interpolated data points appeared in any one-millimeter interval in y. The two surviving

points were the ones for which the original end values of z were closest to each other. At the end of this process, the number of data points along any grid line was increased by an order of magnitude over the number obtainable by the original process of linear interpolation along data arcs.

Finally, a fitting and smoothing operation was carried out over an interval of 2 cm in y centered on each grid point. Near the edges of the experimentally defined part of the flow, the interval was symmetrically enlarged as necessary until at least 12 data points were included. The fitted curve was a cubic. Only the value of z and its first derivative at the grid point were saved.

These procedures are illustrated by Figures 40 and 41. The variable is $< u'u' >$. Figure 40 shows contour lines obtained by linear interpolation along probe arcs in the (corrected, averaged, rotated) raw data to obtain profiles at constant x, followed by linear interpolation in y. The improvement obtainable by area interpolation and smoothing is evident when these contours

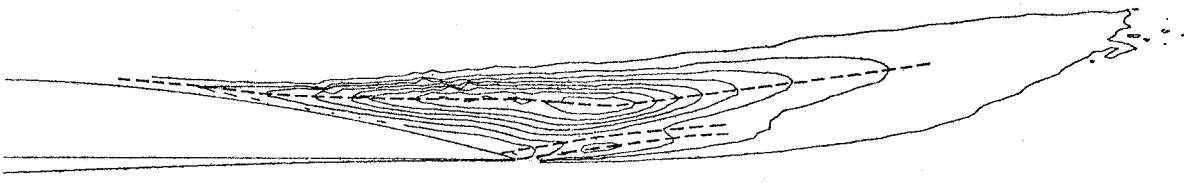

Figure 40. Contour lines for $< u'u' >$ as obtained by linear interpolation in raw data. Heavy dashed lines are guard lines used during area interpolation.

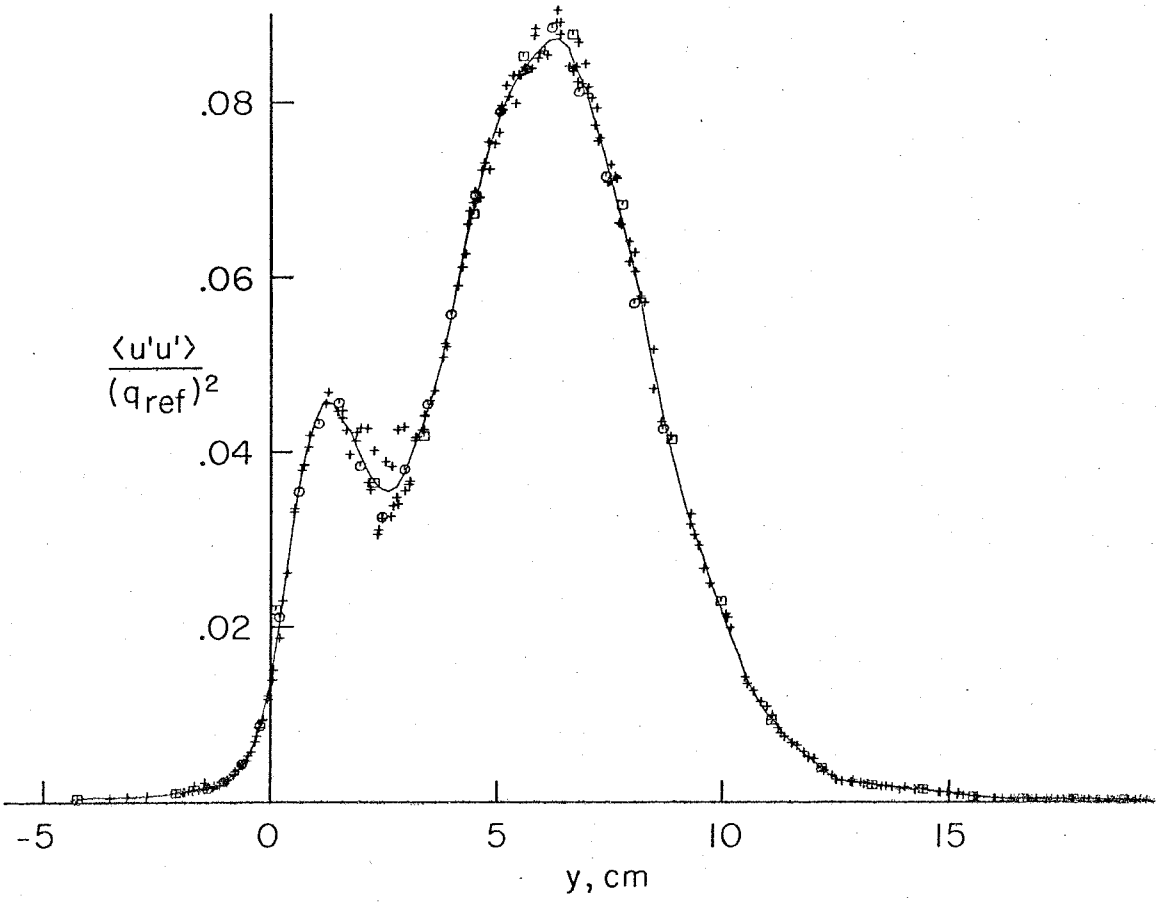


Figure 41. Comparison of data for $\langle u'u' \rangle/(q_{ref})^2$ at x = 98.86 cm (IX = 93) as obtained by different methods of interpolation. Open symbols: same as in Figure 38. Crosses: result of area interpolation, after thinning to obtain a maximum of two points per millimeter in y. Solid line: fitted curve.

are compared to the final ones in Figure 44 below, and is much more striking for higher moments. Figure 40 also shows the location of the three guard lines which were found to be necessary for this particular variable.

Figure 41 is a plot of the same variable $\langle u'u' \rangle$ as a function of y at x = 98.86 cm (IX = 93), near the center of the separation bubble. The open symbols are identical to the ones

shown previously in Figure 38. The crosses are the data obtained by area interpolation and thinning. The solid line is the fitted curve.

Discussion.--Figures 42, 43, 44, 45, and 46 are contour plots of the fifteen experimental variables listed under "Level Curves" above. The plots display the richness of the present data, but they say little about accuracy. We believe that the absolute accuracy of the data is within 0.02 in the case of the dimensionless mean-velocity components, and within 5 percent in the case of the Reynolds stresses, with progressively decreasing accuracy in the higher moments. The flow angles are relatively uncertain, partly because such uncertainty is inherent in hot-wire anemometry and partly because of the almost arbitrary correction made to the data in Section 5.2. The quality of the description obtained for the mean flow could be tested by constructing a stream function, but this has not yet been done. In fact, the flying-hot-wire data have not been connected to the airfoil surface at all. Neither has the ultimate calculation, the calculation of static pressure by integration of the full Reynolds equations, so far been attempted.

The present research was commissioned primarily to provide data for use in modeling of turbulent flow. The issues in turbulence modeling are as varied as the modelers. The main problem in modeling is closure, which means simply making the number of equations equal to the number of dependent variables. While a knowledge of high-order correlations may

not always be necessary for this purpose, such knowledge can also serve a different purpose in studies of probability distributions for turbulent fluctuations (cf. the putative relationship between flatness factor and intermittency).

The present data may also allow a fresh examination of at least two other important concepts in turbulence. One is the observed near-constancy of the correlation $\langle u'v' \rangle / \langle u'u' \rangle^{\frac{1}{2}} \langle v'v' \rangle^{\frac{1}{2}}$ for a wide variety of flows; the other is the validity of a scalar eddy viscosity, as epitomized by a nearly constant value for the ratio $\langle u'v' \rangle / \partial \langle u \rangle / \partial y$.

More modest purposes may also be served. For example, one of the most useful and well-established concepts in aerodynamics is the theory of thin airfoils. Stall is essentially a departure from this theory caused by viscous effects. It may be that some simple modification of thin airfoil theory, including particularly the Kutta-Joukowski condition, can be found to account for first-order effects of separation and bubble closure on effective chord, camber, and angle of attack. In any event, the present data are submitted as a comprehensive and permanent addition to the experimental literature of separating turbulent flow.

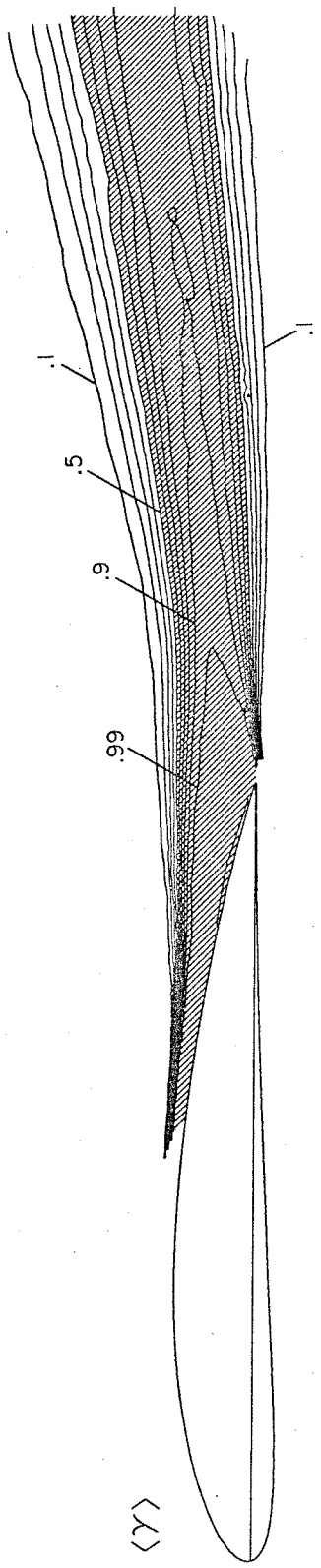


Figure 42. Contour plot for intermittency factor $\langle\gamma\rangle$ from final processed data. Contour interval 0.1.

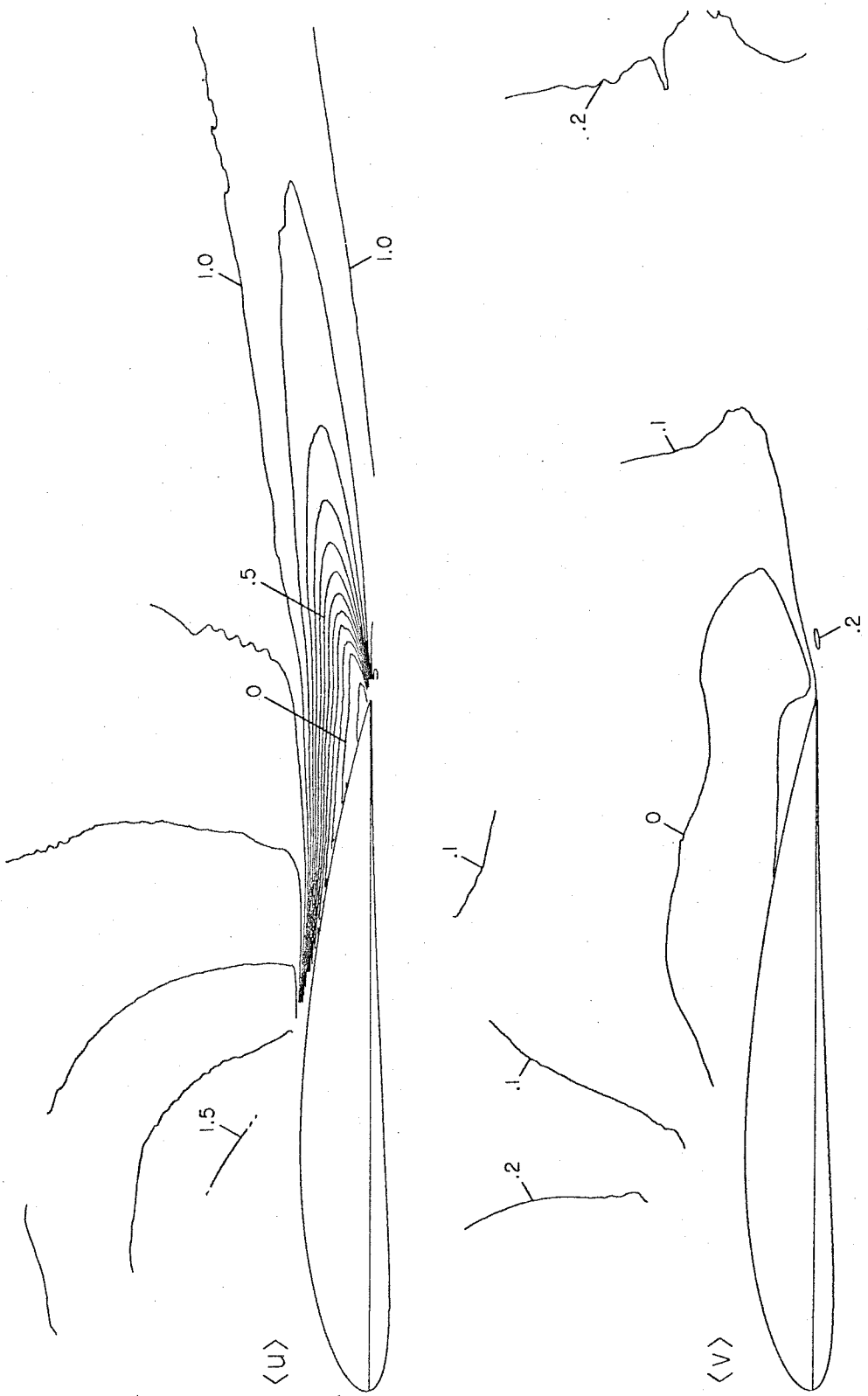


Figure 43. Contour plots for dimensionless mean-velocity components from final processed data. Contour intervals: $\langle u \rangle / (q_{ref})$; 0.1
$\langle v \rangle / (q_{ref})$; 0.1

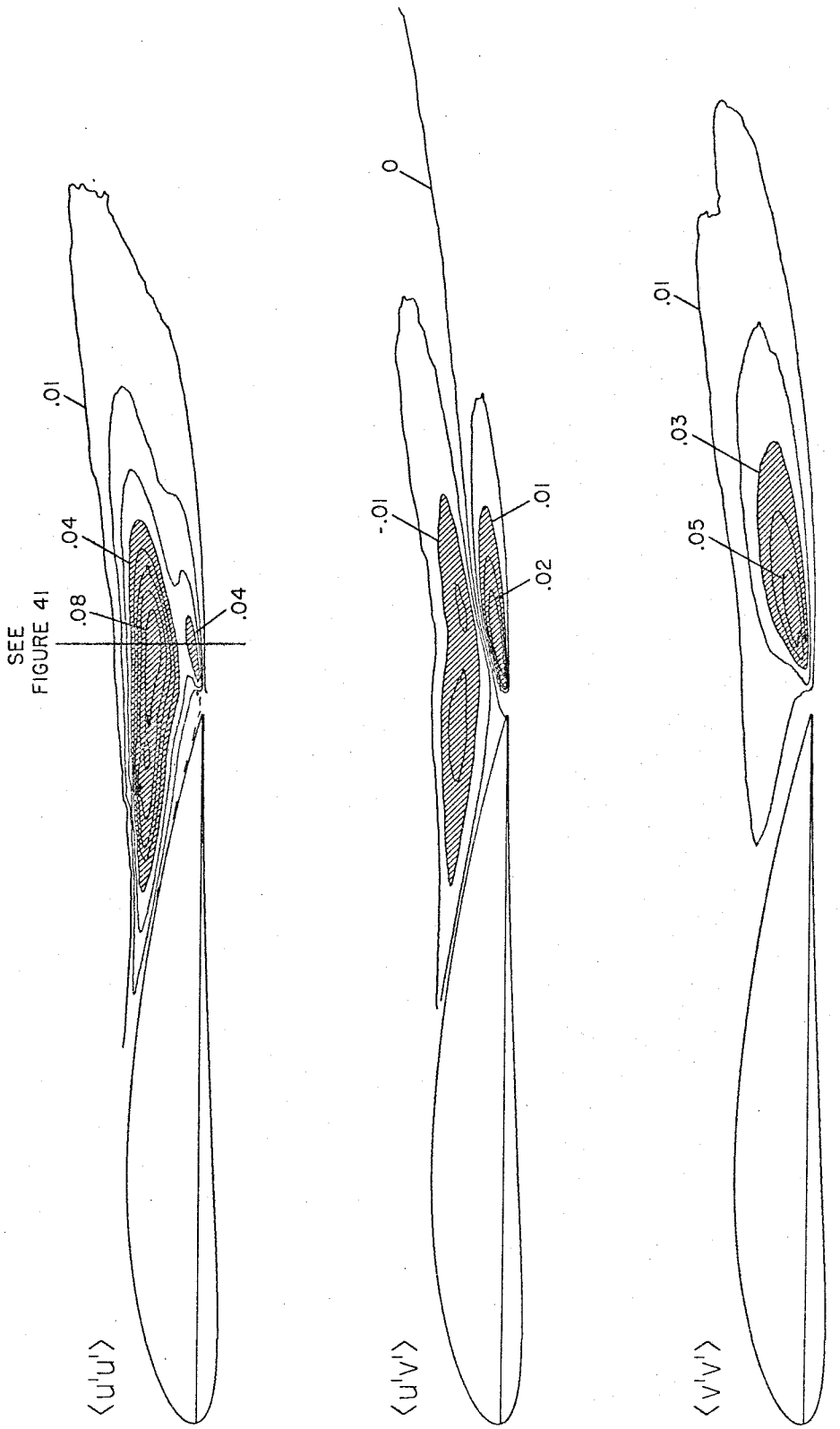


Figure 44. Contour plots for dimensionless double correlations from final processed data. Contour intervals: $\langle u'u' \rangle / (q_{ref})^2$; 0.010
$\langle u'v' \rangle / (q_{ref})^2$; 0.005
$\langle v'v' \rangle / (q_{ref})^2$; 0.010

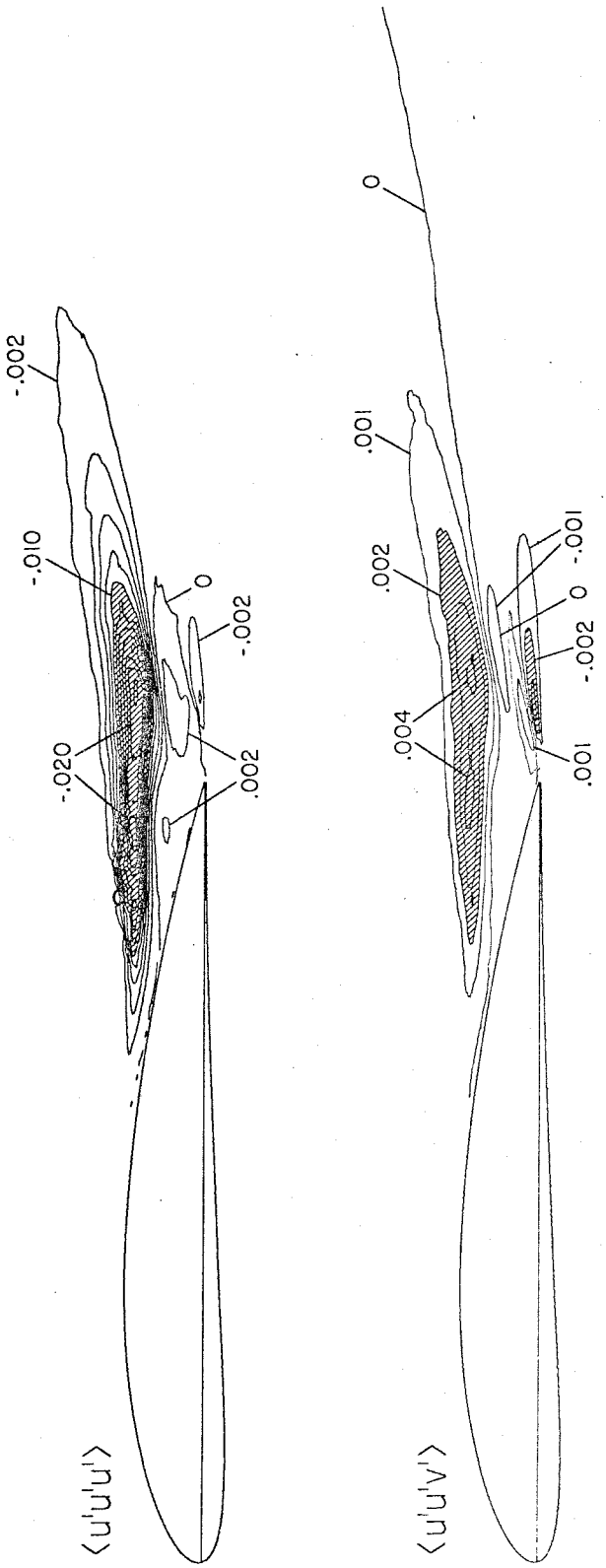


Figure 45.

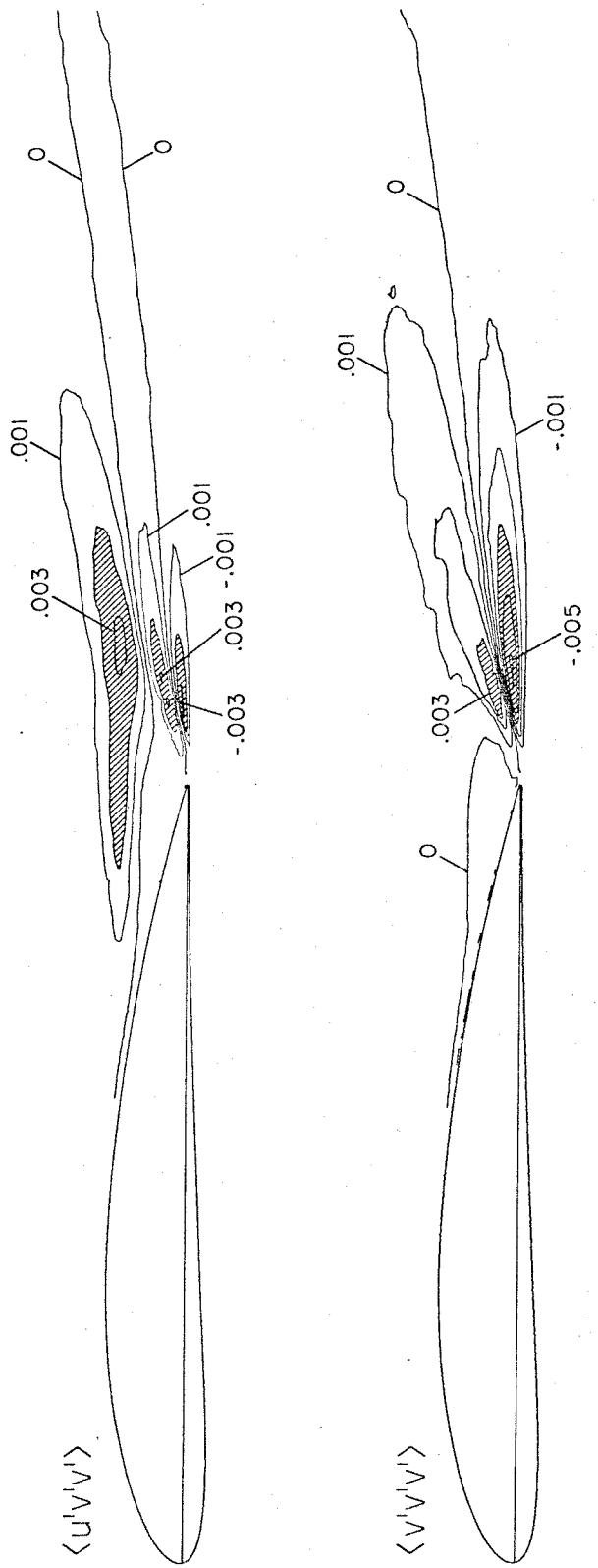


Figure 45. Contour plots for dimensionless triple correlations from final processed data. Contour intervals: $\langle u'u'u' \rangle / (q_{ref})^3$; 0.002
$\langle u'u'v' \rangle / (q_{ref})^3$; 0.001
$\langle u'v'v' \rangle / (q_{ref})^3$; 0.001
$\langle v'v'v' \rangle / (q_{ref})^3$; 0.001

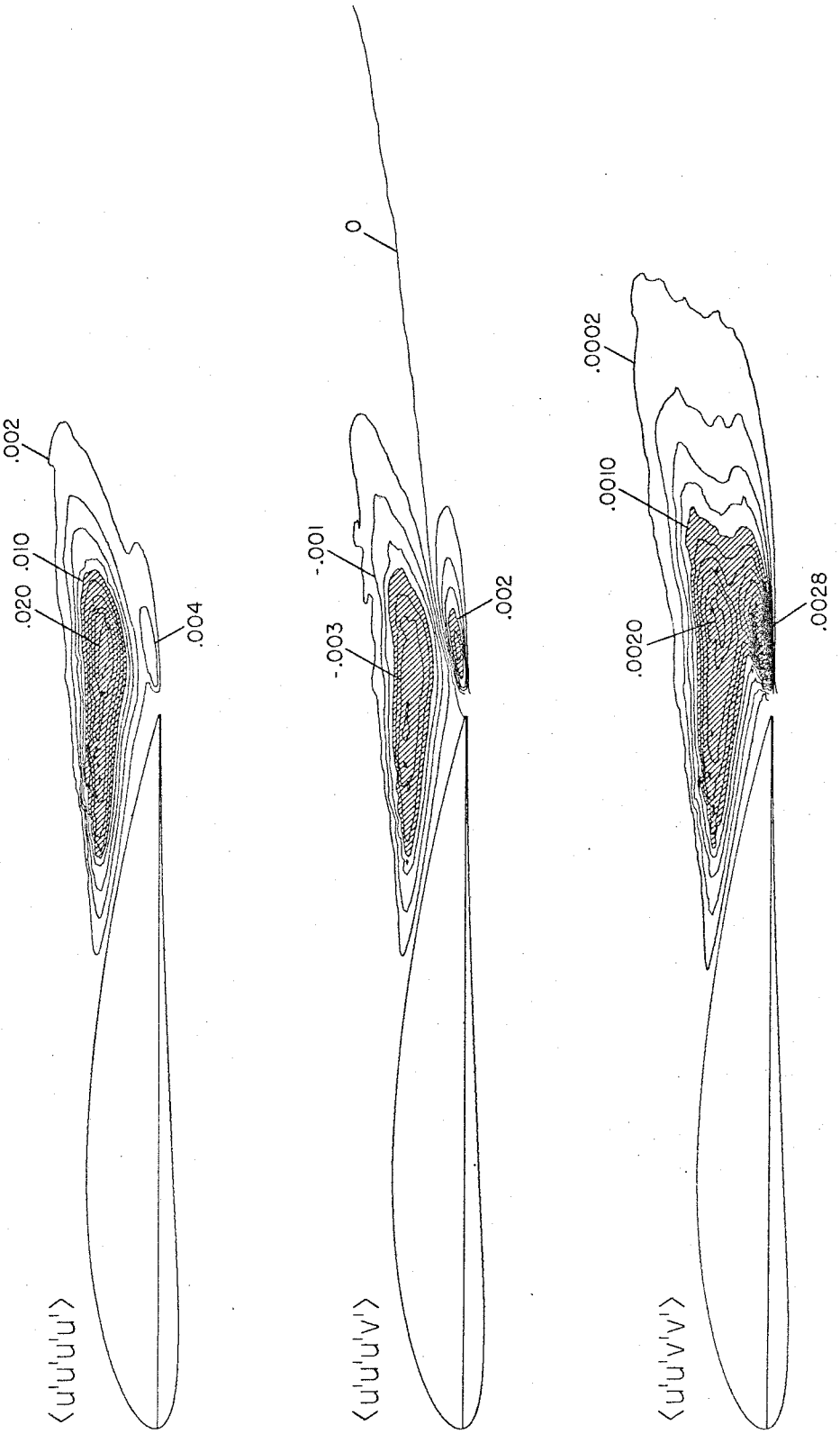
.002
.010
.020
.004
<u'u'u'u'>
0
-.001
-.003
.002
<u'u'u'v'>
.0002
.0010
.0020
.0028
<u'u'v'v'>

Figure 46.

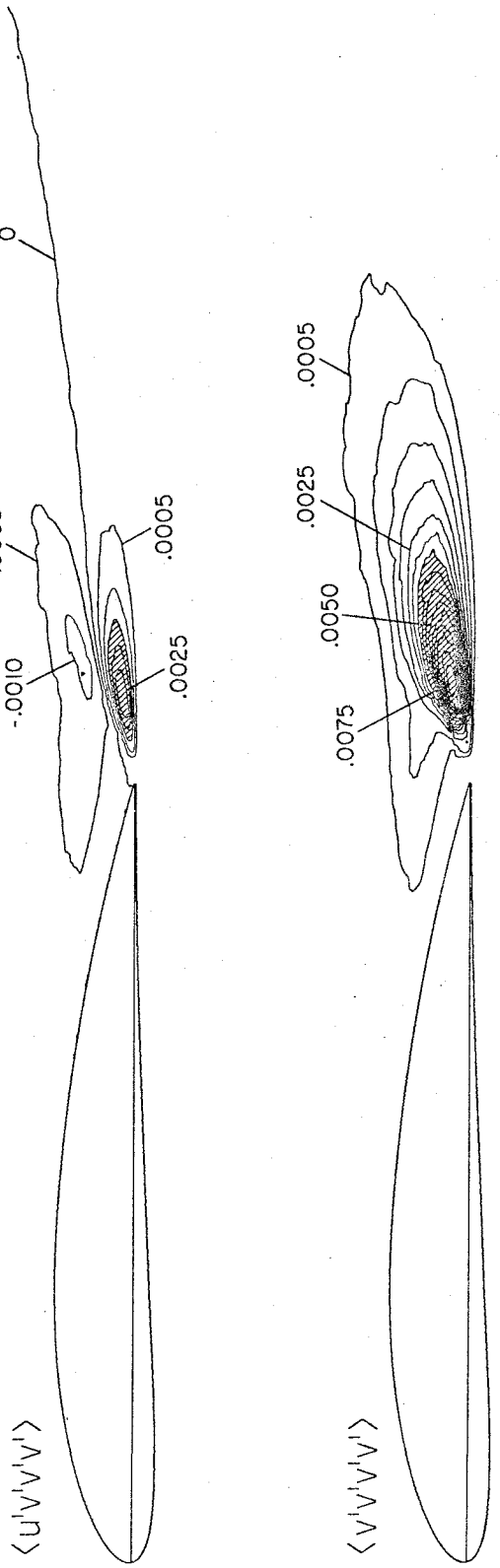


Figure 46. Contour plots for dimensionless quadruple correlations from final processed data. Contour intervals: $\langle u'u'u'u' \rangle / (q_{ref})^4$; 0.0020
$\langle u'u'u'v' \rangle / (q_{ref})^4$; 0.0005
$\langle u'u'v'v' \rangle / (q_{ref})^4$; 0.0002
$\langle u'v'v'v' \rangle / (q_{ref})^4$; 0.0005
$\langle v'v'v'v' \rangle / (q_{ref})^4$; 0.0005

# REFERENCES

Abbott, I. H. and von Doenhoff, A. E. 1949 Theory of wing sections. McGraw-Hill (reprinted, Dover, 1959).

Bradbury, L. J. S. 1976 Measurements with a pulsed-wire and a hot-wire anemometer in the highly turbulent wake of a normal flat plate. J. Fluid Mech. 77, 473-497.

Cantwell, B. J. 1975 A flying hot wire study of the turbulent near wake of a circular cylinder at a Reynolds number of 140,000. Ph. D. Thesis, Calif. Inst. Technology.

Caupenne, P. 1976 Études expérimentales et théoriques sur les décollements de profiles. Paper at 13th Coll. on Applied Aerodynamics, École Central Lyonnaise, 8-10 Nov.

Chu, J. and Young, A. D. 1975 Measurements in separating two-dimensional turbulent boundary layers. AGARD CP 168, "Flow Separation", Paper 13.

Coles, D. E. and Hirst, E. A. (eds.) 1968 Proc. AROSR-IFP-Stanford Conf., "Computation of Turbulent Boundary Layers"; Vol. II, Compiled Data. Dept Mech. Engrg., Stanford Univ.

Coles, D., Cantwell, B. and Wadcock, A. 1977 The flying hot wire and related instrumentation. Techn. Rep. to NASA Ames Research Center (NASA Grant NGL 05-002-229).

Fomina, N. N. and Buchinskaia, E. K. 1938 Experimental investigation of the two-dimensional boundary layer. Trudy TsAGI, Moscow, No. 374 ( in Russian; available from Library of Congress).

Goradia, S. H., Mehta, J.M., and Shrewsbury, G. D. 1977 Analyses of the separated boundary layer flow on the surface and in the wake of blunt trailing edge airfoils. Contract Rep., Lockheed-Georgia Co. (NASA CR 145202).

Gregory, N., Quincey, V. G., O'Reilly, C. L., and Hall, D. J. 1971 Progress report on observations of three-dimensional flow patterns obtained during stall development on aerofoils, and on the problem of measuring two-dimensional characteristics. ARC, CP 1146.

Jacobs, E. N., Ward, K. E., and Pinkerton, R. M. 1933 The characteristics of 78 related airfoil sections from tests in the variable-density wind tunnel. NACA TR 460.

Owen, F. K. 1976 Measurements and observations of turbulent recirculating jet flows. AIAA J. 14, 1556-1562.

Perry, A. E. and Morrison, G. L. 1971 A study of the constant-temperature hot-wire anemometer. J. Fluid Mech. 47, 577-599.

Pinkerton, R. M. 1936 Calculated and measured pressure distributions over the midspan section of the NACA 4412 airfoil. NACA Rep. 563.

Pinkerton, R. M. 1938 The variation with Reynolds number of pressure distribution over an airfoil section. NACA Rep. 613.

Schubauer, G. B. and Klebanoff, P. S. 1950 Investigation of separation of the turbulent boundary layer. NACA TN 2133.

Seetharam, H. C. and Wentz, W. H. Jr. 1977 Experimental investigation of subsonic turbulent separated boundary layers on an airfoil. J. Aircraft 14, 51-55.

Simpson, R. L., Strickland, J. H., and Barr, P. W. 1977 Features of a separating turbulent boundary layer in the vicinity of separation. J. Fluid Mech. 79, 553-594.

Spalding, D. B. 1961 A single formula for the "law of the wall". Trans. ASME 28E (J. Appl. Mech.), 455-457.

Tombach, I. 1973 An evaluation of the heat pulse anemometer for velocity measurement in inhomogeneous turbulent flow. Rev. Sci. Instr. 44, 141-148.

Tutu, N. K. and Chevray, R. 1975 Cross-wire anemometry in high intensity turbulence. J. Fluid Mech. 71, 785-800.

de Vos, D. M. 1973 Low speed windtunnel measurements on a two-dimensional flapped wing model using tunnel wall boundary layer control at the wing-wall junctions. NLR TR 70050 U.

Wentz, W. H. Jr. and Seetharam, H. C. 1977 Split-film anemometer measurements on an airfoil with turbulent separated flow. Paper at 5th Biennial Symp. on Turbulence, Rolla.

Willmarth, W. W. and Bogar, T. J. 1977 Survey and new measurements of turbulent structure near the wall. Phys. Fluids 20, Supplement, S9-S21.